

NASA-CR-190908

PROGRESS REPORT

Title: REMOTE SENSING OF EARTH TERRAIN

Sponsored by: National Aeronautics and Space Administration

Contract number: NAGW-1617

Research Organization: Center for Electromagnetic Theory and Applications
Research Laboratory of Electronics
Massachusetts Institute of Technology

OSP number: 71715

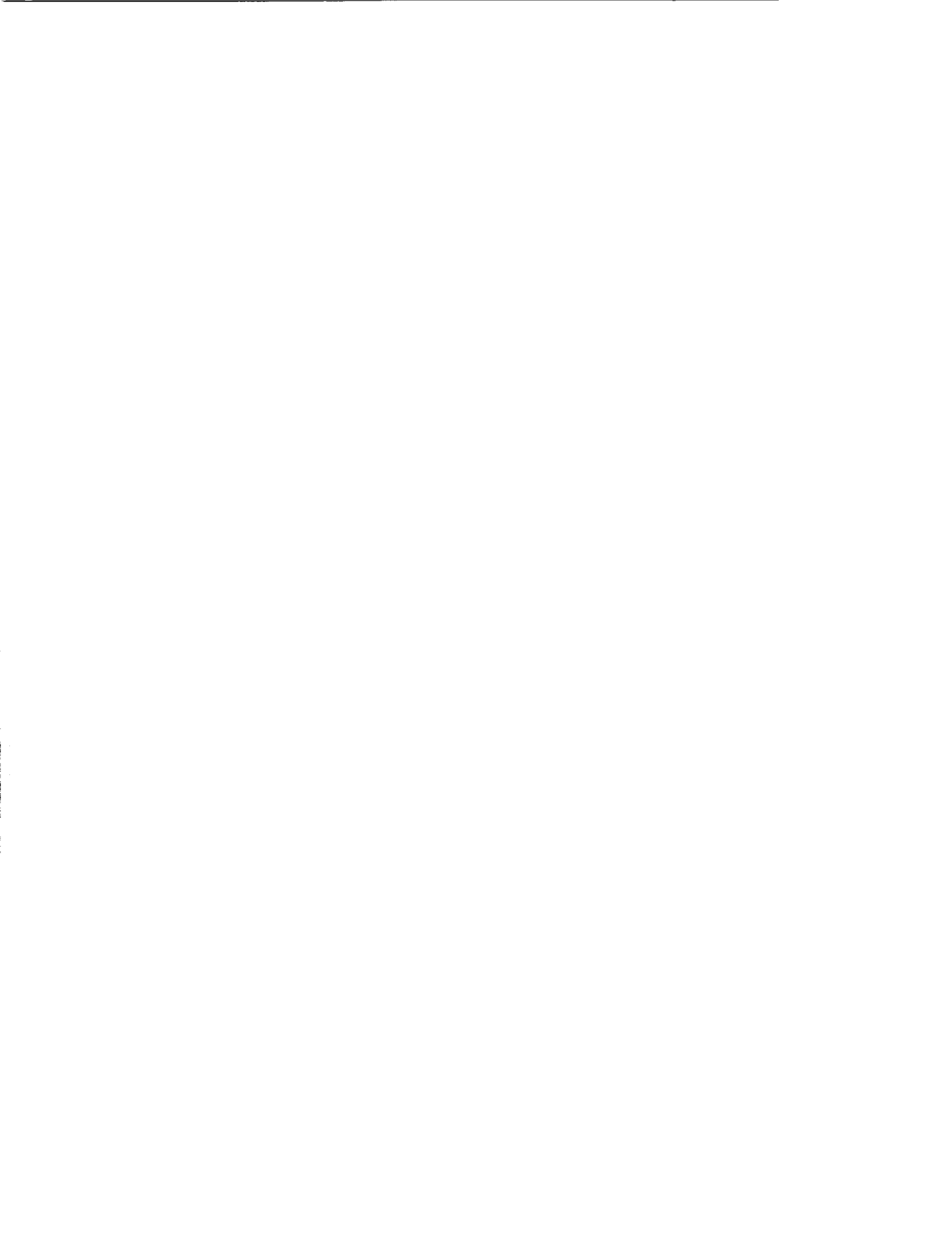
Principal Investigator: J. A. Kong

Period covered: January 1, 1992 — September 30, 1992

(NASA-CR-190908) REMOTE SENSING OF
EARTH TERRAIN Progress Report, 1
Jan. - 30 Sep. 1992 (MIT) 77 p

N93-13084
--THRU--
N93-13088
Unclas

G3/43 0121973



REMOTE SENSING OF EARTH TERRAIN

Under the sponsorship of the NASA Contract NAGW-1617, we published 56 refereed journal and conference papers for the research on remote sensing of earth terrain. The following is a summary of recent research findings.

Application of Theoretical Models to Active and Passive Remote Sensing of Saline Ice

The random medium is used to interpret the polarimetric active and passive measurements of saline ice. The ice layer is described as a host ice medium embedded with randomly distributed inhomogeneities, and the underlying sea water is considered as a homogeneous half-space. The scatterers in the ice layer are modeled with an ellipsoidal correlation function. The orientation of the scatterers is vertically aligned and azimuthally random. The strong permittivity fluctuation theory is employed to calculate the effective permittivity and distorted Born approximation is used to obtain the polarimetric scattering coefficients. We also calculate the thermal emissions base on the reciprocity and energy conservation principles. The effects of the random roughness at the air-ice, and ice-water interfaces are accounted for by adding the surface scattering to the volume scattering return incoherently. The above theoretical model, which has been successfully applied to analyze the radar backscatter data of the first-year sea ice near Point Barrow, AK, is used to interpret the measurements performed in the CRRELEX program.

Radiative Transfer Theory for Polarimetric Remote Sensing of Pine Forest

The radiative transfer theory is applied to interpret polarimetric radar backscatter from pine forest with clustered vegetation structures. To take into account the clustered structures with the radiative transfer theory, the scattering function of each cluster is calculated by incorporating the phase interference of scattered fields from each component. subsequently, the resulting phase matrix is used in the radiative transfer equations to evaluate the polarimetric backscattering coefficients from random medium layers embedded with vegetation clusters. Upon including the multi-scale structures, namely, trunks, primary and secondary branches, as well as needles, we interpret and simulate the polarimetric radar responses from pine forest for different frequencies and looking angles. The preliminary results are shown to be in good agreement with the measured backscattering coefficients at the Landes maritime pine forest the MAESTRO-1 experiment.



Scattering of Electromagnetic Waves from a Dense Medium Consisting of Correlated Mie Scatterers with Size Distributions and Applications to Dry Snow

The scattering of a plane electromagnetic wave obliquely incident on a layer of dense medium consisting of dielectric spherical particles of finite sizes and with size distributions is studied. The spherical particles are of sizes comparable to wavelength so that Mie scattering is used to describe the single particle scattering characteristics. The coherent wave is studied with quasicrystalline approximation using the cross pair distribution functions of multiple size governed by Percus-Yevick approximation. The incoherent scattered wave is calculated with the distorted Born approximation with the result expressed in terms of a product of the T-matrices of particles of different sizes and permittivities and the Fourier transform of the cross pair distribution functions. The coherent wave effective propagation constants, the attenuation rates and the backscattering coefficients are illustrated numerically, with examples chosen to illustrate microwave and millimeter wave scattering from snow cover in the frequency range of 5 GHz to 95 GHz, and mean grain radius between 0.03 cm to 0.09 cm. Salient features of the numerical results for scattering from snow with size distribution are: (1.) Correlated dense medium scattering is less than independent scattering at low frequency, a fact that is consistent with controlled laboratory experiment. (2.) Scattering from dense medium of a Rayleigh size distribution with an average radius can be much larger than the case of monodisperse particles of the sizes identical to that average radius. (3.) The scattering attenuation rate increases rapidly with frequency at low frequency regime and begins to level off at high frequency regime. (4.) The coherent wave scattering attenuation rate is large in snow at frequencies above 15 GHz indicating large optical thickness and the important of multiple scattering. Comparisons with extinction measurements of dry snow at 18 GHz, 35 GHz, 60 GHz, and 90 GHz are made.

Variance of Phase Fluctuations of Waves Propagating through a Random Medium

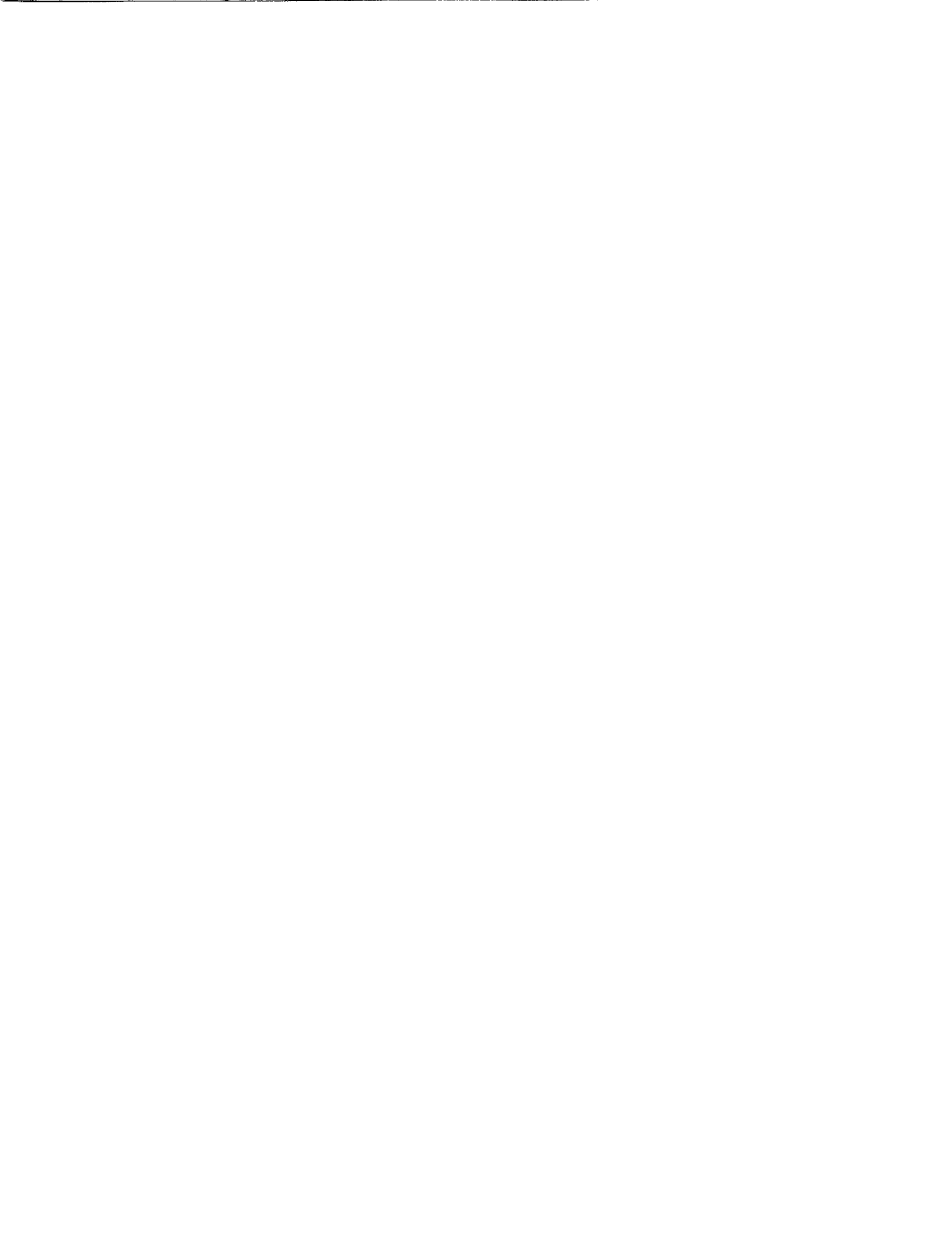
As an electromagnetic wave propagates through a random scattering medium, such as a forest, its energy is attenuated and random phase fluctuations are induced. The magnitude of the random phase fluctuations induced is important in estimating how well a Synthetic Aperture Radar (SAR) can image objects within the scattering medium. The two-layer random medium model, consisting of a scattering layer between free space and ground, is used to calculate the variance of the phase fluctuations induced between a transmitter located above the random medium and a receiver located below the random medium. The scattering properties of the random medium are characterized by a correlation function of the random permittivity fluctuations. The effective permittivity of the random medium is first calculated using the strong fluctuation theory, which accounts for large permittivity fluctuations of the scatterers. The distorted Born approximation is



used to calculate the first-order scattered field. A perturbation series for the phase of the received field in the Rytov approximation is then introduced and the variance of the phase fluctuations is solved to first order in the permittivity fluctuations. The variance of the phase fluctuations is also calculated assuming that the transmitter and receiver are in the paraxial limit of the random medium, which allows an analytic solution to be obtained. Results are compared using the paraxial approximation, scalar Green's function formulation, and dyadic Green's function formulation. The effects studied are the dependence of the variance of the phase fluctuations on receiver location in lossy and lossless regions, medium thickness, correlation length and fractional volume of scatterers, depolarization of the incident wave, ground layer permittivity, angle of incidence, and polarization.

Theoretical Modeling for Passive Microwave Remote Sensing of Earth Terrain

Historically, the volume scattering effects stimulated the development of the continuous random medium model and the random discrete scattering model for the description of the media. Theoretical treatments were developed along two different paths. Invoking the principle of reciprocity, the wave theory based on Maxwell's equations has been used to calculate the emissivity. The other approach was to start with the radiative transfer equations and solved for the brightness temperatures directly. Attempts have been made to derive the radiative transfer theory from the wave theory. At the same time, both theoretical approaches have been used to calculate the radiometric emissions and to interpret experimentally measured data. The successful interpretation of the Cosmos 243 data was perhaps the first most important step towards a serious development of the continuous random medium model to account for the volume scattering effects of snow ice fields. Subsequent interpretation of measurement results from snow field with both passive radiometers and active radar systems established a unique position for its description of earth terrain media. Recent efforts in classifying sea ice with correlation function characterization are demonstration of acceptance of this model. Future inverse scattering developments will perhaps rely heavily on this model. In this paper, we shall illustrate the development of the theoretical models and present data matching results with measurements made in snow ice fields and vegetation canopies. The emissivity calculations for periodical rough surfaces will also be presented and compared to measured data. Recent development in polarimetric active remote sensing with synthetic aperture radar has created significant theoretical results and practical applications. In passive remote sensing, the third and the fourth Stokes parameters for earth remote sensing have not received much attention in the past partly due to the expected small values any measurement can yield. We have made initial calculations and experimental measurements to show that at least the third Stokes parameter can give appreciable number in both theoretical prediction and actual experimentation in a plowed field. Such results may have practical implications in measuring wind directions in ocean waves, for instance. We believe polarimetric passive remote sensing is a viable field which should be explored



in light of its potential applications that may be derived from the full Stokes vector instead of its first two parameters, i.e., the horizontally and vertically polarized brightness temperature components.

Polarimetric Signatures of a Canopy of Dielectric Cylinders Based on First and Second Order Vector Radiative Transfer Theory

Complete polarimetric signatures of a canopy of dielectric cylinders overlying a homogeneous half space are studied with the first and second order solutions of the vector radiative transfer theory. The vector radiative transfer equations contain a general nondiagonal extinction matrix and a phase matrix. The energy conservation issue is addressed by calculating the elements of the extinction matrix and the elements of the phase matrix in a manner that is consistent with energy conservation. Two methods are used. In the first method, the surface fields and the internal fields of the dielectric cylinder are calculated by using the fields of an infinite cylinder. The phase matrix is calculated and the extinction matrix is calculated by summing the absorption and scattering to ensure energy conservation. In the second method, the method of moments is used to calculate the elements of the extinction and phase matrices. The Mueller matrix based on the first order and second order multiple scattering solutions of the vector radiative transfer equation are calculated. Results from the two methods are compared. The vector radiative transfer equations, combined with the solution based on method of moments, obey both energy conservation and reciprocity. The polarimetric signatures, copolarized and depolarized return, degree of polarization, and phase differences are studied as a function of the orientation, sizes, and dielectric properties of the cylinders. It is shown that second order scattering is generally important for vegetation canopy at C band and can be important at L band for some cases.

Branching model for vegetation

A branching model has been proposed for the remote sensing of vegetation. The frequency and angular response of a two-scale cylinder cluster are calculated to demonstrate the significance of vegetation architecture. The results indicate that it is necessary for theoretical remote sensing models to take into account the architecture of vegetation which plays an important role in determining the observed coherent effects. A two-scale branching model is implemented for soybean with its internal structure and the resulting clustering effects considered. Furthermore, at the scale of soybean fields, the relative locations of soybean plants is described by a pair distribution function. The polarimetric backscattering coefficients are obtained in terms of the scattering properties of soybean plants and their pair distribution. Theoretical backscattering coefficients are evaluated using two pair-distribution functions: independent scatterer and hole correction. Backscattering



coefficients calculated by using independent-scatterer pair distribution are in good agreement with extensive data collected from soybean fields except for the data near normal incidence. It is found that the hole-correction approximation, which prevents two soybean plants from overlaying each other, is more realistic. By introducing destructive interference at small angles of incidence, it greatly improves the agreement between the model and these three data sets near normal incidence. Extension to a multi-scale branching model can be achieved by recursion of the two-scale modelling approach reported in this research.

In the past, when radiative transfer theory was applied to the modeling of vegetation, the average phase matrix of vegetation layer was approximated by an incoherent sum of the phase matrices of individual vegetation elements. However, it can be observed that most of vegetation species exhibits a branching structure, whose significance has been demonstrated by the frequency and angular response of a two-scale cylinder cluster. This indicates that it is necessary for theoretical remote sensing models to account for the architecture of vegetation.

In this research, radiative transfer theory is applied to vegetation with clustered structures. To take into account vegetation structure in the radiative transfer theory, the phase matrix of a vegetation cluster is calculated by incorporating the phase interference of scattered fields from every components. Subsequently, the resulting phase matrix is used in the radiative transfer equations to evaluate the polarimetric backscattering coefficients from a layer of medium embedded with vegetation clusters. Theoretical results are illustrated for various kinds of vegetation clusters. It is found that the simulated polarization, frequency, and angular responses carry significant information regarding the structure of vegetation clusters, and also agree with the signatures observed in measured multi-frequency polarimetric synthetic aperture radar images.

In passive remote sensing of earth terrain, the radiative transfer (RT) theory has also been widely applied with various types of random medium models to interpret observation. Part of the advantages of the RT theory can be attributed to its simplicity in formulating the reflection and transmission in the presence of boundaries as well as in treating the scattering effect by the incoherent sum of the scattering from each individual scatterer. However, being restricted by this incoherent nature, the RT theory cannot properly take into account the coherent effect which becomes significant at lower frequency in the case of remote sensing of a structured vegetation canopy as observed in our active models.

In this research, we formulate the vector radiative transfer equation for passive microwave remote sensing of a vegetation canopy overlying a soil half-space, and study the calculated brightness temperatures resulting from microwave thermal emission based on the Gaussian quadrature



numerical method. A randomly distributed stem-leave model is employed to construct the phase matrix such that the effects of coherence and multi-scale can be properly accounted for.

For polarimetric remote sensing, geophysical media are modeled as layers containing randomly embedded scatterers. In a medium such as vegetation canopy, the scatterers can have various shapes, sizes, and permittivities that are significantly distinct from the background medium. The model studied in this research will consider each type of the scatterers as a species which can take on a shape, size, and complex permittivity different from other species. The effective permittivity of the random medium is derived under the strong permittivity fluctuation theory and the polarimetric scattering coefficients are calculated for the layer configuration with the distorted Born approximation in the analytical wave theory which preserves the phase information.

The multiple species in the random medium are considered as randomly oriented ellipsoids and described by multiple three-dimensional ellipsoidal correlation functions. The variances and correlation lengths of the correlation functions characterize the fluctuation strengths and the physical geometry of the scatterers, respectively. The strong permittivity fluctuation theory is extended to account for the multiple species of ellipsoidal shape. In the random medium, a coincidence of an observation point with a source point gives rise to the singularity of the dyadic Green's function which is properly taken into account with exclusion volumes of the scatterers.

Polarimetric scattering properties of a remotely sensed medium are depicted with a covariance matrix whose elements are polarimetric scattering coefficients. The medium has a layer configuration: the top layer such as air is considered as homogeneous, the middle layer such as a vegetation canopy is random, and the underlying layer such as soil is a homogeneous half space. More random medium layers can also be introduced in the configuration to account for weather effect such as fog cover. The distorted Born approximation is then used with the effective permittivity to obtain the polarimetric covariance matrix. The result for the cross-polarized return σ_{hv} is non-zero even in the first order approximation. Due to the non-spherical shape and the random orientation of the scatterers, the correlation coefficient between the HH and VV returns has a magnitude differed from unity and a small phase. The scattering coefficients are also used to calculate the Mueller matrix for synthesis of polarization signatures. The copolarized signature of the random medium has a rather straight distortion track and a recognizable pedestal.

Polarimetric Passive Remote Sensing of Periodic Surfaces

To demonstrate the use of microwave polarimetry for passive remote sensing of azimuthally asymmetric surface features on the earth terrain, we have performed a series of theoretical analysis and experimental measurements for the polarimetric thermal emissions from periodic surfaces. In



our recent research, the third Stokes parameter U for thermal emission from periodic surfaces has been shown to be zero when the observation direction is parallel or perpendicular to the direction of the corrugation, while becomes significant for observation directions between these two directions. Thus, the parameter U is related to the relative azimuthal angles of observation and symmetry axes of periodic surfaces. This implies that measurement of fully polarimetric emissions of all four Stokes parameters can be used to probe the symmetry axes of surface structures. In addition, the other measured Stokes parameters are also shown to be related to the height variations of periodic surfaces, and permittivities of the underlying medium.

To verify the theoretical findings, an experiment was designed and carried out by measuring the polarimetric thermal emissions from a triangularly corrugated soil surface. A triangular corrugation pattern was prepared on a surface of soil with known texture and moisture content. A 10 GHz radiometer operated at linear polarizations was then used to measure the brightness temperatures at different polar and azimuthal angles. The brightness temperatures corresponding to the first three Stokes parameters were measured. The fourth Stokes parameter V was not measured because the radiometer used could not measure the emission at circular polarizations. The measurements were made at horizontal, vertical, and 45° linear polarizations. Significant values of the brightness temperature corresponding to the third Stokes parameter U were observed in various configurations (as high as 40 K for certain configurations). Theoretical analysis of the measurement data indicates that the appreciable values of U are caused by the azimuthal asymmetry of soil surfaces.

It is also observed from the experiment that T_{Bh} decreases, T_{Bv} increases, T_{Bp} decreases to a minimum at $\phi = 45^\circ$ and then increases as ϕ takes on the increased values. For U_B , the trend is similar to that of T_{Bp} . These general trends are supported by our theoretical predictions of the polarimetric brightness temperatures. The significant observation from this experiment is that the surface asymmetry can be detected with a measurement of U_B at a single azimuthal angle.

Composite Volume and Surface Scattering Model

Among the various theoretical models applied to study the electromagnetic wave scatterings from geophysical terrain, such as snow, ice, and vegetation canopy, the radiative transfer theory has drawn intensive attention in the microwave remote sensing society during the past years. In most of the scattering models, the volume scattering and the surface scattering effects have been investigated separately. Recently, there has been a growing interest in the construction of composite models which can take into account both types of scattering.

... ..

... ..

... ..

In this research, we study the first order iterative solution to the vector radiative transfer equations for a two-layer medium with a diffuse top boundary and an irregular bottom boundary of Gaussian roughness. The geometrical optics approach with shadowing correction is used in formulating the boundary conditions. To demonstrate the utilities of the theory, we apply our formula with a phase matrix for randomly oriented spheroidal discrete scatterers to calculate the backscattering coefficients from soybean field in different growing stages and compare the results with the experimental measurements. Good agreement has been achieved for both the co-polarized and the cross-polarized data. It is observed that the presence of the rough surface can significantly enhance the backscattering at small incident angles and the levels of the cross-polarized return. The polarization signatures calculated based on the Mueller matrix show a straight distortion track and an observable pedestal. Numerical comparison to the backscattering coefficients calculated by using planar bottom boundary conditions with or without the incoherent addition of the rough surface effects are also made in this work.

Radar Image Classification

Classification of terrain cover using polarimetric radar is an area of considerable current interest and research. A number of methods have been developed to classify ground terrain types from fully polarimetric synthetic aperture radar (SAR) images, and these techniques are often grouped into supervised and unsupervised approaches. Supervised methods, including both conventional Maximum Likelihood (ML) and more recent Multi-layer Perceptron classifiers, have yielded higher accuracy than unsupervised techniques, but suffer from the need for human interaction to predetermine classes and training regions. In contrast, unsupervised methods determine classes automatically, but generally show limited ability to accurately divide terrain into natural classes. In this research, a new terrain classification technique is introduced, utilizing unsupervised neural networks to provide automatic classification, but employing an iterative algorithm which overcomes the poor accuracy of other unsupervised techniques.

Several types of unsupervised neural networks are first applied to the classification of SAR images, and the results are compared with those of more conventional unsupervised methods. Neural Network approaches include Adaptive Resonance theory (ART), Learning Vector Quantization (LVQ), and Kohonen's self-organizing feature map. Conventional classifiers utilized are the migrating means clustering algorithm and the K-means clustering method. With both neural network and conventional classifiers, preprocessing is performed to reduce speckle noise and to stabilize the training process. Results show that LVQ is the best of the neural network techniques, and that

this method outperforms all of the conventional unsupervised classifiers. The accuracy of even the LVQ technique, however, is seen to remain below that of supervised methods.

To overcome this poor accuracy, an iterative algorithm is proposed in which the SAR image is reclassified using a Maximum Likelihood (ML) classifier. Training of the ML classifier is performed using a training data set first classified by the above unsupervised method, thus, requiring no human intervention, and preserving the unsupervised nature of the overall classification scheme. The process is then repeated iteratively, training a second ML classifier using data classified by the first. It is shown that this algorithm converges rapidly, and significantly improves classification accuracy. Performance after convergence is seen to be comparable to that obtained with a supervised ML classifier, while maintaining the advantages of an unsupervised technique.

The new unsupervised and iterative algorithm developed in this research is applied to polarimetric SAR images of San Francisco and Beaufort sea ice, acquired by the Jet Propulsion Laboratory. The results obtained for this imagery using the new algorithm are compared with the results obtained with other techniques, and also with those obtained with single-feature classification. It is found in each case that the new fully polarimetric unsupervised algorithm yields classified images which compare closely with those obtained from optimally chosen, supervised algorithms.



PUBLICATIONS SUPPORTED BY NASA CONTRACT NAGW-1617

Refereed Journal Articles and Conference Papers

Radiative Transfer theory for polarimetric remote sensing of pine forest (H. C. Hsu, H. C. Han, R. T. Shin, J. A. Kong, A. Beaudoin, and T. Le Toan,) *International Geoscience and Remote Sensing Symposium*, Houston, Texas, May 26–29, 1992.

Application of theoretical models to active and passive remote sensing of saline ice (H. C. Han, J. A. Kong, R. T. Shin, S. V. Nghiem, and R. Kwok), *International Geoscience and Remote Sensing Symposium*, Houston, Texas, May 26–29, 1992.

Radiative transfer theory for polarimetric remote sensing of pine forest (C. C. Hsu, H. C. Han, R. T. Shin, J. A. Kong, A. Beaudoin, and T. Le Toan), submitted to the *International Journal of Remote Sensing*, 1992.

Scattering of electromagnetic waves from a dense medium consisting of correlated Mie scatterers with size distributions and applications to dry snow (L. Tsang and J. A. Kong), *Journal of Electromagnetic Waves Applications*, Vol. 6, No. 3, 265–286, 1992.

Variance of phase fluctuations of waves propagation through a random medium (N. C. Chu, J. A. Kong, H. A. Yueh, and S. V. Nghiem), *Journal of Electromagnetic Waves Applications*, Vol. 6, No. 2, 169–197, 1992

Theoretical modeling for passive microwave remote sensing of earth terrain (J. A. Kong), URSI Specialists Meeting on Microwave Radiometry and Remote Sensing, Boulder, Colorado, January 24–26, 1992.

Polarimetric signatures of a canopy of dielectric cylinders based on first and second order vector radiative transfer theory (L. Tsang, C. H. Chan, J. A. Kong, J. Joesph), *Journal of Electromagnetic Waves Applications*, Vol. 6, No. 1, 19–51, 1992.

Branching model for polarimetric remote sensing of vegetation (S. H. Yueh, J. A. Kong, J. K. Jao, S. Ayasli, and R. T. Shin), *Progress in Electromag. Research Symposium*, Cambridge, Massachusetts, July 1–5, 1991.

Branching model for vegetation (S. H. Yueh, J. A. Kong, J. K. Jao, and R. T. Shin), *Progress in Electromag. Research Symposium*, Cambridge, Massachusetts, July 1–5, 1991.

Radiative transfer modelling of vegetation clusters (C. C. Hsu, S. H. Yueh, H. C. Han, R. T. Shin, and J. A. Kong), *Progress in Electromag. Research Symposium*, Cambridge, Massachusetts, July 1–5, 1991.



Application of neural network to polarimetric SAR image classification (Y. Hara, R. G. Atkins, S. H. Yueh, R. T. Shin, J. A. Kong, and R. Kwok), *Progress in Electromag. Research Symposium*, Cambridge, Massachusetts, July 1-5, 1991.

Multiple ellipsoidal species in layer random medium model for polarimetric remote sensing (S. V. Nghiem, J. A. Kong, R. T. Shin, and T. Le Toan), *Progress in Electromag. Research Symposium*, Cambridge, Massachusetts, July 1-5, 1991.

Polarimetric passive remote sensing of an azimuthally asymmetric periodic soil surface (S. V. Nghiem, M. E. Veysoglu, J. A. Kong, R. T. Shin, K. O'Neill, and A. Lohanick), *Progress in Electromag. Research Symposium*, Cambridge, Massachusetts, July 1-5, 1991.

Polarimetric passive remote sensing of periodic surfaces (M. E. Veysoglu, H. A. Yueh, R. T. Shin, and J. A. Kong), *Progress in Electromag. Research Symposium*, Cambridge, Massachusetts, July 1-5, 1991.

Analytical solution of the vector radiative transfer equation with rough surface boundary condition (H. C. Han, J. A. Kong, S. V. Nghiem, and T. Le Toan), *Progress in Electromag. Research Symposium*, Cambridge, Massachusetts, July 1-5, 1991.

Radiative transfer theory for passive microwave remote sensing (H. C. Han, W. Au, S. H. Yueh, R. T. Shin, and J. A. Kong), *Progress in Electromag. Research Symposium*, Cambridge, Massachusetts, July 1-5, 1991.

Application of random medium model to remote sensing of vegetation (T. Le Toan, S. V. Nghiem, J. A. Kong, H. C. Han,) *International Geoscience and Remote Sensing Symposium (IGARSS'91)*, Helsinki University of Technology, Espoo, Finland, June 3-6, 1991.

Application of neural networks to sea ice classification using polarimetric SAR images (R. Kwok, Y. Hara, R. G. Atkins, S. H. Yueh, R. T. Shin, and J. A. Kong), *International Geoscience and Remote Sensing Symposium (IGARSS'91)*, Helsinki University of Technology, Espoo, Finland, June 3-6, 1991.

External calibration of polarimetric radars using point and distributed targets (S. H. Yueh, J. A. Kong, and R. T. Shin), *Second Annual JPL Airborne Geoscience Workshop*, JPL, Pasadena, California, May 20-24, 1991.

Simulation of electromagnetic phenomena using a finite difference-time domain technique (K. Li, M. A. Tassoudji, R. T. Shin, and J. A. Kong), *7th Annual Review of Progress in Applied Computational Electromagnetics*, Naval Postgraduate School, Monterey, 38-55, March 18-22, 1991.

Electromagnetic scattering of waves by random rough surface: a finite-difference time-domain approach (C. H. Chan, S. H. Lou, L. Tsang, and J. A. Kong), *Microwave and Optical Technology Letters*, Vol. 4, No. 9, 355-359, 1991.

Branching Model for Vegetation (S. H. Yueh, J. A. Kong, J. K. Jao, R. T. Shin, and T. Le Toan), *IEEE Trans. Geosci. Remote Sensing*, Vol. 30, No. 2, 390-402, March 1991.



Electromagnetic wave modeling for remote sensing (S. V. Nghiem, J. A. Kong, and T. Le Toan), *International Conference on Directions in Electromagnetic Wave Modeling*, New York, October 22-24, 1990.

Inversion of permittivity and conductivity profiles employing transverse-magnetic polarized monochromatic data (T. M. Habashy, M. Moldoveanu, and J. A. Kong), *SPIE's 1990 International Symposium on Optical and Optoelectronic Applied Science and Engineering*, San Diego, California, July 8-13, 1990.

Polarimetric passive remote sensing of periodic surfaces (M. E. Veysoglu, H. A. Yueh, R. T. Shin, and J. A. Kong), *J. Electromagnetic Waves and Applications*, Vol. 5, No. 3, 267-280, 1991.

Polarimetric passive remote sensing of a periodic soil surface: microwave measurements and analysis (S. V. Nghiem, M. E. Veysoglu, J. A. Kong, R. T. Shin, K. O'Neill, and A. W. Lohanick), accepted for publication in *J. Electromagnetic Waves and Applications*, 1991.

Application of neural networks to radar image classification (Y. Hara, R. G. Atkins, S. H. Yueh, R. T. Shin, and J. A. Kong), submitted for publication in *IEEE Trans. Geosci. Remote Sensing*, 1991.

Calibration of polarimetric radars using in-scene reflectors, (S. H. Yueh, J. A. Kong, and R. T. Shin), *Progress In Electromagnetic Research*, edited by J. A. Kong, Vol. 3, Ch. 9, 451-510, Elsevier, New York, 1990.

Classification and maximum contrast of earth terrain using polarimetric synthetic aperture radar images, (J. A. Kong, S. H. Yueh, H. H. Lim, R. T. Shin, and J. J. van Zyl), *Progress In Electromagnetic Research*, edited by J. A. Kong, Vol. 3, Ch. 6, 327-370, Elsevier, New York, 1990.

K-distribution and polarimetric terrain radar clutter (S. H. Yueh, J. A. Kong, J. K. Jao, R. T. Shin, H. A. Zebker, T. Le Toan, and H. Öttl), *Progress In Electromagnetic Research*, edited by J. A. Kong, Vol. 3, Ch. 4, 237-275, Elsevier, New York, 1990.

Polarimetric remote sensing of geophysical media with layer random medium model (S. V. Nghiem, M. Borgeaud, J. A. Kong, and R. T. Shin), *Progress in Electromagnetic Research*, edited by J. A. Kong, Vol. 3, Ch. 1, 1-73, Elsevier, New York, 1990.

Application of layered random medium model to polarimetric remote sensing of vegetation (S. V. Nghiem, J. A. Kong, and T. LeToan), *URSI International Commission F meeting*, Hyannis, Massachusetts, May 16-18, 1990.

Calibration of polarimetric radars using in-scene reflectors (S. H. Yueh, J. A. Kong, and R. T. Shin), *10th International Geoscience & Remote Sensing Symposium (IGARSS'90)*, College Park, Maryland, May 20-24, 1990.

Correlation function for a random collection of discrete scatterers (H. H. Lim, S. H. Yueh, R. T. Shin, and J. A. Kong), *10th International Geoscience & Remote Sensing Symposium (IGARSS'90)*, College Park, Maryland, May 20-24, 1990.

Statistical modelling for polarimetric remote sensing of earth terrain (S. H. Yueh, J. A. Kong, R. T. Shin, and H. A. Zebker), *10th International Geoscience & Remote Sensing Symposium (IGARSS'90)*, College Park, Maryland, May 20–24, 1990.

Study of polarimetric response of sea ice with layered random medium model (S. V. Nghiem, J. A. Kong, and R. T. Shin), *10th International Geoscience & Remote Sensing Symposium (IGARSS'90)*, College Park, Maryland, May 20–24, 1990.

Measurements of sea-state bias at Ku and C bands (W. K. Melville, J. A. Kong, R. H. Stewart, W. C. Keller, D. Arnold, A. T. Jessup, and E. Lamarre), *URSI International Commission F meeting*, Hyannis, Massachusetts, May 16–18, 1990.

Measurements of EM bias at Ku and C bands (W. K. Melville, D. V. Arnold, J. A. Kong, A. T. Jessup, E. Lamarre, R. H. Stewart, and W. C. Keller), *OCEANS'90*, Washington, D.C., September 24–26, 1990.

Analysis of diffraction from chiral gratings (S. H. Yueh and J. A. Kong), *J. Electromagnetic Waves and Applications*, Vol. 5, No. 7, 701–714, 1991.

Principles of VLF antenna array design in magnetized plasmas (H. C. Han, J. A. Kong, T. M. Habashy, and M. D. Grossi), *URSI National Radio Science Meeting*, Boulder, Colorado, USA, January 3–5, 1990.

Theoretical models and experimental measurements for polarimetric remote sensing of snow and sea ice (S. V. Nghiem, J. A. Kong, R. T. Shin, H. A. Yueh, and R. Onstott), *URSI International Commission F meeting*, Hyannis, Massachusetts, May 16–18, 1990.

A neural net method for high range resolution target classification (R. G. Atkins, R. T. Shin, and J. A. Kong), *Progress In Electromagnetics Research*, edited by J. A. Kong, Vol. 4, Ch. 7, 255–292, Elsevier, New York, 1990.

Scattering from randomly oriented scatterers with strong permittivity fluctuations (H. A. Yueh, R. T. Shin, and J. A. Kong) *J. Electromagnetic Waves and Applications*, Vol. 4, No. 10, 983–1004, 1990.

K-distribution and multi-frequency polarimetric terrain radar clutter (H. A. Yueh, J. A. Kong, R. T. Shin, H. A. Zebker, and T. Le Toan), *J. Electromagnetic Waves and Applications*, Vol. 5, No. 1, 1–15, 1991.

Polarimetric remote sensing of earth terrain with two-layer random medium model (M. Borgeaud, J. A. Kong, R. T. Shin, and S. V. Nghiem), *Progress in Electromagnetics Research Symposium*, Boston, Massachusetts, July 25–26, 1989.

Theoretical prediction of EM bias (D. V. Arnold, J. A. Kong, W. K. Melville, and R. W. Stewart), *Progress in Electromagnetics Research Symposium*, Boston, Massachusetts, July 25–26, 1989.



Phase fluctuations of waves propagating through a random medium (N. C. Chu, S. V. Nghiem, R. T. Shin, and J. A. Kong) *Progress in Electromagnetics Research Symposium*, Boston, Massachusetts, July 25-26, 1989.

Correlation function study for random media with multiphase mixtures (F. C. Lin, H. A. Yueh, J. A. Kong, and R. T. Shin), *Progress in Electromagnetics Research Symposium*, Boston, Massachusetts, July 25-26, 1989.

Three-layer random medium model for fully polarimetric remote sensing of geophysical media (S. V. Nghiem, F. C. Lin, J. A. Kong, R. T. Shin, and H. A. Yueh), *Progress in Electromagnetics Research Symposium*, Boston, Massachusetts, July 25-26, 1989.

Faraday polarization fluctuations in transionospheric polarimetric VLF waves (S. V. Nghiem and J. A. Kong), *Progress in Electromagnetics Research Symposium*, Boston, Massachusetts, July 25-26, 1989.

Calibration of polarimetric radars using in-scene reflectors (H. A. Yueh, J. A. Kong, R. M. Barnes, and R. T. Shin), *Progress in Electromagnetics Research Symposium*, Boston, Massachusetts, July 25-26, 1989.

K-distribution and polarimetric terrain radar clutter (H. A. Yueh, J. A. Kong, J. K. Jao, R. T. Shin, and L. M. Novak), *Progress in Electromagnetics Research Symposium*, Boston, Massachusetts, July 5-26, 1989.

Contrast and classification studies of polarimetric SAR images for remote sensing of earth terrain (H. H. Lim, H. A. Yueh, J. A. Kong, R. T. Shin, and J. J. van Zyl), *Progress in Electromagnetics Research Symposium*, Boston, Massachusetts, July 25-27, 1989.

The measurement and modelling of sea-state bias in SAXON (W. K. Melville, J. A. Kong, R. H. Stewart, W. C. Keller, A. Jessup, D. V. Arnold, A. Slinn), *IGARSS'89 and 12th Canadian Symposium on Remote Sensing*, Vancouver, Canada, July 10-14, 1989.

Theoretical models for polarimetric microwave remote sensing of earth terrain (M. Borgeaud, S. V. Nghiem, R. T. Shin, and J. A. Kong), *J. Electromagnetic Waves and Application*, Vol. 3, No. 1, 61-81, 1989.

Application of three-layer random medium model to polarimetric remote sensing of snow and sea ice (S. V. Nghiem, J. A. Kong, R. T. Shin, and H. A. Yueh) *North American Sea Ice Work Shop*, Amherst, Massachusetts, June 26-28, 1989.

RADIATIVE TRANSFER THEORY FOR POLARIMETRIC REMOTE SENSING OF PINE FOREST

C. C. Hsu, H. C. Han, R. T. Shin, J. A. Kong

Massachusetts Institute of Technology, Cambridge, Massachusetts, USA

A. Beaudoin, and T. Le Toan

Centre d'Etude Spatiale des Rayonnements, Toulouse, France

Abstract— In this paper, the radiative transfer theory is applied to interpret polarimetric radar backscatter from pine forest with clustered vegetation structures. To take into account the clustered structures with the radiative transfer theory, the scattering function of each cluster is calculated by incorporating the phase interference of scattered fields from each component. Subsequently, the resulting phase matrix is used in the radiative transfer equations to evaluate the polarimetric backscattering coefficients from random medium layers embedded with vegetation clusters. Upon including the multi-scale structures, namely, trunks, primary and secondary branches, as well as needles, we interpret and simulate the polarimetric radar responses from pine forest for different frequencies and looking angles. The preliminary results are shown to be in good agreement with the measured backscattering coefficients at the Landes maritime pine forest during the MAESTRO-1 experiment.

I. Introduction

In recent years, the application of radar polarimetry for active remote sensing of the earth terrain has inspired extensive interests. A variety of theories have been used for electromagnetic modeling of geophysical terrain, such as snow, ice, and vegetation canopy [1]. Among these studies, the radiative transfer (RT) theory has been commonly used to calculate radar backscattering coefficients from layered geophysical media and to interpret the experimental measurements.

The radiative transfer theory consists of the radiative transfer equations which govern the electromagnetic energy propagation through scattering media. Various models have been developed based on this theory [2-4]. In general, the conventional RT theory ignores the relative phase information associated with structured scatterers, which may play an important role in the overall scattering behavior [5]. In forest, vegetation consists of structures of many different scale length — the trunk, primary branches, secondary branches, and needle leaves, etc. Vegetation elements of each scale are connected to elements of other scales in a fashion statistically described by the unique architecture pertaining to each tree species. For the microwave remote sensing of forest, the vegetation structures not only give rise to the separation of scattering centers for different polarizations, but also provide partially coherent scattering by different scatterers with statistically prescribed relative positions.

In this paper, a four-layer RT model is presented for the modeling of the pine forest in the Landes area, France.

We make use of the newly developed branching model for vegetation [7] to account for the scattering properties of structured pine trees. The model thus constructed has a wide validity range in frequency spectrum.

II. Radiative Transfer Theory

Consider an electromagnetic wave incident upon a multi-layered random medium with the incident angle θ_0 as shown in Fig. 1. The scattering regions 1 to 3 are layers of thickness h_n ($n = 1, 2, 3$), where discrete scatterers embedded in homogeneous background. The bottom boundary between region 4 and region t can be either a flat surface or a rough surface described by a Gaussian random process.

The vector radiative transfer equation for the specific intensity in each scattering region is of the form

$$\cos \theta \frac{d\bar{I}(\theta, \phi, z)}{dz} = -\bar{\kappa}_e(\theta, \phi, z) \cdot \bar{I}(\theta, \phi, z) + \int_{4\pi} d\Omega' \bar{P}(\theta, \phi; \theta', \phi') \cdot \bar{I}(\theta', \phi', z) \quad (1)$$

where the Stokes vector \bar{I} containing information regarding field intensity and phase relation of the two orthogonal polarizations is defined as

$$\bar{I} = \begin{pmatrix} I_h \\ I_v \\ U \\ V \end{pmatrix} = \frac{1}{\eta} \begin{pmatrix} \langle |E_h|^2 \rangle \\ \langle |E_v|^2 \rangle \\ 2 \operatorname{Re} \langle E_v E_h^* \rangle \\ 2 \operatorname{Im} \langle E_v E_h^* \rangle \end{pmatrix} \quad (2)$$

In (2), the subscripts h and v represent the horizontal and vertical polarizations, respectively. The angular bracket $\langle \rangle$ denotes ensemble average over the size and orientation distributions of scatterers; and $\eta = \sqrt{\mu_0/\epsilon_0}$ is the free-space characteristic impedance.

The extinction matrix $\bar{\kappa}_e$ represents the attenuation due to both the scattering and absorption, and can be obtained through the optical theorem in terms of forward scattering functions. The phase matrix $\bar{P}(\theta, \phi; \theta', \phi')$ characterizes the scattering of the Stokes vector from (θ', ϕ') direction into (θ, ϕ) direction. The phase matrix can be formulated in terms of scattering functions of the randomly distributed discrete scatterers. Along with the boundary conditions, we can solve the radiative transfer equations iteratively for the polarimetric backscattering coefficients [1].

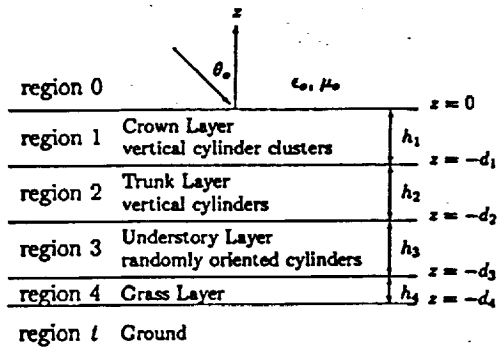


Figure 1. Configuration

III. Scattering Function for Clustered Structure

In order to take into account the partially coherent effect due to clustered vegetation structures, we formulate the phase matrix based on the branching model for vegetation. In pine forest, most of the scatterers are of cylindrical shapes. Hence in this study, the main subject is cylinder clusters. For the cylinder cluster that has one center cylinder and N branching cylinders, the total backscattering function $f_{\alpha\beta}$ is

$$f_{\alpha\beta} = f_{0\alpha\beta} + \sum_{n=1}^N f_{n\alpha\beta} e^{i\phi_n} \quad (3)$$

where $f_{0\alpha\beta}$ is the $\alpha\beta$ -th element of the scattering matrix for the center cylinder, and $f_{n\alpha\beta}$ is $\alpha\beta$ -th element of the scattering matrix for the n -th branching cylinder. $\alpha, \beta, \gamma, \delta$ represent horizontal or vertical polarization.

Assuming all the branching cylinders are identical and independent of each other, the correlation of f is

$$\begin{aligned} \langle f_{\alpha\beta} f_{\gamma\delta}^* \rangle &= \langle f_{0\alpha\beta} f_{0\gamma\delta}^* \rangle + N \langle f_{n\alpha\beta} f_{n\gamma\delta}^* \rangle \\ &+ 2N \operatorname{Re} \left[\langle f_{0\alpha\beta} \rangle \langle f_{n\gamma\delta}^* \rangle \langle e^{-i\phi_n} \rangle \right] \\ &+ N(N-1) \langle f_{m\alpha\beta} \rangle \langle f_{n\gamma\delta}^* \rangle \\ &\cdot \langle e^{i\phi_m} \rangle \langle e^{-i\phi_n} \rangle \end{aligned} \quad (4)$$

The relative phase of the n -th branch with respect to the center cylinder is defined as

$$\phi_n = (\bar{k}_i - \bar{k}_s) \cdot \bar{r}_n$$

where \bar{k}_i and \bar{k}_s are the incident and scattered wave vectors, respectively. \bar{r}_n is the location of the n -th branching cylinder relative to the center cylinder.

In (4), the third and fourth terms are the coherent terms. It can be seen that the incoherent approximation is valid when the average of the random phase factor $\langle e^{i\phi_j} \rangle$ is so small that the coherent terms are negligible as compared with the incoherent terms. However, this is not true for vegetation structure with scale length comparable with wavelength.

For the calculation of scattered fields of different cluster elements, dielectric cylinders can be used to model trunks, branches and coniferous leaves [6,7]. Leaves of deciduous tree can be modelled as disks [6,8]. The truncated infinite cylinder approximation [9] is employed in this study to calculate scattered fields from cylinders.

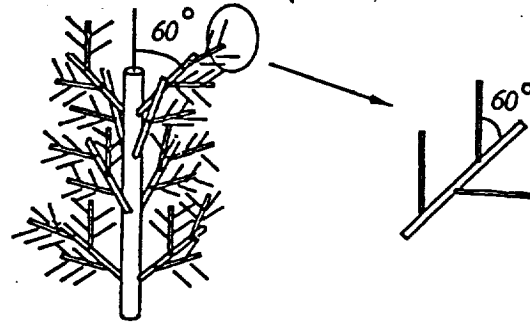


Figure 2. Cylinder Cluster

IV. Comparison with Experimental Data

The experiment is conducted by the Centre d'Etude Spatiale des Rayonnements (CESR) at the Landes forest, in southwest France, using the NASA/JPL Synthetic Aperture Radar (SAR) during the MAESTRO-1 campaign in August 1989. A strong correlation between P-band backscattering coefficients and pine forest parameters has been observed in the measurement data [10].

To model the pine forest, the RT model described in previous sections is adopted as depicted in Fig. 1. The top layer (region 1) consists of vertically orientated three-scale dielectric cylinder clusters characterizing the trunks and the attached smaller scale branching clusters. These smaller scale branching clusters include primary and secondary branches, as well as needles. However, at P-band, only the primary and secondary branches are important. In the three-scale model, all the smaller scale cylinders are uniformly distributed along a larger scale center cylinder with 60° angle relative to the orientation of the center cylinder, as show in Fig. 2. Region 2 contains vertically oriented dielectric cylinders representing tree trunks. In region 3, vertical cylinders and randomly oriented thin cylinders coexist characterizing a mixture of the tree trunks and the short vegetation in the forest understory. The underlying grass/ground consists of the attenuating grass layer and the ground.

With this model, we calculate backscattering coefficients for six pine stands of different ages. The ages of the forest under investigation are 6, 14, 20, 30, 38, and 46 years old. It is observed that as forest becomes aged, the average radius of tree trunk grows bigger and the average tree height also becomes taller. The primary and secondary branches grow bigger as well. In general, the above-ground biomass increases despite the decrease in the number of trees per unit area as forest ages. Since the ground truth indicates that the surface is very smooth for observation at P-band, we model the ground as a planar surface. The grass layer above the ground is considered as an homogeneous attenuating layer of 0.2m height and characterized by a dielectric constant $(1.05 + i0.5)$. The calculated results for P-band are shown in Fig. 3. The discrete points are the data collected by SAR; the curves are the theoretical results. It is found from the simulations, the main contribution for HH backscattering coefficient is from trunk-ground interaction and scattering from branches. As for the VV and HV, the branches are the dominate scatterers.

V. Conclusions

Radiative transfer theory is applied to the modeling of polarimetric radar backscatter for vegetation canopy. The phase matrix is derived with the coherent effects due to the clustered structures. With this model, we simulate multi-frequency and multi-angular backscattering coefficients at different radar polarizations. Theoretical results are in good agreement with the measurement data collected by NASA/JPL SAR. This paper presents the comparison performed at P-Band frequency.

Acknowledgments

This work was supported by the NASA Grant No. NAGW-1617, the NASA Contract No. 958461, the ESA Contract No. AO/1-2413/90/NL/PB, and the ONR Contract No. N00014-89-J-1107.

References

- [1] Tsang, L., J. A. Kong, and R. T. Shin, *Theory of Microwave Remote Sensing*, Wiley-Interscience, New York, 1985.
- [2] Han, H. C., S. V. Nghiem, and J. A. Kong, "Analytical solution of vector radiative transfer equation with rough surface boundary condition," *Progress in Electromagnetics Research Symposium*, Cambridge, Massachusetts, 1991.
- [3] Shin, R. T., and J. A. Kong, "Radiative transfer theory for active remote sensing of two-layer random medium," *Progress in Electromagnetic Research*, Vol. 1, Chapter 4, ed. by J. A. Kong, Elsevier, New York, 1989.
- [4] Tsang, L., J. A. Kong, and R. T. Shin, "Radiative transfer theory for active remote sensing of a layer of nonspherical particles," *Radio Science*, Vol. 19, 629-642, 1984.
- [5] Yueh, S. H., J. A. Kong, J. K. Jao, R. T. Shin, and T. Le Toan, "Branching model for vegetation," *IEEE Trans. Geosci. Remote Sensing*, Vol. GE-30, No. 2, 1992.
- [6] Karam, M. A., A. K. Fung, and Y. M. M. Antar, "Electromagnetic wave scattering from some vegetation samples," *IEEE Trans. Geosci. Remote Sensing*, Vol. GE-26, No. 6, 799-808, 1988.
- [7] Durden, S. L., J. J. van Zyl, and H. A. Zebker, "Modeling and observation of the radar polarization signature of forested areas," *IEEE Trans. Geosci. Remote Sensing*, Vol. GE-27, No. 3, 290-301, 1989.
- [8] Lang, R. H., and H. A. Saleh, "Microwave inversion of leaf area and inclination angle distribution from backscattered data," *IEEE Trans. Geosci. Remote Sensing*, Vol. GE-23, No. 5, 685-694, 1985.
- [9] van de Hulst, H. C., *Light Scattering by Small Particles*, Dover, New York, 1981.
- [10] Le Toan, T., A. Beaudoin, J. Riom, and D. Guyon, "Relating forest biomass to SAR data," *IEEE Trans. Geosci. Remote Sensing*, Vol. GE-30, No. 2, 1992.

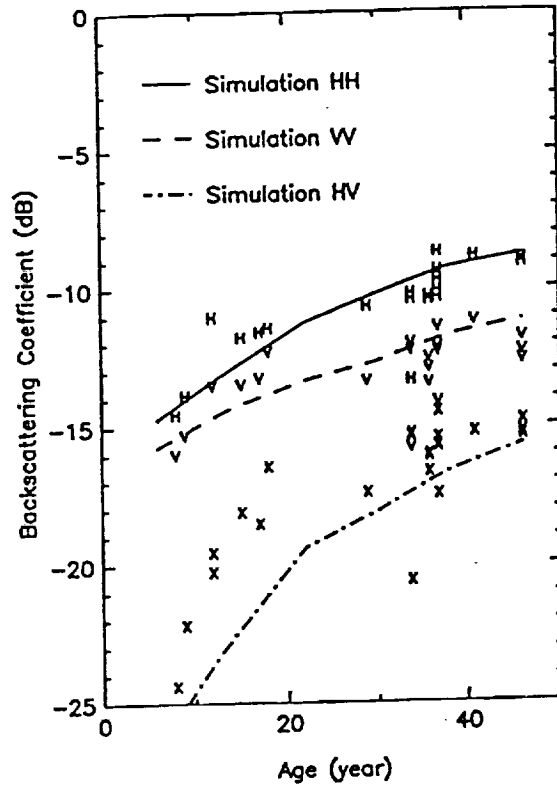


Figure 3. Backscattering for P-band



APPLICATION OF THEORETICAL MODELS
TO ACTIVE AND PASSIVE REMOTE SENSING OF SALINE ICE

N93-13086

H. C. Han, J. A. Kong, R. T. Shin
Massachusetts Institute of Technology, Cambridge, Massachusetts

S. V. Nghiem, and R. Kwok
Jet Propulsion Laboratory, California Institute of Technology, Pasadena, California

Abstract— The random medium model is used to interpret the polarimetric active and passive measurements of saline ice. The ice layer is described as a host ice medium embedded with randomly distributed inhomogeneities, and the underlying sea water is considered as a homogeneous half-space. The scatterers in the ice layer are modeled with an ellipsoidal correlation function. The orientation of the scatterers is vertically aligned and azimuthally random. The strong permittivity fluctuation theory is employed to calculate the effective permittivity and the distorted Born approximation is used to obtain the polarimetric scattering coefficients. We also calculate the thermal emissions based on the reciprocity and energy conservation principles. The effects of the random roughness at the air-ice, and ice-water interfaces are accounted for by adding the surface scattering to the volume scattering return incoherently. The above theoretical model, which has been successfully applied to analyze the radar backscatter data of the first-year sea ice near Point Barrow, AK, is used to interpret the measurements performed in the CRRELEX program.

interfaces, and add incoherently to the volume scattering return obtained with the distorted Born approximation. This model has been successfully applied to study the radar backscatter for the thick first-year sea ice data measured near Point Barrow, Alaska [5]. In this study, we further employ this model to interpret the multi-frequency active and passive measurements taken during the CRRELEX experiment.

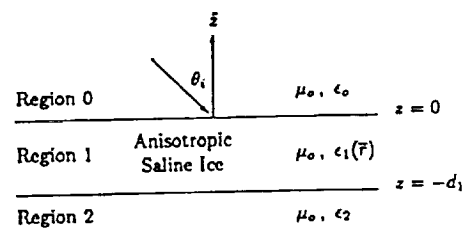


Figure 1 Scattering configuration.

INTRODUCTION

Understanding electromagnetic wave interaction with saline ice provides physical insight for interpretation of active and passive remote sensing data of sea ice. Various theoretical models have been developed to characterize the scattering and the emission properties of sea ice [1]. In this paper, the random medium model [2] is used to interpret the measurement data collected at the US Army Cold Regions Research and Engineering Laboratory (CRREL) under the CRRELEX program. To simulate sea ice, saline ice was grown under partially controlled condition at CRREL and active and passive microwave signatures of the saline ice were measured together with ice characteristic parameters.

Under quiescent condition, the background ice grows in columnar form and saline water is trapped between ice platelets in the form of brine inclusions which are usually ellipsoidal. The ice tends to grow vertically downward rendering the ellipsoidal inclusions aligned preferably in the vertical direction and the crystallographic c-axes parallel to the horizontal plane. In this case, the c-axes are, however, random in the horizontal direction. The saline ice layer is modeled as a random medium containing ellipsoidal scatterers vertically aligned but randomly oriented in the horizontal direction. The strong fluctuation theory is employed to calculate the effective permittivity and the distorted Born approximation is used to obtain the polarimetric scattering coefficients. The emissivity of a layer of sea ice overlying sea water can be obtained through the principles of reciprocity and energy conservation [3]. In other words, the emissivity is obtained as one minus the reflectivity. To account for the effects of rough interfaces, we use small perturbation method [4] to evaluate the surface scattering from air-ice, and ice-water

MODEL DESCRIPTION

Multi-Layered Random Medium Model

The fully polarimetric multi-layered random medium model for sea ice has been developed with the wave theory. The layer configuration is shown in Fig. 1. Region 0 represents the homogeneous air above sea ice. The sea ice in region 1 contains vertically aligned ellipsoidal scatterers such as saline ice with brine pockets or air bubbles which has spatially varying permittivity $\epsilon_1(\vec{r})$. Region 2 is the underlying sea water with homogeneous permittivity ϵ_2 . All three regions are assumed to have the free-space permeability μ_0 .

An exponential correlation function locally corresponding to a scatterer is used in the derivation of the effective permittivity with the strong fluctuation theory extended to account for the ellipsoidal shape and the horizontally random orientation of the scatterers. The local correlation function of the brine inclusion has three different correlation lengths related to the three different axial lengths of the ellipsoid as shown in Fig. 2. The azimuthal orientation of the scatterer is depicted locally with the local z' -axis parallel to the global z -axis and an Eulerian fluctuation angle ϕ_f corresponding to the angle between the c -axis and the global horizontal axis (x -axis). When the average process is performed over the random orientation angle ϕ_f , the effective permittivity is a uniaxial tensor with vertical optic axis describing the effective azimuthal symmetry of the inhomogeneous sea ice. When a single set of correlation lengths is used, for simplicity, to model the brine inclusions with various sizes, these correlation lengths are considered as related to the effective size of the scatterers. After the effective permittivity of the sea ice is calculated, the complete set of polarimetric scattering coefficients are obtained under the distorted Born

approximation with the anisotropic dyadic Green's function for the layer media. From the scattering coefficients, the Mueller matrix is computed to plot the polarization signatures of sea ice.

Under the distorted Born approximation the polarimetric scattering coefficients, obtained as the correlation of the scattered field, takes the form

$$\begin{aligned} \langle \bar{E}_{0s}(\bar{r}) \cdot \bar{E}_{0s}^*(\bar{r}) \rangle = & \sum_{i,j,k,l,m} k_o^4 \int_0^{2\pi} d\phi_f p(\phi_f) \int_{V_1} d\bar{r}_1 \int_{V_1} d\bar{r}'_1 C_{\xi_{njklm}}(\bar{r}_1, \bar{r}'_1; \phi_f) \\ & \left[\langle G_{01ij}(\bar{r}, \bar{r}_1) \rangle \langle F_{1k}(\bar{r}_1) \rangle \right] \cdot \left[\langle G_{01il}(\bar{r}, \bar{r}'_1) \rangle \langle F_{1m}(\bar{r}'_1) \rangle \right]^* \end{aligned} \quad (1)$$

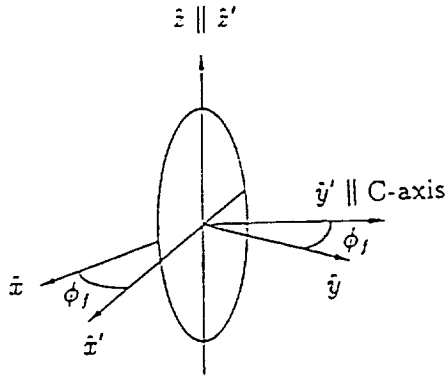


Figure 2 Geometry of scatterer in region 1.

where the uniaxial effective permittivity $\bar{\epsilon}_{eff1}$ for region 1 is used to calculate the mean dyadic Green's functions and the mean fields $\langle \bar{F}_1(\bar{r}) \rangle$. The correlation function for region 1, $C_{\xi_{1jklm}}(\bar{r}_1, \bar{r}'_1; \phi_f)$ in (1) is the $jklm$ -th element of fourth-rank correlation tensor $\bar{C}_{\xi_1}(\bar{r}_1, \bar{r}'_1; \phi_f)$ defined as

$$C_{\xi_{1jklm}}(\bar{r}_1, \bar{r}'_1; \phi_f) = \langle \xi_{1jk}(\bar{r}_1) \xi_{1lm}^*(\bar{r}'_1) | \phi_f(\bar{r}_1) \rangle \quad (2)$$

In (1), the probability density function of scatterer orientation $p(\phi_f)$ is simply

$$p(\phi_f) = \frac{1}{2\pi} \quad (3)$$

for complete random orientation horizontally with no preference in azimuthal direction, and $k_o = \omega \sqrt{\mu_o \epsilon_o}$ is the free-space wavenumber with angular frequency ω .

Effective Permittivities

The strong fluctuation theory is used to derive the effective permittivities of the ice layer. The singularities of the dyadic Green's functions in the bilocal approximated Dyson's equations are accounted for; and the low-frequency approximation is applied to obtain the results for the anisotropic sea ice media. The derivations are done in the frequency domain with the Fourier-transform method.

The ice layer is described with a normalized local correlation function of the form

$$R_{\xi_1}(\bar{r}) = \exp \left(- \sqrt{\frac{x^2}{\ell_x^2} + \frac{y^2}{\ell_y^2} + \frac{z^2}{\ell_z^2}} \right) \quad (4)$$

with correlation length ℓ_x , ℓ_y , and ℓ_z in the local coordinates corresponding to the minor, the meridian, and the major axes of

the scatterer. In this model, the correlation lengths are related to the effective size and shape of the scatterers. The effective permittivity of the ice layer is composed of a quasi-static part and a scattering part which accounts for the modification in the wave speed and attenuation

$$\bar{\epsilon}_{eff1} = \bar{\epsilon}_{g1} + \epsilon_o \left[\bar{I} - \bar{\xi}_{eff1} \cdot \langle \bar{S}_1 \rangle \right]^{-1} \cdot \bar{\xi}_{eff1} \quad (5)$$

The effective dyadic scatterer $\bar{\xi}_{eff1}$ is obtained from the volume integration of the dyadic Green's function and the correlation function, the auxiliary permittivity $\bar{\epsilon}_{g1}$ and dyadic coefficient \bar{S}_1 characterizing the source singularity of the dyadic Green's function are determined by the condition of secular term elimination.

Scattering Coefficients

For polarimetric backscattering, the scattering coefficients are defined by

$$\sigma_{\mu\tau\nu\kappa} = \lim_{\substack{r \rightarrow \infty \\ A \rightarrow \infty}} \frac{4\pi r^2 \langle E_{\mu s} E_{\nu s}^* \rangle}{A E_{\tau i} E_{\kappa i}^*} \quad (6)$$

where A is the illuminated area, subscript i is for the incident wave, s represents the scattered wave, and μ , ν , τ , and κ can be h or v which respectively stands for the horizontal or vertical components of the electric fields. The components of the scattered field in (6) are obtained by measuring the h and the v returns while the incident field is transmitted exclusively with h or v polarization. For backscattering from reciprocal media, the h return obtained by transmitting v is the same as the v return obtained by transmitting h .

Rough Surface Contribution

To account for the effects of rough interfaces at $z = 0$ and $z = -d_1$, we first approximate the surface statistics by a Gaussian correlation function with standard deviation σ and correlation length ℓ , then employ the small perturbation method to obtain the first-order backscattering field from the interfaces. For example, the surface scattering from the air-ice interface is given by

$$\sigma_{hh} = 4k_o^4 \sigma^2 \ell^2 \cos^4 \theta_i \left| R_{01}^{TE} \right|^2 e^{-k_o^2 \ell^2 \sin^2 \theta_i} \quad (7a)$$

$$\begin{aligned} \sigma_{vv} = & 4k_o^8 \sigma^2 \ell^2 \cos^4 \theta_i \\ & \times \left| \frac{(k_1^2 - k_o^2)(k_1^2 \sin^2 \theta_i + k_{1z}^2)}{(k_1^2 k_z + k_o^2 k_{1z})^2} \right|^2 e^{-k_o^2 \ell^2 \sin^2 \theta_i} \end{aligned} \quad (7b)$$

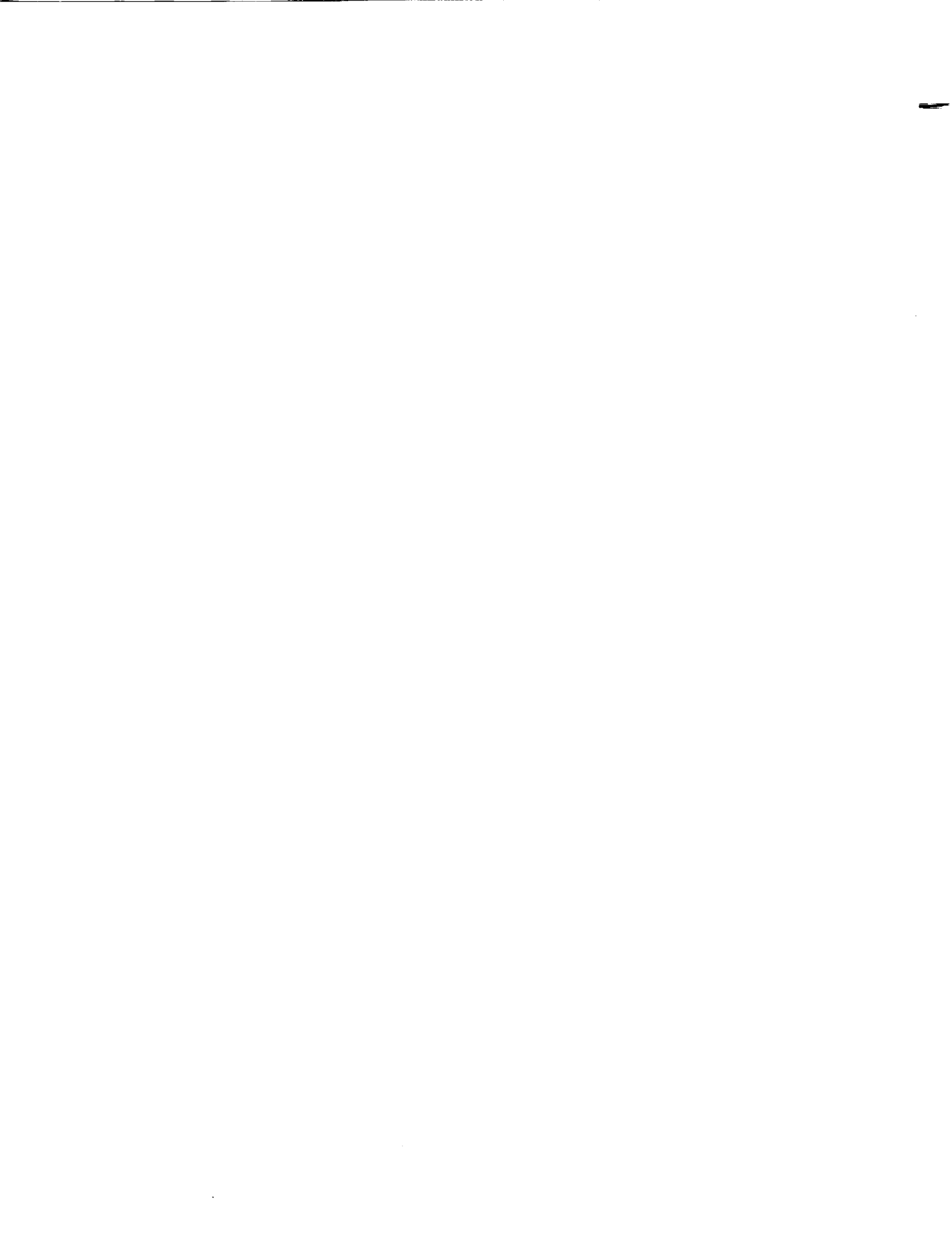
where θ_i and k_1 denote the angle of incidence and the wavenumber for the ice layer, respectively. The surface scattering is incoherently added to the volume scattering return calculated based on the method described previously.

Emissivities

The Kirchhoff law is invoked to obtain the emissivity of sea ice under isothermal condition from the active bistatic scattering coefficients.

$$e_h(\theta, \phi) = 1 - \frac{1}{4\pi} \sum_{b=h,v} \int_{4\pi} d\Omega' \gamma_{bh}(\theta', \phi'; \theta, \phi) \quad (8a)$$

$$e_v(\theta, \phi) = 1 - \frac{1}{4\pi} \sum_{b=h,v} \int_{4\pi} d\Omega' \gamma_{bv}(\theta', \phi'; \theta, \phi) \quad (8b)$$



where $\gamma_{hh}(\theta', \phi'; \theta, \phi)$ represents the bistatic scattering coefficient for an h -polarized incident wave propagating in the direction described by (θ, ϕ) and scattered into the (θ', ϕ') direction with b -polarization.

DATA INTERPRETATION

The theoretical results from the random medium model are compared to the CRRELEX data. For the case under consideration, region 0 is air, region 1 is the sea ice layer containing ellipsoidal brine inclusions, and region 2 is sea water. The thickness of the ice layer is obtained by ground truth measurement. The fractional volume of the brine inclusions is calculated from the bulk ice salinity and temperature. Results from publications are used to estimate the frequency-dependent permittivities of the ice background, the brine inclusions, and the underlying sea water. The theoretical calculations performed with and without the rough interfaces contributions are compared.

The local correlation lengths, which are not defined in the same manner as the global correlation lengths in the Perovich's estimation, corresponding to the effective size of the scatterers need to be determined. In our preliminary calculations, instead of adjusting the correlation lengths to match the experimental data, they are chosen from the characterization of the first-year sea ice obtained by a comparison with the 9 GHz measurements made at Point Barrow, Alaska [2]. This approach, based on the theoretical model, also serves the purpose of referring the remote sensing signatures of the saline ice artificially grown at CRREL to the sea ice in the natural conditions.

The theoretically calculated emissivities are in good agreement with the data. This indicates that the estimated effective permittivity tensor, which affects the emissivity even in the zeroth order, are close to that for natural sea ice. At lower frequencies where the electromagnetic wave can penetrate the ice, the emissivities can be sensitive to the ice thickness. In this case, the h polarization is more sensitive to the thickness than the v polarization which usually has higher attenuation. For information pertaining more to the first or higher order effects, active signatures should be considered.

The backscattering coefficients generated theoretically have also been compared with that observed in the CRRELEX experiment for co-polarized and cross-polarized returns only, since measurements of other elements in the covariance matrix are not available. At 5 GHz, the theoretical results overestimate the CRRELEX data at larger incident angles. This indicates that the local correlation lengths of the grown sea ice probably smaller than those observed at Point Barrow. At smaller incident angles, the measurements are higher than the theoretical values without rough surface contributions. At 10 GHz, the results, calculated using the above correlation lengths, are all higher than the measured values provided to us for the backscattering from the CRRELEX experiment.

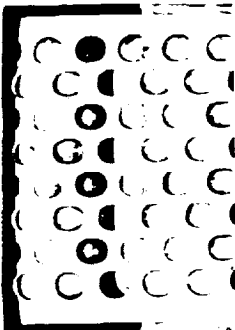
ACKNOWLEDGMENT

This work was supported by the ONR Contract No. N00014-89-J-1107, the NASA Grant No. NAGW-1617, and the NASA Contract No. 958461.

REFERENCES

- [1] L. Tsang, J. A. Kong, and R. T. Shin, *Theory of Microwave Remote Sensing*, Wiley-Interscience, New York, 1985.
- [2] S. V. Nghiem, "Electromagnetic wave models for polarimetric remote sensing of geophysical media," *Ph.D. Thesis*, Massachusetts Institute of Technology, Cambridge, Massachusetts, 1991.
- [3] W. H. Peake, "Interaction of electromagnetic waves with some natural surfaces," *IEEE Trans. Ant. Propagat.*, Vol. AP-7, 5324-5329, 1959.
- [4] J. A. Kong, *Electromagnetic Wave Theory*, Second edition, Wiley-Interscience, New York, 1990.
- [5] Y. S. Kim, R. K. Moore, and R. G. Onstott, "Theoretical and experimental study of radar backscatter from sea ice," *RSL Tech. Report*, 331-337, University of Kansas Center for Research, Inc., Lawrence, Kansas, 1984.

ORIGINAL PAGE IS
OF POOR QUALITY



Scattering of Electromagnetic Waves from a Dense Medium Consisting of Correlated Mie Scatterers with Size Distributions and Applications to Dry Snow

L. Tsang

Electromagnetics and Remote Sensing Laboratory
Department of Electrical Engineering
University of Washington
Seattle, WA 98195, USA

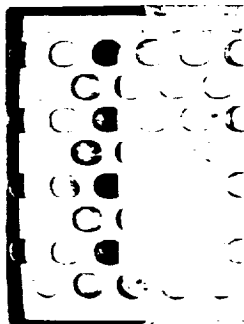
J. A. Kong

Department of Electrical Engineering and Computer Science
Massachusetts Institute of Technology
Cambridge, MA 02139, USA

Abstract— The scattering of a plane electromagnetic wave obliquely incident on a layer of dense medium consisting of dielectric spherical particles of finite sizes and with size distributions is studied. The spherical particles are of sizes comparable to wavelength so that Mie scattering is used to describe the single particle scattering characteristics. The coherent wave is studied with quasicrystalline approximation using the cross pair distribution functions of multiple sizes governed by Percus-Yevick approximation. The incoherent scattered wave is calculated with the distorted Born approximation with the result expressed in terms of a product of the T-matrices of particles of different sizes and permittivities and the Fourier transform of the cross pair distribution functions. The coherent wave effective propagation constants, the attenuation rates and the backscattering coefficients are illustrated numerically, with examples chosen to illustrate microwave and millimeter wave scattering from snow cover in the frequency range of 5 GHz to 95 GHz, and mean grain radius between 0.03 cm to 0.09 cm. Salient features of the numerical results for scattering from snow with size distribution are: 1. Correlated dense medium scattering is less than independent scattering at low frequency, a fact that is consistent with controlled laboratory experiment. 2. Scattering from dense medium of a Rayleigh size distribution with an average radius can be much larger than the case of monodisperse particles of the sizes identical to that average radius. 3. The scattering attenuation rate increases rapidly with frequency at low frequency regime and begins to level off at high frequency regime. 4. The coherent wave scattering attenuation rate is large in snow at frequencies above 15 GHz indicating large optical thickness and the importance of multiple scattering. Comparisons with extinction measurements of dry snow at 18 GHz, 35 GHz, 60 GHz, and 90 GHz are made.

I. INTRODUCTION

Propagation and scattering in dense media has applications in remote sensing of geophysical terrain and nondestructive evaluation of composite materials [1-13]. In a dense medium, particles occupy an appreciable fractional volume. A main feature of a medium with densely packed scatterers is that Foldy's approximation [14]

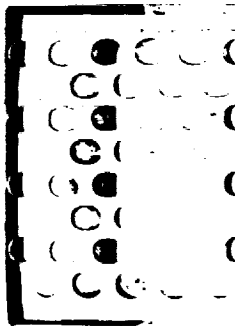
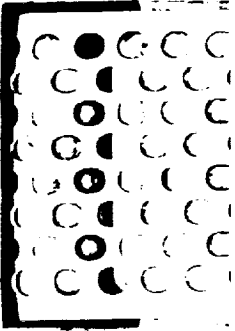


which has been successful in propagation problems through sparse media, is not applicable. It has been shown theoretically [1-2,4-6,9,15-16] and through laboratory experiments [3] that the effects of correlated scattering between scatterers must be taken into account.

Propagation and scattering in dense media has been studied with the quasicrystalline approximation [1-2,4-6], and the quasicrystalline approximation with coherent potential [6-8] for the first moment of the field and the correlated ladder approximation for the second moment of the field [7,9,13]. The dense medium theory is developed for media with particles of finite sizes. Because of the finite sizes of the particles, their positions are correlated. The dense medium radiative transfer theory has also been developed from these approximations to study multiple scattering effects in the incoherent wave. Some of the studies of correlated scattering have been limited to the case of low frequency [7,9] and/or particles of identical sizes [1-2,4-6,10-11]. However, to approximate physical reality in geophysical terrain scattering, size distributions of particles must be taken into account. The case of monodisperse particles and polydisperse scattering generally can give different results for independent scattering [14,17] as well as correlated scattering [8,16]. High frequency results are also important for example at frequencies above 15 GHz for snow cover.

In this paper, we study the scattering of a plane electromagnetic wave obliquely incident on a layer of dense medium consisting of dielectric spherical particles with size distributions. The spherical particles are of sizes comparable to wavelength so that Mie scattering is used to describe the single particle scattering characteristics. Thus the theory is applicable to particles of arbitrary size. The coherent wave is studied with the quasicrystalline approximation using the cross pair distribution functions of multiple sizes governed by Percus-Yevick approximation [18-20]. The integral equation of the quasicrystalline approximation gives rise to the generalized Lorentz-Lorentz law and the generalized Ewald-Oseen extinction theorem [4,21]. The generalized Lorentz-Lorentz law consists of a homogeneous system of equations. The resulting dispersion relation is an equation governing the effective propagation constant for the coherent wave. The generalized Ewald-Oseen extinction theorem is an inhomogeneous equation that relates the transmitted coherent field to the amplitude, polarization, and direction of propagation of the incident field. The name "generalized" denotes the fact that the classical Lorentz-Lorentz law and the Ewald-Oseen extinction theorem were derived for low frequency effective permittivity for the total field with the imaginary part accounting for absorption loss only. In the present "generalized" case, the effective propagation constant is derived for high frequency when the particle sizes are comparable to wavelength. Also the imaginary part of the effective propagation constant includes attenuation due to scattering diverted to other directions as well as absorption.

The calculations of the cross pair distribution functions are based on a special case of Percus-Yevick approximation that has no inter-particle forces except for non-interpenetration [8,17-19,22]. The Percus-Yevick cross pair distribution functions of multiple sizes have recently been shown to compare very well with Monte-Carlo simulations [23]. The incoherent scattered wave is calculated with



the distorted Born approximation with the result expressed in terms of a product of the T-matrices of particles of different sizes and permittivities and the Fourier transform of the cross pair distribution functions. Numerical examples are chosen to illustrate microwave and millimeter wave scattering from snow cover in the frequency range of 5 GHz to 95 GHz and mean grain radius ranging from 0.03 cm to 0.09 cm [24]. The Rayleigh size distribution and the modified gamma size distribution are used to illustrate the scattering. Salient features of the numerical results for scattering from snow with Rayleigh size distribution are: 1. Correlated dense medium scattering is less than independent scattering at low frequency that is consistent with controlled laboratory experiment [3]. 2. Scattering from dense medium of a Rayleigh size distribution with an average radius can be much larger than the case of monodisperse particles of the sizes identical to that average radius. Particles with larger size can contribute to scattering even though they are fewer in number. 3. The scattering attenuation rate increases rapidly with frequency at low frequency regime and begins to level off at high frequency regime. This is to be contrasted with Rayleigh scattering where scattering attenuation just increases rapidly with frequency. 4. The coherent wave scattering attenuation rate can be large at frequencies above 15 GHz based on the Rayleigh size distribution indicating large optical thickness and the importance of multiple scattering in snow at high frequencies. Comparisons are made with extinction measurements of dry snow at 18 GHz, 35 GHz, 60 GHz, and 90 GHz. Good agreement is obtained and the dense media theory is shown to be able to account for the frequency dependence of extinction of dry snow from 18 GHz to 90 GHz.

II. FORMULATION

Consider a plane electromagnetic plane wave impinging in direction $(\pi - \theta_i, \phi_i)$ upon a half space of spherical discrete scatterers of multiple sizes and multiple permittivities (Fig. 1). Let s_j be the species index $j = 1, 2, \dots, L$. Each species is described by the permittivity ϵ_{sj} , radius a_{sj} and number density n_{sj} . The number density n_{sj} is related to the volume fraction of species f_{sj} , $f_{sj} = 4\pi n_{sj} a_{sj}^3 / 3$. The scatterers are embedded in the lower half space (region 1) with background permittivity equal to ϵ which is the same permittivity as that of the region 0 (Fig. 1).

The electric field of the incident wave is given by

$$\bar{E}_i(\bar{r}) = (E_{vi}\hat{\theta}_{id} + E_{hi}\hat{\phi}_i) e^{i\bar{k}_{id}\cdot\bar{r}} \quad (1)$$

where subscripts v and h denote vertical and horizontal polarizations respectively, \bar{k}_{id} denotes the downward propagating incident wave vector and $\hat{\theta}_{id}$ and $\hat{\phi}_i$ are the associated polarization vectors

$$\begin{aligned} \bar{k}_{id} &= k(\sin \theta_i \cos \phi_i \hat{x} + \sin \theta_i \sin \phi_i \hat{y} - \cos \theta_i \hat{z}) \\ &= k_{ix} \hat{x} + k_{iy} \hat{y} - k_{iz} \hat{z} \end{aligned} \quad (2)$$

$$\hat{\theta}_{id} = -\hat{x} \cos \theta_i \cos \phi_i - \hat{y} \cos \theta_i \sin \phi_i - \hat{z} \sin \theta_i \quad (3)$$

$$\hat{\phi}_i = -\hat{x} \sin \phi_i + \hat{y} \cos \phi_i \quad (4)$$

In the following, our notation follows that of [6], pp. 446-454 and pp. 506-517. Under the quasicrystalline approximation for multiple species, the coherent field obeys the equation

$$\begin{aligned} \overline{w}^{(s_l)}(\bar{r}_l) = & \sum_{s_j=1}^L n_{s_j} \int_{V_{jl}} d\bar{r}_j g_{s_j s_l}(\bar{r}_j - \bar{r}_l) \overline{\sigma}(k\bar{r}_l \bar{r}_j) \overline{T}^{(s_j)} \overline{w}^{(s_j)}(\bar{r}_j) \\ & + e^{i\bar{k}_{id} \cdot \bar{r}_l} \overline{a}_{inc} \end{aligned} \quad (5)$$

where $\overline{w}^{(s_l)}(\bar{r}_l)$ is the conditional average of the exciting field of particles at \bar{r}_l of species s_l conditioning on the particle at \bar{r}_l , $\overline{T}^{(s_j)}$ is the matrix representation of the T matrix of species s_j and $\overline{\sigma}(k\bar{r}_l \bar{r}_j)$ is a transformation matrix transforming from vector spherical waves with center at \bar{r}_j to vector spherical waves with center at \bar{r}_l as given on p. 452 of [6]. It is an exact wave transformation applicable to near field, intermediate field, and far field regions. The function $g_{s_j s_l}(\bar{r}_j - \bar{r}_l)$ is the cross pair distribution function of two species s_j and s_l . These can be computed readily from the Percus-Yevick approximation. These were originally derived for molecular dynamics of fluid mixtures. The result that we use is the special case when intermolecular forces are zero, and molecules cannot interpenetrate each other. In (5) the volume of integration V_{jl} for $d\bar{r}_j$ is the lower half space excluding a "hole" of radius $(a_{s_j} + a_{s_l})$ around vector \bar{r}_l . This is because

$$g_{s_j s_l}(\bar{r}_j - \bar{r}_l) = 0, \quad \text{for } |\bar{r}_j - \bar{r}_l| < a_{s_j} + a_{s_l} \quad (6)$$

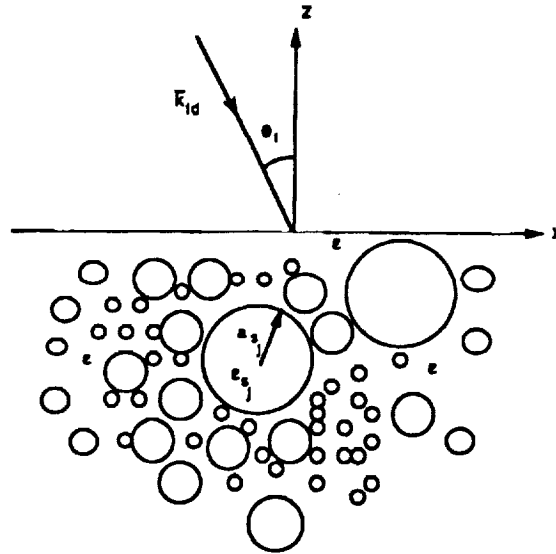


Figure 1. Geometry of the problem: an incident electromagnetic plane wave impinging upon a dense medium consisting of spherical particles with a size distribution.

In (5) \bar{a}_{inc} is the column matrix representing the coefficients of the incident wave when expanded into spherical waves, as given on pp. 507 and 514 of [6].

To solve (5), we assume the solution

$$\bar{w}^{(s_l)}(\bar{r}_l) = \bar{a}_E^{(s_l)} e^{i\bar{K}_d \cdot \bar{r}_l} \quad (7)$$

where $\bar{a}_E^{(s_l)}$ is a column matrix representing coefficients of the exciting field and \bar{K}_d is the downward going effective wave vector

$$\bar{K}_d = K_x \hat{x} + K_y \hat{y} - K_z \hat{z} \quad (8)$$

and the effective wavenumber is

$$K = \sqrt{K_x^2 + K_y^2 + K_z^2} \quad (9)$$

Substitution of (7) into the integrand of the integral (5), integrations can be performed [4,6]. The integral yields two terms that correspond to two waves with dependencies

$$e^{i\bar{K}_d \cdot \bar{r}_l} \quad (10)$$

and

$$e^{iK_x x_l + iK_y y_l - i(k^2 - K_x^2 - K_y^2)^{1/2} z_l} \quad (11)$$

The first wave given by (10) propagates with \bar{K}_d and is to be balanced with the term $\bar{w}^{s_l}(\bar{r}_l)$ on the left hand side of equation since they both have the same propagation constant. Balancing these two terms give rise to the generalized Lorentz-Lorentz law which can be used to calculate the effective propagation constant K . The second wave of (11) with incident wave wavenumber k in the square root will cancel the second term on the right hand side of (5) which is the incident wave term. This cancellation or extinction is the generalized Ewald-Oseen extinction theorem [6,25]. For the two terms to cancel out, the wave vector of (11) must exactly balance the incident wave vector. This gives rise to the phase matching condition

$$K_x = k_{ix} \quad (12)$$

$$K_y = k_{iy} \quad (13)$$

so that from (8), (9), (10), we obtain Snell's law for the effective propagation constant,

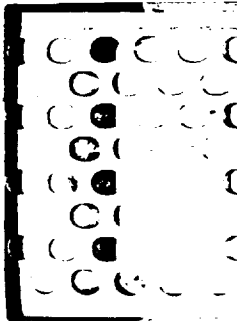
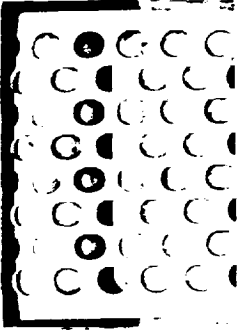
$$K \sin \theta_l = k \sin \theta_i \quad (14)$$

$$K_z = (K^2 - k^2 \sin^2 \theta_i)^{1/2} \quad (15)$$

We call both laws generalized because the concept has been generalized to coherent wave at high frequency while the classical laws were derived for low frequency case.

A. Generalized Lorentz-Lorentz Law

The $\bar{a}_E^{(s_l)}$ column matrix for the exciting field can be expressed in terms of $Y_n^{(s_j)(M)}$ and $Y_n^{(s_j)(N)}$ coefficients where (M) stands for \bar{M} type of vector spherical wave and (N) stands for \bar{N} type of vector spherical wave and n is the



multipole index. The $Y_n^{(s_j)(M)}$ and $Y_n^{(s_j)(N)}$ coefficients satisfy a homogeneous set of equations. By setting the determinant equal to zero, one gets a nonlinear algebraic equation for the effective propagation K . Because the medium is statistical isotropic, we have the same homogeneous set of equation for arbitrary polarization and incident angle of the incident wave. The homogeneous set of equations is

$$Y_\nu^{(s_j)(M)} = -2\pi \sum_{s_l=1}^L n_{s_l} \sum_{n,p} (2n+1) S_p(k, K | R_{s_j s_l}) \left\{ a(1, n | -1, \nu | p) A(n, \nu, p) T_n^{(s_l)(M)} Y_n^{(M)(s_l)} + a(1, n | -1, \nu | p, p-1) B(n, \nu, p) T_n^{(s_l)(N)} Y_n^{(N)(s_l)} \right\} \quad (16)$$

$$Y_\nu^{(s_j)(N)} = -2\pi \sum_{s_l=1}^L n_{s_l} \sum_{n,p} (2n+1) S_p(k, K | R_{s_j s_l}) \times \left\{ a(1, n | -1, \nu | p, p-1) B(n, \nu, p) T_n^{(s_l)(M)} Y_n^{(s_l)(M)} + a(1, n | -1, \nu | p) A(n, \nu, p) T_n^{(s_l)(N)} Y_n^{(s_l)(N)} \right\} \quad (17)$$

where $a(1, n | -1, \nu | p)$ and $a(1, n | -1, \nu | p, p-1)$ are in terms of Wigner 3-j symbols and can be found on pp. 449-450 of [6]. In (16), (17)

$$A(n, \nu, p) = \frac{\nu(\nu+1) + n(n+1) - p(p+1)}{n(n+1)} \quad (18)$$

$$B(n, \nu, p) = \frac{\sqrt{(n+\nu+p+1)(\nu+p-n)(n+p-\nu)(n+\nu-p+1)}}{n(n+1)} \quad (19)$$

$$S_p(k, K | R_{s_j s_l}) = -\frac{R_{s_j s_l}^2}{K^2 - k^2} \left[kh_p'(kR_{s_j s_l}) j_p(KR_{s_j s_l}) - Kh_p(kR_{s_j s_l}) j_p'(KR_{s_j s_l}) \right] + \int_{R_{s_j s_l}}^{\infty} dr r^2 [g_{s_j s_l}(r) - 1] h_p(kr) j_p(Kr) \quad (20)$$

$$R_{s_j s_l} = a_{s_j} + a_{s_l} \quad (21)$$

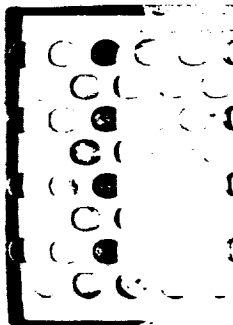
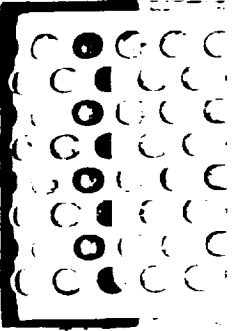
and

$$T_n^{(s_l)(M)} = -\frac{[\rho_{s_l} j_n(\rho_{s_l})]' j_n(\zeta_{s_l}) - [\zeta_{s_l} j_n(\zeta_{s_l})]' j_n(\rho_{s_l})}{[\rho_{s_l} h_n(\rho_{s_l})]' j_n(\zeta_{s_l}) - [\zeta_{s_l} j_n(\zeta_{s_l})]' h_n(\rho_{s_l})} \quad (22)$$

$$T_n^{(s_l)(N)} = -\frac{[\rho_{s_l} j_n(\rho_{s_l})]' \zeta_{s_l}^2 j_n(\zeta_{s_l}) - [\zeta_{s_l} j_n(\zeta_{s_l})]' \rho_{s_l}^2 j_n(\rho_{s_l})}{[\rho_{s_l} h_n(\rho_{s_l})]' \zeta_{s_l}^2 j_n(\zeta_{s_l}) - [\zeta_{s_l} j_n(\zeta_{s_l})]' \rho_{s_l}^2 h_n(\rho_{s_l})} \quad (23)$$

with $\rho_{s_l} = ka_{s_l}$, $\zeta_{s_l} = k_{s_l} a_{s_l}$, and $k_{s_l} = \omega \sqrt{\mu \epsilon_{s_l}}$, are the Mie scattering T matrix coefficients for \bar{M} and \bar{N} vector spherical waves.

For each species s_l , we terminate at a multipole N_{s_l} depending on the radius a_{s_l} of that species. Thus (12) and (13) form N_e homogeneous equations for



the N_e unknowns $Y_n^{(s_l)(M)}$ and $Y_n^{(s_l)(N)}$, $n = 1, 2, \dots, N_{s_l}$ and $s_l = 1, 2, \dots, L$. Thus $N_e = \sum_{l=1}^L 2N_{s_l}$.

The generalized Lorentz-Lorentz law determines the effective propagation K . Setting the determinant of (16)–(17) equal to zero gives the nonlinear equation for the effective propagation constant K . After K is calculated, then the complex transmitted angle θ_t and K_z can be determined from (12)–(15).

The N_e coefficients $Y_n^{(s_l)(M)}$ and $Y_n^{(s_l)(N)}$ are then reduced to only one arbitrary constant that is to be determined by the incident wave. That one equation to determine the arbitrary constant is provided by the generalized Ewald-Oseen extinction theorem which gives a single inhomogeneous equation.

B. Generalized Ewald-Oseen Extinction Theorem

The generalized Ewald-Oseen extinction theorem is obtained by balancing the incident wave term of the second term of (5) and the term of (11) that is a result of the integral in (5). The result matrix equation can be reduced to one single equation for the set of coefficients $Y_n^{(s_l)(M)}$ and $Y_n^{(s_l)(N)}$. The equation depends on whether the incident wave is vertically polarized or horizontally polarized.

1. Vertical polarized incidence

In this case $E_{vi} \neq 0$ and $E_{hi} = 0$. The coherent transmitted wave is also vertically polarized. The generalized Ewald-Oseen extinction theorem gives rise to the following inhomogeneous equation

$$\begin{aligned} & \sum_{s_l=1}^L \sum_n n_{s_l} i \frac{(2n+1)}{n(n+1)} \left[-T_n^{(s_l)(M)} Y_n^{(s_l)(M)(V)} \frac{P_n^1(\cos(\theta_i - \theta_t))}{|\sin(\theta_i - \theta_t)|} \right. \\ & \left. + Y_n^{(s_l)(N)(V)} T_n^{(s_l)(N)} \left\{ \cos(\theta_i - \theta_t) \frac{P_n^1(\cos(\theta_i - \theta_t))}{|\sin(\theta_i - \theta_t)|} + n(n+1) P_n(\cos(\theta_i - \theta_t)) \right\} \right] \\ & = -\frac{(K_z - k_{iz}) k_{iz} k}{2\pi} E_{vi} \end{aligned} \quad (24)$$

where the additional superscript (V) denotes the vertically polarized case. Note that the set of coefficients $Y_n^{(s_l)(M)(V)}$ and $Y_n^{(s_l)(N)(V)}$, $n = 1, \dots, N_{s_l}$, $s_l = 1, \dots, L$ have been determined to within one arbitrary constant by the generalized Lorentz-Lorentz law of (16) and (17). Thus (24) provide the last equation that determines all those coefficients uniquely.

2. Horizontal polarized incidence

For this case $E_{vi} = 0$ and $E_{hi} \neq 0$. The coherent transmitted wave is horizontally polarized. The inhomogeneous equation for the generalized Ewald-Oseen extinction theorem is

$$\sum_{s_l=1}^L \sum_n n_{s_l} i \frac{(2n+1)}{n(n+1)} \left[T_n^{(s_l)(M)} Y_n^{(s_l)(M)(H)} \right]$$

$$\begin{aligned}
& \times \left\{ \cos(\theta_i - \theta_t) \frac{P_n^1(\cos(\theta_i - \theta_t))}{|\sin(\theta_i - \theta_t)|} + n(n+1)P_n(\cos(\theta_i - \theta_t)) \right\} \\
& + T_n^{(s_i)(N)} Y_n^{(s_i)(N)(H)} \left(-\frac{P_n^1(\cos(\theta_i - \theta_t))}{|\sin(\theta_i - \theta_t)|} \right) \\
& = -\frac{(K_z - k_{iz})k_{iz}k}{2\pi} E_{hi} \quad (25)
\end{aligned}$$

where the additional superscript (H) denotes horizontal polarization. Thus the homogeneous system of equations of (16), (17) combined with the inhomogeneous equation (25) determines the coefficients $Y_n^{(s_i)(M)(H)}$ and $Y_n^{(s_i)(N)(H)}$ uniquely for the use of horizontally polarized incidence.

The case of an incident wave of arbitrary polarization can be calculated by linearly combining the cases of vertical and horizontal polarized incidence.

C. Bistatic Scattering Coefficients for Incoherent Field

The incoherent field can be studied with the distorted Born approximation or the first order smoothing approximation [4,6]. From the incoherent field, the bistatic-scattering coefficients for the incoherent field can be calculated. The bistatic scattering coefficients are defined by [6]

$$\gamma_{\beta\alpha}(\theta_s, \phi_s; \theta_i, \phi_i) = \frac{4\pi r^2 |\bar{\mathcal{E}}_\beta^s|^2}{|E_\alpha^i|^2 A_0 \cos \theta_i} \quad (26)$$

where $\bar{\mathcal{E}}_\beta^s$ is the incoherent scattered field of polarization β , E_α^i is the incident field of polarization α , A_0 is the area of target and r is the distance of observation point from target. In the following, we shall give the result for bistatic scattering in the plane of incidence $\phi_s = \phi_i + \pi$ and $0 \leq \theta_s \leq \pi/2$. Because of statistical isotropy of random distribution of spherical scatterers, bistatic scattering in the plane of incidence do not have depolarization for vertically polarized incidence or horizontally polarized incidence. Under the distorted Born approximation, γ_{vv} and γ_{hh} are given as follows; for $0 \leq \theta_s \leq \pi/2$

$$\begin{aligned}
\gamma_{vv}(\theta_s, \phi_s = \pi + \phi_i; \theta_i, \phi_i) &= \frac{4\pi}{k^2} \sum_{s_j} \frac{n_{s_j}}{2K_z'' \cos \theta_i} \left| W_{s_j}^{(V)}(\theta_s, \theta_i) \right|^2 \\
&+ \frac{4\pi}{k^2 \cos \theta_i} \sum_{s_j, s_l} n_{s_j} n_{s_l} U_{s_j, s_l}(\theta_s, \phi_s = \pi + \phi_i; \theta_i, \phi_i) \\
&\times W_{s_j}^{(V)}(\theta_s, \theta_i) W_{s_l}^{(V)*}(\theta_s, \theta_i) F_d \quad (27)
\end{aligned}$$

$$\begin{aligned}
\gamma_{hh}(\theta_s, \phi_s = \pi + \phi_i; \theta_i, \phi_i) &= \frac{4\pi}{k^2} \sum_{s_j} \frac{n_{s_j}}{2K_z'' \cos \theta_i} \left| W_{s_j}^{(H)}(\theta_s, \theta_i) \right|^2 \\
&+ \frac{4\pi}{k^2 \cos \theta_i} \sum_{s_j, s_l} n_{s_j} n_{s_l} U_{s_j, s_l}(\theta_s, \phi_s = \pi + \phi_i; \theta_i, \phi_i) \\
&\times W_{s_j}^{(H)}(\theta_s, \theta_i) W_{s_l}^{(H)*}(\theta_s, \theta_i) F_d \quad (28)
\end{aligned}$$

$$\begin{aligned}
 W_{s_j}^{(V)}(\theta_s, \theta_i) = & \sum_n (-1)^n \frac{(2n+1)}{n(n+1)} \left\{ T_n^{(s_j)(M)} Y_n^{(s_j)(M)(V)} \frac{P_n^1(\cos(\theta_s - \theta_i))}{|\sin(\theta_s - \theta_i)|} \right. \\
 & + T_n^{(s_j)(N)} Y_n^{(s_j)(N)(V)} \left(\cos(\theta_s - \theta_i) \frac{P_n^1(\cos(\theta_s - \theta_i))}{|\sin(\theta_s - \theta_i)|} \right. \\
 & \left. \left. + n(n+1) P_n(\cos(\theta_s - \theta_i)) \right) \right\} \quad (29)
 \end{aligned}$$

$$\begin{aligned}
 W_{s_j}^{(H)}(\theta_s, \theta_i) = & \sum_n (-1)^n \frac{(2n+1)}{n(n+1)} \left\{ T_n^{(s_j)(N)} Y_n^{(s_j)(N)(H)} \frac{P_n^1(\cos(\theta_s - \theta_i))}{|\sin(\theta_s - \theta_i)|} \right. \\
 & + T_n^{(s_j)(M)} Y_n^{(s_j)(M)(H)} \left(\cos(\theta_s - \theta_i) \frac{P_n^1(\cos(\theta_s - \theta_i))}{|\sin(\theta_s - \theta_i)|} \right. \\
 & \left. \left. + n(n+1) P_n(\cos(\theta_s - \theta_i)) \right) \right\} \quad (30)
 \end{aligned}$$

and

$$\begin{aligned}
 U_{s_j s_l}(\theta_s, \phi_s = \pi + \phi_i; \theta_i, \phi_i) &= \frac{1}{2 \operatorname{Im}(K_z)} \int_{-\infty}^{\infty} d\bar{r} [g_{s_j s_l}(\bar{r}) - 1] e^{i(\operatorname{Re} \bar{K}_d - \bar{k}_s) \cdot \bar{r}} \\
 &= \frac{(2\pi)^3}{2 \operatorname{Im}(K_z)} H_{s_j s_l}(\bar{p} = -\operatorname{Re} \bar{K}_d + \bar{k}_s) \quad (31)
 \end{aligned}$$

where superscript double prime denotes imaginary part. In (31), \bar{K}_d is given by (8), (12)–(15) and

$$\bar{k}_s = k(\sin \theta_s \cos \phi_s \hat{x} + \sin \theta_s \sin \phi_s \hat{y} + \cos \theta_s \hat{z}) \quad (32)$$

is the wave vector of the scattered wave in region 0. In (31) $H_{s_j s_l}$, $s_j, s_l = 1, 2, \dots, L$ is the Fourier transform of the cross pair distribution function $g_{s_j s_l}$ minus 1. It is also called structure factor.

$$H_{s_j s_l}(\bar{p}) = \frac{1}{(2\pi)^3} \int_{-\infty}^{\infty} d\bar{r} [g_{s_j s_l}(\bar{r}) - 1] e^{-i\bar{p} \cdot \bar{r}} \quad (33)$$

Thus the bistatic scattering coefficient is proportional to the Fourier transform of the cross pair distribution function, a concept that has been used extensively in the investigation of molecular structures of liquids and amorphous solids by X-rays [22].

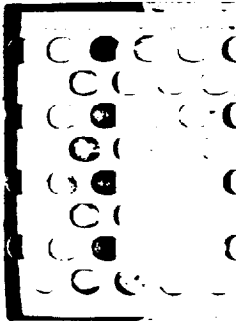
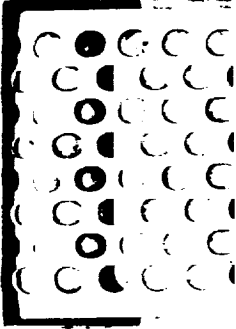
For multiple sizes of spherical particles, the cross pair distribution function $g_{s_j s_l}$ are isotropic, so that $g_{s_j s_l}(\bar{r})$ depends on $|\bar{r}|$ only. Hence, the cross structure factor $H_{s_j s_l}(\bar{p})$ also depends on $|\bar{p}|$ only. It is useful to note that under the Percus-Yevick approximation, closed form expressions are available [18,19,22] for $H_{s_j s_l}(\bar{p})$, $s_j, s_l = 1, 2, \dots, L$.

In (27) and (28)

$$F_d = (1 - e^{-2K_z'' d}) \quad (34)$$

where $K_z'' = \operatorname{Im}(K_z)$.

We have inserted in (34) the thickness d of the layer containing random discrete scatterers. The results of (34) only include volume scattering and ignores any possible reflections from the bottom boundary.



III. NUMERICAL RESULTS AND DISCUSSION

In this section, we shall illustrate the numerical results of the effective propagation constants and backscattering coefficients using parameters of snow. The results are illustrated with the Rayleigh size distribution which is a special case of the modified gamma size distribution. The size distribution is represented by $n(a)$, which is the number of particles per unit volume with radii between a and $a + da$. It is given by

$$n(a) = \frac{\pi f a}{16 \langle a \rangle^3} \exp\left(-\frac{\pi a^2}{4 \langle a \rangle^2}\right) \quad (35)$$

where $\langle a \rangle$ is the mean radius. The fractional volume and the mean radius are defined by

$$f = \int_0^\infty da \frac{4\pi}{3} a^3 n(a) \quad (36)$$

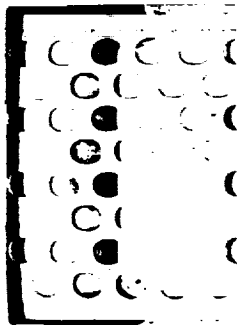
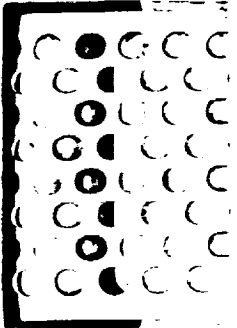
$$\langle a \rangle = \frac{\int_0^\infty da a n(a)}{\int_0^\infty da n(a)} \quad (37)$$

$$a_m = \sqrt{\frac{2}{\pi}} \langle a \rangle \quad (38)$$

Thus, given the fractional volume f , the Rayleigh size distribution contains only one parameter, viz., the mean radius. In (38) a_m is the mode radius where the size distribution is at a maximum [20], and as indicated in (38), is approximately equal to $0.798 \langle a \rangle$. In our numerical calculations of Figs. 2 to 11, we discretize the Rayleigh size distribution into 20 different equally spaced sizes (i.e. $L = 20$ species). The pair distribution functions for a medium with 20 sizes are then calculated by the Percus-Yevick approximation [20]. The maximum size for these 20 sizes is chosen such that at least 99.7% of the scattering contributions and the fractional volume of particles are included. That usually occurs around 2.5 to 3 times the mean radius. Comparison will be made between the scattering of a medium with Rayleigh size distribution of a specified value of $\langle a \rangle$ and the case of monodisperse particles with radii equal to that same value. The results of QCA will also be compared with that of independent scattering. For the case of independent scattering, the extinction rate is

$$(\kappa_e)_{\text{independent}} = -\frac{2\pi}{k^2} \sum_{s_j=1}^L n_{s_j} \sum_n (2n+1) \text{Re} \left[T_n^{(M)s_j} + T_n^{(N)s_j} \right] \quad (39)$$

In Figs. 2 and 3, we plot respectively the effective loss tangent $2K_i/K_r$ and the normalized phase velocity k/K_r as a function of fractional volume at frequency = 37 GHz for two Rayleigh size distributions with $\langle a \rangle = 0.05$ cm and $\langle a \rangle = 0.09$ cm. We note that the effective loss tangents first increase with fractional volume, rise to maxima and then decrease with further increase in fractional volume. These are consistent with controlled optical experiments [3] and controlled microwave experiments [26]. The peak of the larger size of $\langle a \rangle = 0.09$ cm occurs at $f = 0.19$ and the peak for $\langle a \rangle = 0.05$ cm occurs at $f = 0.16$. This indicates that scattering



by larger particles are "more independent." "More independent" means that for scattering by large particles, the "hole correction" for distribution functions very often are sufficient to characterize the scattering [6]. Figure 3 shows that the phase velocity decreases with fractional volume with smaller velocity for larger particles indicating that scattering decreases phase velocity. In Fig. 4, the backscattering coefficients are plotted as a function of fractional volume for a layer thickness of $d = 3$ cm. The backscattering coefficients are $\sigma_{\beta\beta} = \cos\theta; \gamma_{\beta\beta}$ with $\beta = v, h$. A small thickness is chosen because the model of incoherent scattering is limited to distorted Born approximation which is valid only for small optical thickness. The associated extinction rates of Fig. 2 show that multiple scattering of incoherent waves become important for thickness larger than 3 cm as the optical thickness becomes large. The results of Fig. 4 indicate that backscattering coefficient can be as large as -4 dB for a small layer thickness of $d = 3$ cm.

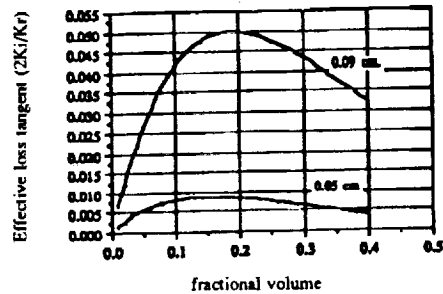
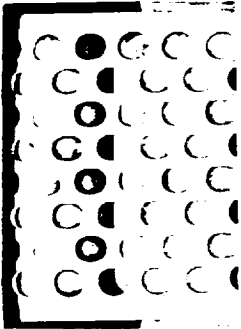


Figure 2. Effective loss tangent $2K_i/K_r$ of QCA as a function of fractional volume. Frequency is at 37 GHz. The permittivity of the particles is $\epsilon_s = (3.2 + i0.001)\epsilon_0$. Two cases of Rayleigh size distributions are considered with $\langle a \rangle = 0.05$ cm and $\langle a \rangle = 0.09$ cm.

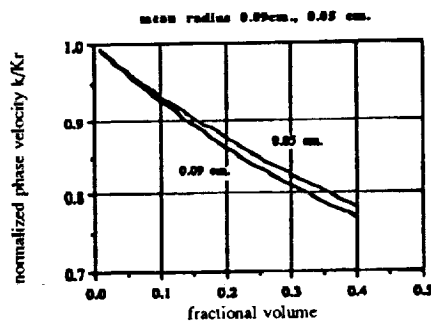
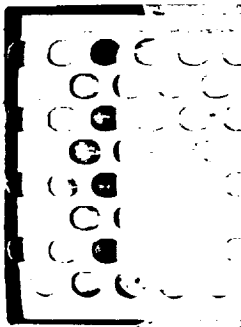


Figure 3. Normalized phase velocity k/K_r of QCA as a function of fractional volume. Frequency is at 37 GHz. The permittivity of the particles is $\epsilon_s = (3.2 + i0.001)\epsilon_0$. Two cases of Rayleigh size distributions are considered with $\langle a \rangle = 0.05$ cm and $\langle a \rangle = 0.09$ cm.



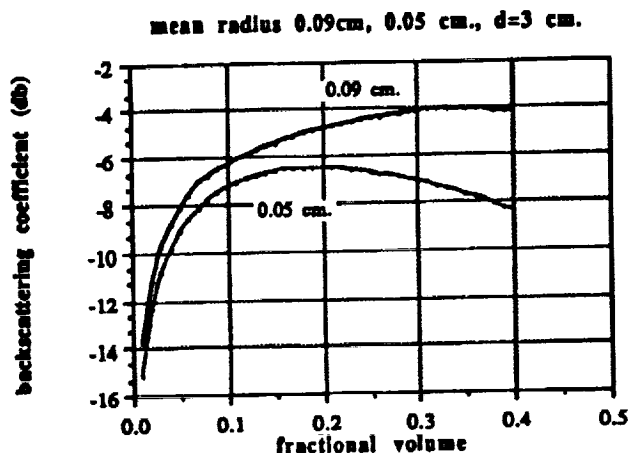
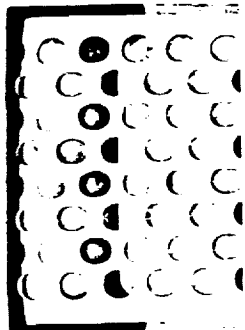
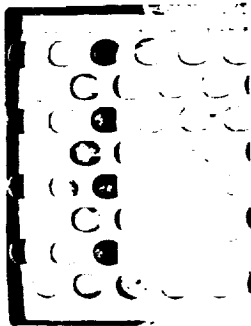


Figure 4. Backscattering coefficient σ_{hh} in dB of QCA as a function of fractional volume. Frequency is at 37 GHz. The permittivity of the particles is $\epsilon_s = (3.2 + i0.001)\epsilon_0$. Two cases of Rayleigh size distributions are considered with $\langle a \rangle = 0.05$ cm and $\langle a \rangle = 0.09$ cm. The layer thickness is $d = 3$ cm and incident angle is 30° .

In Figs. 5, 6, and 7, we show the coherent wave attenuation rates for a smaller mean grain radius of 0.035 cm. The corresponding mode radius is 0.0279 cm. Figure 5 compares the extinction rate $2K_i$ between independent scattering and QCA. We note that attenuation rate of independent scattering is larger than QCA. The results show that the extinction rate first increases rapidly with frequency as in Rayleigh scattering. Then it departs from Rayleigh scattering around 20 GHz and starts to gradually level off. This indicates the importance of including Mie scattering effects beyond 20 GHz for $\langle a \rangle = 0.035$ cm. Figure 6 compares the results of QCA between the extinction rates of monodisperse particles with radii = 0.035 cm and the case of Rayleigh size distribution with $\langle a \rangle = 0.035$ cm. We note that the case of Rayleigh size distribution has a considerably larger scattering rate than monodisperse case. This indicates the importance of including size distribution in modelling scattering from realistic geophysical terrain when grain sizes are small. It also means that in laboratory controlled experiments when particle sizes are made to be close to monodisperse, the measured scattering can be substantially less. The numerical results indicate that the extinction rate is at 1.056 cm^{-1} based on Rayleigh size distribution at frequency = 95 GHz meaning that there is strong multiple scattering of incoherent waves at such high frequency even for moderate snow layer thicknesses. Figure 7 shows the results of HH backscattering coefficient for a layer thickness of $d = 10$ cm. It shows that distorted Born backscattering can be as large as 0 dB at 60 GHz with $\langle a \rangle = 0.035$ cm. The curves show saturation effects due to the limitations of distorted Born approximation. We expect that if multiple scattering of incoherent waves are included, the backscattering should continue to increase above 0 dB.



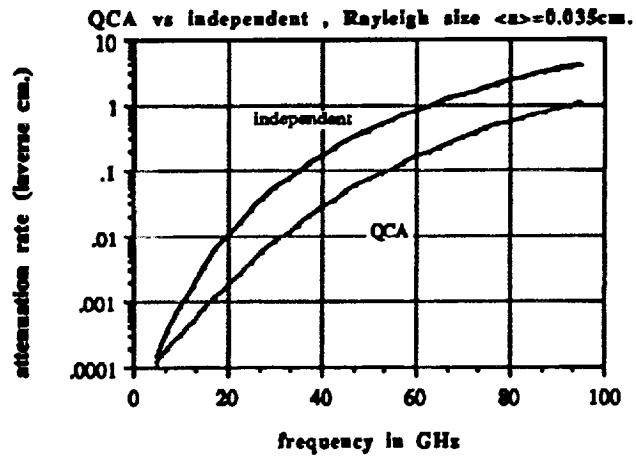
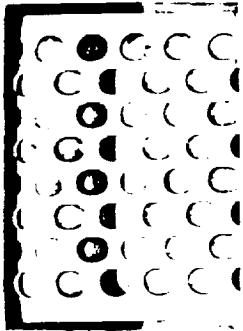


Figure 5. Coherent wave attenuation rate $2K_i$ in cm^{-1} as a function of frequency. The permittivity of the particles is $\epsilon_s = (3.2 + i0.001)\epsilon_0$. Rayleigh size distribution is considered with $\langle a \rangle = 0.035 \text{ cm}$ and fractional volume $f = 0.3$. The cases of independent scattering and QCA are compared.

QCA (single size $a=0.035 \text{ cm}$. vs Rayleigh size $\langle a \rangle = 0.035 \text{ cm}$.)

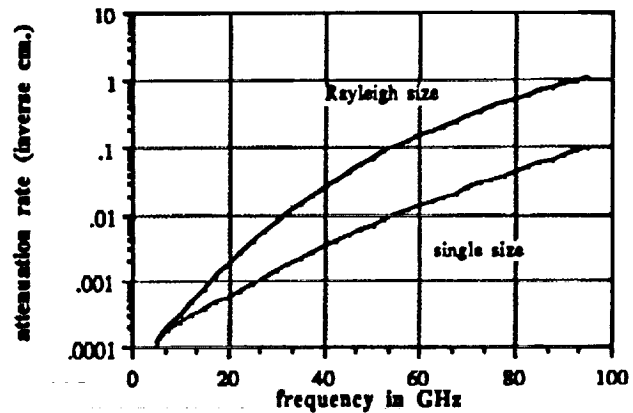
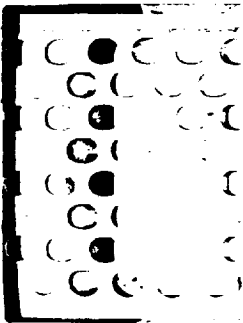
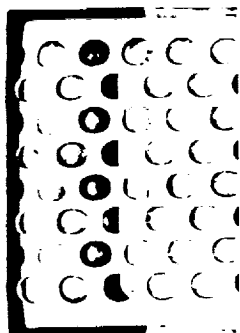


Figure 6. Coherent wave attenuation rate $2K_i$ in cm^{-1} under QCA as a function of frequency. The permittivity of the particles is $\epsilon_s = (3.2 + i0.001)\epsilon_0$. The fractional volume is $f = 0.3$. The cases of identical sizes of $a = 0.035 \text{ cm}$ and Rayleigh size distribution with $\langle a \rangle = 0.035 \text{ cm}$ are compared.





QCA ($d=10$ cm., single size $a=0.035$ cm. vs Raleigh size $\langle a \rangle=0.035$ cm.)

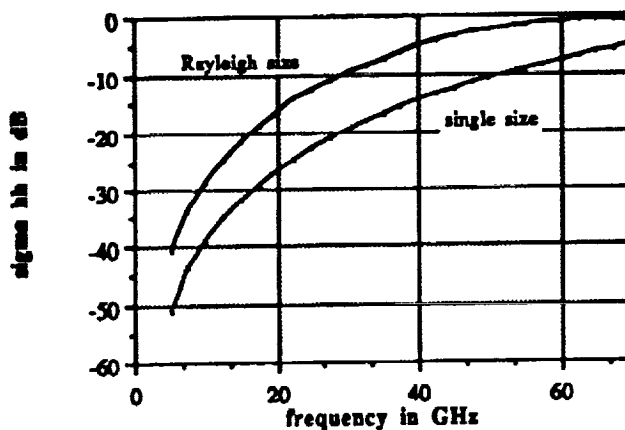
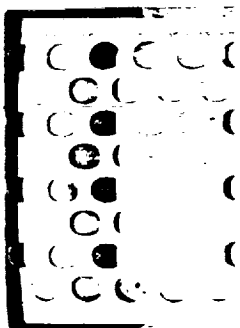
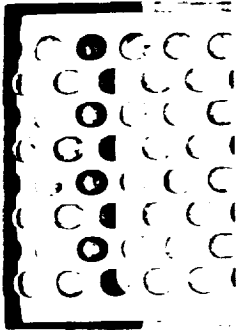


Figure 7. Backscattering coefficient σ_{hh} in dB of QCA as a function of frequency. The permittivity of the particles is $\epsilon_p = (3.2 + i0.001)\epsilon_0$. The layer thickness is $d = 10$ cm and incident angle is 30° . The cases of identical sizes of $a = 0.035$ cm and Rayleigh size distribution with $\langle a \rangle = 0.035$ cm are compared.

In Figs. 8, 9 and 10, the results for the cases of a larger mean grain radius of 0.075 cm are shown. The corresponding mode radius is 0.0598 cm. Figure 8 shows that the extinction rate of independent scattering is still larger than that of QCA. However the two curves are much closer than that of Figure 5 showing that scattering by larger particles are "more independent." At frequency = 95 GHz, QCA and independent scattering are almost the same. Figure 9 shows that the Rayleigh size distribution case is considerably larger than the monodisperse case. Strong multiple scattering is to be expected as the extinction rates of QCA for Rayleigh size case are large. Figure 10 show the HH backscattering coefficients of a snow layer of thickness $d = 1$ cm. The small layer thickness is chosen to satisfy the validity condition of small optical thickness for distorted Born approximation. The saturation effect in Fig. 10 is a demonstration of the limitation of the distorted Born approximation. Nevertheless, the backscattering coefficients are quite large in view of the small layer thickness of $d = 1$ cm. In Fig. 11, the VV and HH backscattering coefficients are plotted as a function of incident angles at frequency = 37 GHz and $d = 10$ cm. There is a gradual decrease with incident angle. There is little difference between VV and HH with the HH return slightly larger than VV.





QCA vs independent, Rayleigh size $\langle a \rangle = 0.075$ cm.

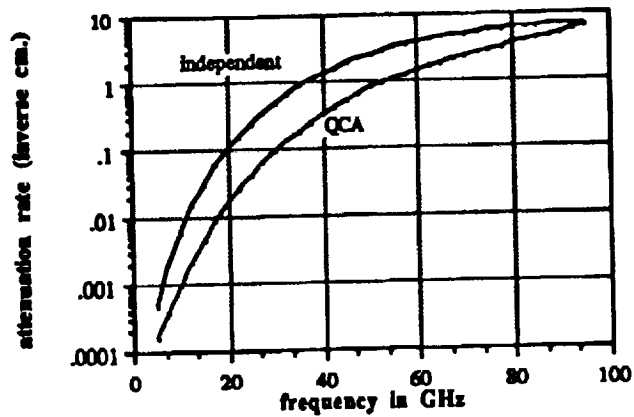


Figure 8. Coherent wave attenuation rate $2K_i$ in cm^{-1} as a function of frequency. The permittivity of the particles is $\epsilon_s = (3.2 + i0.001)\epsilon_0$. Rayleigh size distribution is considered with $\langle a \rangle = 0.075$ cm and fractional volume $f = 0.3$. The cases of independent scattering and QCA are compared.

qca (single size $a=0.075$ cm., and Rayleigh size $\langle a \rangle = 0.075$ cm.)

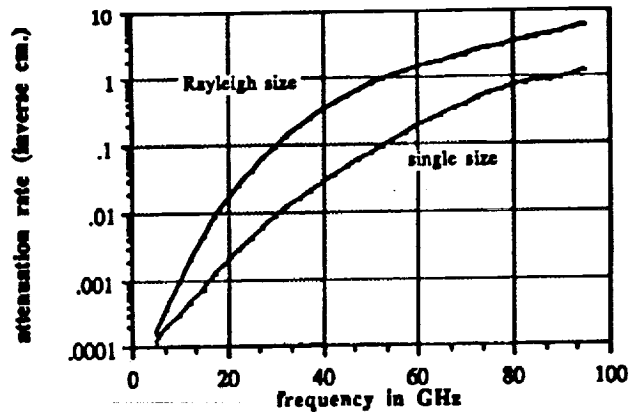
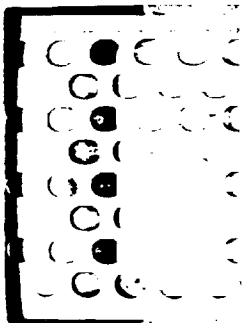


Figure 9. Coherent wave attenuation rate $2K_i$ in cm^{-1} of QCA as a function of frequency. The permittivity of the particles is $\epsilon_s = (3.2 + i0.001)\epsilon_0$. The fractional volume is $f = 0.3$. The cases of identical sizes of $a = 0.075$ cm and Rayleigh size distribution with $\langle a \rangle = 0.075$ cm are compared.



QCA ($d = 1$ cm.; single size $a=0.075$ cm.; Rayleigh size $\langle a \rangle=0.075$ cm.)

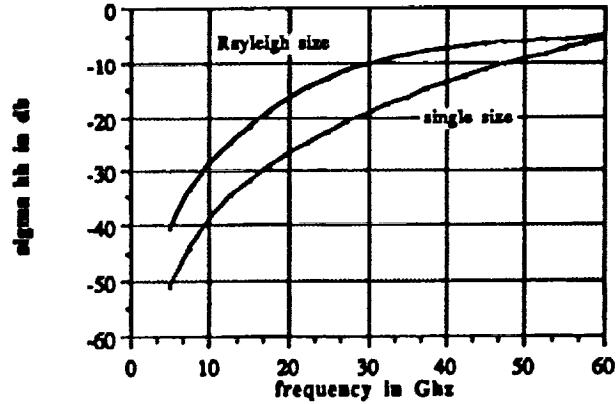
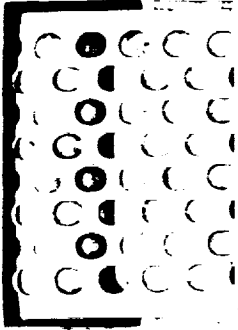


Figure 10. Backscattering coefficient σ_{hh} in dB of QCA as a function of frequency. The permittivity of the particles is $\epsilon_s = (3.2 + i0.001)\epsilon_0$. The layer thickness is $d = 1$ cm and incident angle is 30° . The cases of identical sizes of $a = 0.075$ cm and Rayleigh size distribution with $\langle a \rangle = 0.075$ cm are compared.

VV and HH returns, $d=10$ cm., Rayleigh size $\langle a \rangle=0.075$ cm.

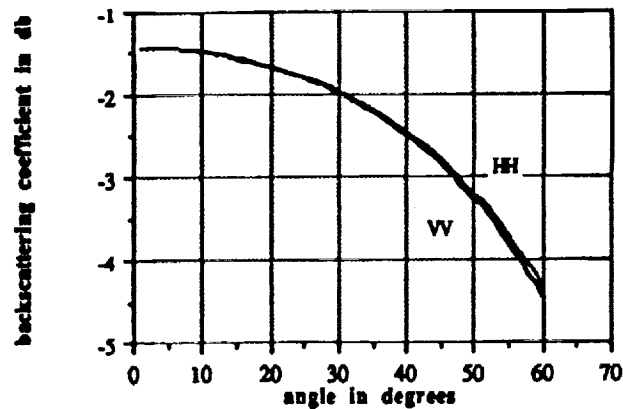
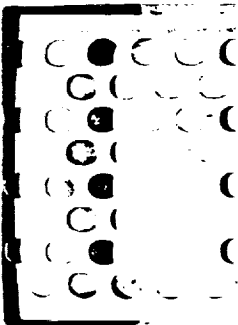


Figure 11. Backscattering coefficient σ_{vv} and σ_{hh} in dB of QCA as a function of incident angle. The permittivity of the particles is $\epsilon_s = (3.2 + i0.001)\epsilon_0$. The layer thickness is $d = 10$ cm. Frequency is at 37 GHz. The cases of Rayleigh size distribution with $\langle a \rangle = 0.075$ cm is considered.



IV. COMPARISON WITH EXTINCTION MEASUREMENTS OF DRY SNOW BETWEEN 18 GHZ AND 90 GHZ

In this section, we apply the dense media QCA-PY-Mie theory to compare with extinction measurements of dry snow. Dry snow is a mixture of ice grains and air. Hallikanen et al. [24] measured the extinction behavior of different types of dry snow at four frequencies: 18 GHz, 35 GHz, 60 GHz and 90 GHz. Thus, it is important to match the data for a sample over the entire frequency range with one set of physical parameters. In this section, we shall match the data of one sample (sample number 9 [24]) of large grains. Other samples are being studied and comparisons will be reported in the future.

Recently, grain size distributions of dry snow have been measured extensively [27]. Dry snow can be divided into new snow and old snow. New snow has smaller mean size and smaller standard deviation while old snow has larger grain size and larger standard deviation. The standard deviation of grain size radius can be several times larger than the mode radius showing that snow has a broad grain size distribution. The maximum grain diameter is between 3mm to 4 mm. It is also observed that the number ratio of large grains to grains with mean size is about 1 to 300 [27].

In the following, we shall compare with the snow data for sample 9 [24] with ground truth of mean grain diameter = 1 mm and snow density = 0.385 gm/cc. This corresponds to a fractional volume of 0.423. The reported measurements of extinction are 10.2 dB/m, 58.8 dB/m, 247.2 dB/m and 304.0 dB/m respectively at frequencies of 18 GHz, 35 GHz, 60 GHz and 90 GHz. Comparisons are made with QCA-PY-Mie theory based on two size distributions: the modified gamma size distribution and the histogram (Fig. 12) based on information as discussed above [27]

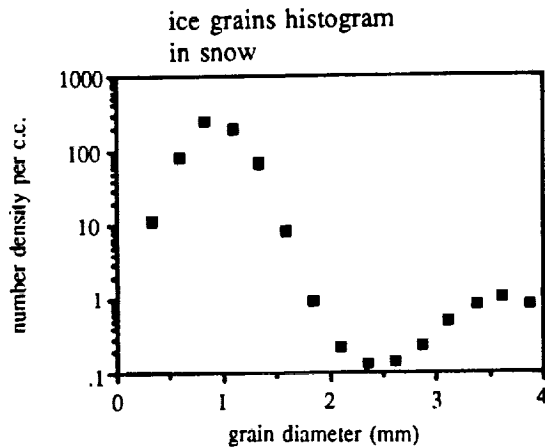
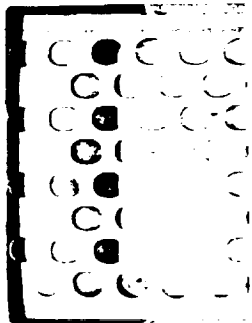
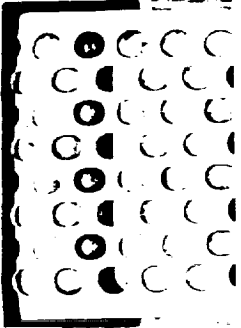


Figure 12. The ice grain size histogram in snow in number per c.c. as a function of grain diameter. The histogram is used for QCA-PY-Mie theory in Fig. 14. There are 15 sizes, with mean grain radius of 0.0479 cm and fractional volume of 0.4134.



The modified gamma size distribution is

$$n(a) = K_1 a^P \exp(-K_2 a^Q) \quad (39)$$

with

$$K_2 = \left(\frac{\Gamma\left(\frac{P+2}{Q}\right)}{\langle a \rangle \Gamma\left(\frac{P+1}{Q}\right)} \right)^Q \quad (40)$$

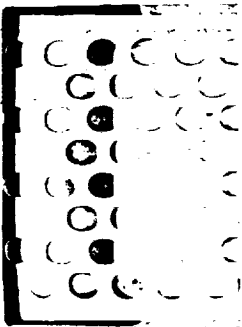
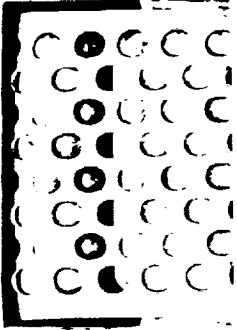
$$K_1 = \frac{3fQ}{4\pi\Gamma\left(\frac{P+4}{Q}\right)} (K_2)^{\frac{P+4}{Q}} \quad (41)$$

Thus, the size distributions have four parameters P , Q , K_1 , and K_2 . However, K_2 and K_1 can be expressed in terms of mean radius $\langle a \rangle$ and fractional volume f as indicated in (40)-(41). Thus the alternative four parameters are $\langle a \rangle$, f , P and Q .

The second size distribution that we used is in Fig. 12 which shows the histogram number density (number per c.c.) for 15 sizes with mean grain radius of 0.0479 cm and fractional volume of 0.4134. Note that there are large grains between 3 mm to 4 mm with the number ratio to grains of mean size of about 1 to 300 [27].

In Fig. 13, we make a comparison with the data based on the modified gamma size distribution with $P = 1$, $Q = 1.4$, $\langle a \rangle = 0.05$ cm. and $f = 0.423$. The permittivity of ice grains chosen are $\epsilon_s = 3.2\epsilon_0 + ic_s''$ with $\epsilon_s''/\epsilon_0 = 0.007, 0.009, 0.011$ and 0.014 respectively at 18 GHz, 35 GHz, 60 GHz and 90 GHz which corresponds to a salinity of 0.12 parts per thousand [28]. The results of independent scattering are also shown for comparison. The results in figure 13 show that the independent scattering results are larger than the data while the QCA-PY-Mie theory shows a reasonable match based on the modified gamma size distribution.

In Fig. 14, we make a comparison with data based on the histogram size distribution of Fig. 12 and using the same permittivity of ice grains as in Fig. 13. The agreement is good. It seems that with size distribution, the QCA-PY-Mie theory can explain the frequency dependence of the extinction of dry snow between 18 GHz and 90 GHz. The results of independent scattering are also shown for comparison. Future comparisons will be made when the size distributions of ice grains in snow become available [27]. Note that we have used the Percus-Yevick pair functions for non-interacting particles without mutual force. It seems that ice grains may have sticking force that may affect the pair distribution functions. Besides QCA, the quasicrystalline approximation with coherent potential [6,8] should be used. Monte-Carlo simulations of extinction rate can also be made based on the solution of Maxwell's equations [29].



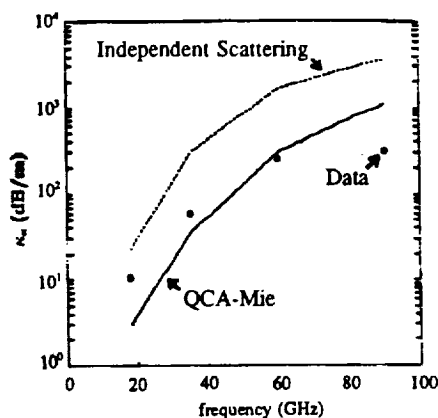
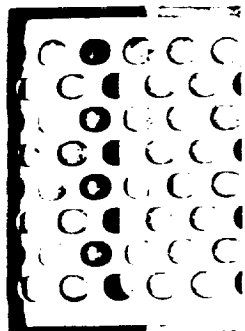


Figure 13. Comparison between QCA-PY-Mie theory and independent scattering with snow extinction data at 18 GHz, 35 GHz, 60 GHz, and 90 GHz of Hallikanen et al. [24] with ground truth of mean grain diameter of 1 mm and snow density=0.385 gm/cc. The theory is based on the modified gamma size distribution with $P = 1$, $Q = 1.4$, $\langle a \rangle = 0.05$ cm, and $f = 0.423$. The permittivity of ice grains chosen are $\epsilon = 3.2\epsilon_0 + i\epsilon_s$ with $\epsilon_s''/\epsilon_0 = 0.007, 0.009, 0.011$ and 0.014 respectively at 18 GHz, 35 GHz, 60 GHz, and 90 GHz which corresponds to a salinity of 0.12 parts per thousand [28].

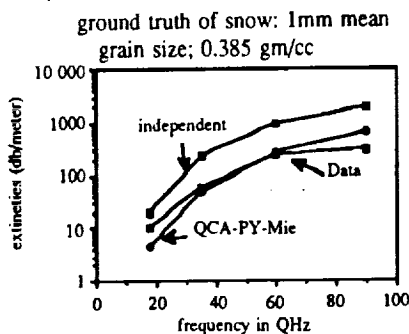
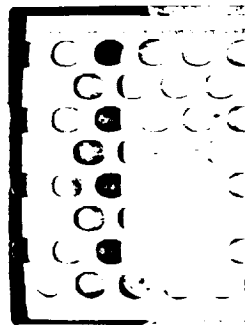


Figure 14. Comparison between QCA-PY-Mie theory and independent scattering with snow extinction data at 18 GHz, 35 GHz, 60 GHz, and 90 GHz of Hallikanen et al. [24] with ground truth of mean grain diameter of 1 mm and snow density=0.385 gm/cc. The theory is based on the histogram of Fig. 12 with $\langle a \rangle = 0.0479$ cm, and $f = 0.4134$. The permittivity of ice grains chosen are $\epsilon_s = 3.2\epsilon_0 + i\epsilon_s''$ with $\epsilon_s''/\epsilon_0 = 0.007, 0.009, 0.011$, and 0.014 , respectively, at 18 GHz, 35 GHz, 60 GHz, and 90 GHz which corresponds to a salinity of 0.12 parts per thousand [28].



V. CONCLUSIONS

In this paper, we have illustrated the importance of dense medium theory of correlated Mie scattering for studying snow cover at microwave and millimeter wave frequencies above 15 GHz. We have also demonstrated the importance of including size distributions as there are large difference between the polydisperse and the monodisperse cases. The importance of polydispersions has long been noted [17], particularly at low frequency when scattering is proportional to particle size to the sixth power. Based on size distributions, the dense medium theory is able to account for the frequency dependence of extinction of dry snow between 18 GHz and 90 GHz. The calculations also show that extinction rates are large for dense medium so that multiple scattering effects become important even for small layer thicknesses. The calculation of the incoherent wave in this paper has been limited to that of distorted Born approximation. The subject of multiple scattering for the incoherent wave including the effects of correlated Mie scattering should be an important future subject for snow cover scattering beyond 15 GHz.

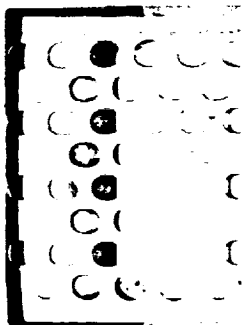
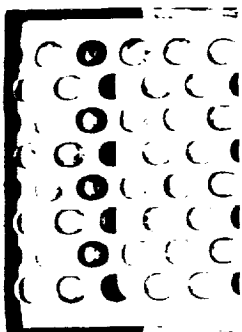
ACKNOWLEDGMENTS

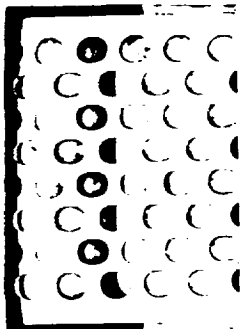
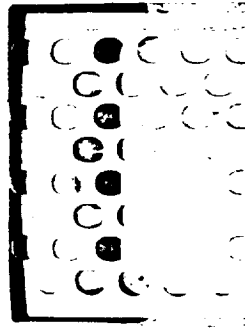
The research in this paper has been supported by the Army Research Office, NASA and the National Science Foundation. The authors would like to thank R. West, D. Winebrenner and J. C. Shi for stimulating discussions.

The Editor thanks A. K. Fung and two anonymous Reviewers for reviewing the paper.

REFERENCES

1. Twersky, V., "Coherent electromagnetic waves in pair-correlated random distributions of aligned scatterers," *J. Math. Phys.*, Vol. 19, 215-230, 1978.
2. Tsang, L., and J. A. Kong, "Effective propagation constant for coherent electromagnetic waves in media embedded with dielectric scatterer," *J. Appl. Phys.*, Vol. 53, 7162-7173, 1982.
3. Ishimaru, A., and Y. Kuga, "Attenuation constant of a coherent field in a dense distribution of particles," *J. Opt. Soc. Am.*, Vol. 72, 1317-1320, 1982.
4. Tsang, L., and J. A. Kong, "Scattering of electromagnetic waves from a half space of densely distributed dielectric scatterers," *Radio Science*, Vol. 18, 1260-1272, 1983.
5. Varadan, V. K., V. N. Bringi, V. V. Varadan, and A. Ishimaru, "Multiple scattering theory for waves in discrete random media and comparison with experiments," *Radio Science*, Vol. 18, 321-327, 1983.
6. Tsang, L., J. A. Kong, and R. T. Shin, *Theory of Microwave Remote Sensing*, Wiley-Interscience, New York, 1985.
7. Tsang, L., and A. Ishimaru, "Radiative wave equation for vector electromagnetic propagation in dense non-tenuous media," *J. Electro. Waves Applic.*, Vol. 1, 59-72, 1987.
8. Ding, K. H., and L. Tsang, "Effective propagation constants in media with densely distributed dielectric particles of multiple sizes and permittivities," Chapter 3 of *Progress in Electromagnetic Research*, Vol. 1, ed. J. A. Kong, 241-295, 1989.
9. Wen, B., L. Tsang, D. P. Winebrenner, and A. Ishimaru, "Dense medium radiative transfer theory: comparison with experiment and application to microwave remote sensing and polarimetry," *IEEE Trans. Geosci. Remote Sensing*, Vol. 28, 46-59,

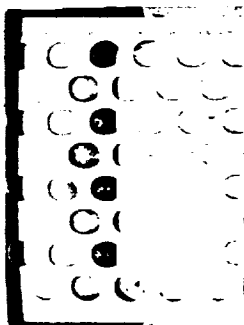
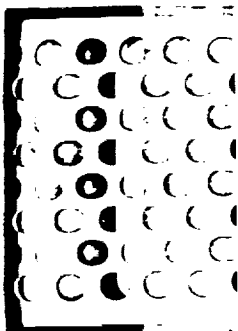


- 
- 
10. Kuga, Y., F. T. Ulaby, T. F. Haddock, and R. DeRoo, "Millimeter wave radar scattering from snow: Part I Radiative transfer model," *Radio Science*, Vol. 26, No. 2, 329-341, 1991.
 11. Ulaby, F. T., T. F. Haddock, R. Austin, and Y. Kuga, "Millimeter wave radar scattering from snow: Part II—comparison of theory with experimental observations," *Radio Science*, Vol. 26, No. 2, 343-351, 1991.
 12. Zhu, P. A., A. K. Fung, and K. W. Wong, "Effective propagation constants in dense discrete random media under effective medium approximation," *Radio Science*, Vol. 22, 234-250, 1987.
 13. Tsang, L., "Dense media radiative transfer theory for dense discrete random media with spherical particles of multiple sizes and permittivities," *Progress in Electromagnetic Research*, in press, 1991.
 14. Ishimaru, A., *Wave Propagation and Scattering in Random Media*, Vol. 2, Academic Press, New York, 1978.
 15. Kuga, Y., and A. Ishimaru, "Retroreflectance from a dense distribution of spherical particles," *J. Opt. Soc. Am. A*, Vol. 1, 831-835, 1984.
 16. West, R., L. Tsang, and D. P. Winebrenner, "Dense medium radiative transfer theory for two scattering layers with a Rayleigh distribution of particle sizes," to be published, 1991.
 17. Deirmendjian, D., *Electromagnetic Scattering on Spherical Polydispersions*, Elsevier, New York, 1969.
 18. Baxter, R. J., "Ornstein-Zernike relation for a disordered fluid," *Australian J. of Physics*, Vol. 21, 563-569, 1968.
 19. Baxter, R. J., "Ornstein-Zernike relation and Percus-Yevick approximation for fluid mixtures," *Journal of Chemical Physics*, Vol. 52, 4559-4562, 1970.
 20. Ding, K. H., and L. Tsang, "Effective propagation constants and attenuation rates in media of densely distributed coated dielectric particles with size distributions," *Journal of Electromagnetic Waves and Applications*, Vol. 5, No. 2, 117-142, 1991.
 21. Born, M., and E. Wolf, *Principles of Optics*, 5th ed., Pergamon Press, New York, 1975.
 22. Waseda, Y., *The Structure of Non-Crystalline Materials, Liquids and Amorphous Solids*, McGraw Hill, New York, 1980.
 23. Ding, K. H., C. E. Mandt, L. Tsang, and J. A. Kong, "Monte Carlo simulations of pair distribution functions with multiple sizes in dense discrete random media," submitted to *Journal of Electromagnetic Waves and Applications*, 1991.
 24. Hallikainen, M. T., F. T. Ulaby, and T. van Deventer, "Extinction coefficient of dry snow at microwave and millimeter wave frequencies," *IEEE Trans. on Geoscience and Remote Sensing*, Vol. 25, 737-745, 1987.
 25. Fikioris, J. G., and P. C. Waterman, "Multiple scattering of waves II, hole-corrections in the scalar case," *J. Math. Phys.*, Vol. 5, 1413-1420, 1964.
 26. Mandt, C., "Microwave propagation and scattering in a dense distribution of spherical particles," M.S. thesis, Department of Electrical Engineering, University of Washington, 1987.
 27. Shi, J. C., private communication, U. C. Santa Barbara.
 28. Matzler, C., and U. Wegmuller, "Dielectric properties of fresh-water ice at microwave frequencies," *J. Phys. D.*, Vol. 20, 1623-1630, 1987.
 29. Tsang, L., C. Mandt, and K. H. Ding, "Monte-Carlo simulations of extinction rate of dense media based on solution of Maxwell's equations," to be published, 1991.

Leung Tsang is Professor of Electrical Engineering at the University of Washington, Seattle, Washington. He received all his degrees (B.S., M.S., and Ph.D.) from the Department of Electrical Engineering and Computer Science of the Massachusetts Institute of Technology, Cambridge, Massachusetts. He is the coauthor of the book, *Theory of Microwave*

Remote Sensing, (Wiley-Interscience, New York 1985). He is an associate editor of *Radio Science*, an associate editor of *IEEE Trans. on Geoscience and Remote Sensing*, an editor of *Journal of Electromagnetic Waves and Applications* and also on the editorial board of *Waves in Random Media*. He is a fellow of IEEE.

J. A. Kong is Professor of Electrical Engineering and Chairman of Area IV on Energy and Electromagnetic Systems in the Department of Electrical Engineering and Computer Science at the Massachusetts Institute of Technology in Cambridge, Massachusetts. His research interest is in the field of electromagnetic wave theory and applications. He has published 7 books and over 300 refereed journal and conference papers, and is the Editor of the Wiley Series in Remote Sensing, and Chief Editor of the Elsevier book series of Progress In Electromagnetics Research (PIER).



Variance of Phase Fluctuations of Waves Propagating through a Random Medium

N. C. Chu, J. A. Kong, H. A. Yueh, and S. V. Nghiem

Department of Electrical Engineering and Computer Science
and Research Laboratory of Electronics
Massachusetts Institute of Technology
Cambridge, MA 02139, USA

J. G. Fleischman, S. Ayasli, and R. T. Shin

MIT Lincoln Laboratory
Lexington, MA 02173, USA

Abstract—As an electromagnetic wave propagates through a random scattering medium, such as a forest, its energy is attenuated and random phase fluctuations are induced. The magnitude of the random phase fluctuations induced is important in estimating how well a Synthetic Aperture Radar (SAR) can image objects within the scattering medium. The two-layer random medium model, consisting of a scattering layer between free space and ground, is used to calculate the variance of the phase fluctuations induced between a transmitter located above the random medium and a receiver located below the random medium. The scattering properties of the random medium are characterized by a correlation function of the random permittivity fluctuations. The effective permittivity of the random medium is first calculated using the strong fluctuation theory, which accounts for large permittivity fluctuations of the scatterers. The distorted Born approximation is used to calculate the first-order scattered field. A perturbation series for the phase of the received field in the Rytov approximation is then introduced and the variance of the phase fluctuations is solved to first order in the permittivity fluctuations. The variance of the phase fluctuations is also calculated assuming that the transmitter and receiver are in the paraxial limit of the random medium, which allows an analytic solution to be obtained. Results are compared using the paraxial approximation, scalar Green's function formulation, and dyadic Green's function formulation. The effects studied are the dependence of the variance of the phase fluctuations on receiver location in lossy and lossless regions, medium thickness, correlation length and fractional volume of scatterers, depolarization of the incident wave, ground layer permittivity, angle of incidence, and polarization.

1. INTRODUCTION

As an electromagnetic wave propagates through a random scattering medium, its energy is attenuated and random phase fluctuations are induced. The ability to calculate these phase fluctuations is of practical interest. Members of the remote sensing community interested in using SAR to detect and image objects within scattering media must use this information as an integral part of their system design. A forest is an example of such a scattering medium, where fluctuations in the density and distribution of foliage induces random phase fluctuations. These

phase fluctuations spread the target return into neighboring range-Doppler cells, thus smearing the image. The magnitude of these fluctuations determines the extent of the range-Doppler spreading and hence gives an estimate of how well targets under foliage can be imaged. The objective of this work is to calculate the phase fluctuations that an electromagnetic wave undergoes as it propagates through a random medium.

The random medium model can be analyzed by using the wave theory approach [1]. This approach begins with Maxwell's equations and develops solutions for the electric field after taking into account absorption and scattering by the medium. The wave theory approach has often been used for studying wave propagation and scattering in continuous random media. Tatarskii and Gertsenshtein [2] studied the propagation of a scalar wave in a homogeneous isotropic medium with quasi-static fluctuations. Lee and Kong [3] studied wave propagation and scattering in a two-layer anisotropic random medium using the bilocal and the nonlinear approximations. They calculated the effective propagation constants of the four characteristic waves associated with the coherent vector fields propagating in an anisotropic random medium, which correspond to the upward- and downward-propagating vectors of the ordinary and extraordinary waves.

The wave theory approach has also been used to calculate backscattering cross sections for continuous random media with lateral and vertical correlations. This has been done by Tsang and Kong [4], Zuniga et al. [5,6], Zuniga and Kong [7], Lin et al. [8], and Borgcaud et al. [9-11]. Stogryn [12] used the first-order renormalization method on a spherically symmetric correlation function, and Fung and Fung [13] used the same method on a cylindrically symmetric correlation function. The modeling of vegetation using the random medium model and wave theory has also been applied by de Wolf [14], Rosenbaum and Bowles [15], Tan et al. [16], Chuah and Tan [17], Tsang and Kong [18], and Nghiem et al. [19].

In this paper, the wave theory approach is used to calculate the variance of the phase fluctuations. In Section 2, the problem is formulated and the random medium model introduced. In Section 3, calculations using the paraxial approximation are shown. In Section 4, calculations using the two-layer dyadic Green's function are discussed. In Section 5, numerical results are presented, and in Section 6, a brief summary is given.

2. FORMULATION

Distorted Born Approximation and Strong Fluctuation Theory

The distorted Born approximation and the strong fluctuation theory are used to calculate the transmitted scattered field. The total electric field transmitted through the random medium to the region of the receiver is (see Figs. 1 and 2)

$$\bar{E}_t(\bar{r}) = \bar{E}_t^{(0)}(\bar{r}) + \bar{E}_{ts}(\bar{r}) \tag{1}$$

where the scattered or incoherent electric field, $\bar{E}_{ts}(\bar{r})$, is found by using the distorted Born approximation [20] and is

$$\bar{E}_{ts}(\bar{r}) \approx k_0^2 \iiint_{V_1} d^3\bar{r}_1 \bar{\epsilon}_{21}(\bar{r}, \bar{r}_1) \cdot \xi(\bar{r}_1) \bar{E}_1^{(0)}(\bar{r}_1) \tag{2}$$

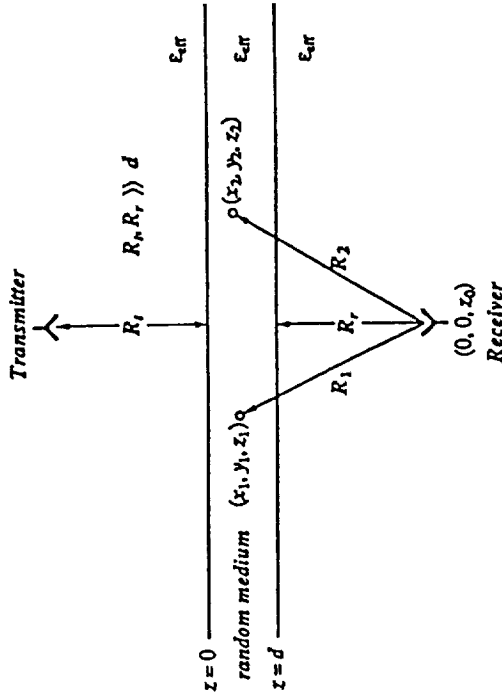


Figure 1. Geometrical configuration for phase fluctuation calculation in the paraxial limit.

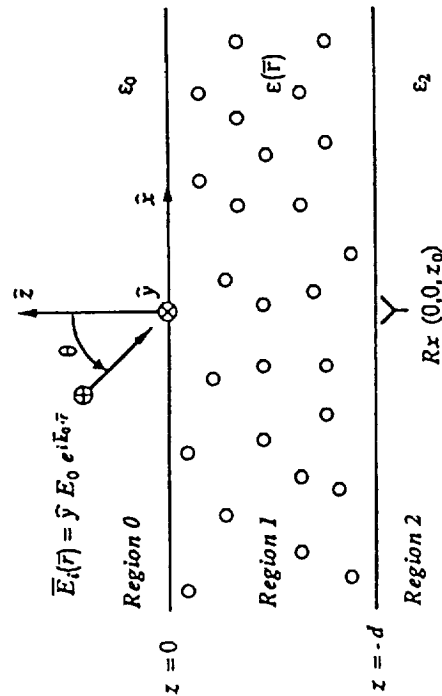


Figure 2. Geometrical configuration for phase fluctuation calculation using two layer dyadic Green's function formulation.



The fields $\overline{E}_1^{(0)}(\overline{r})$ and $\overline{E}_l^{(0)}(\overline{r})$ are the zeroth-order mean or coherent fields in Regions 1 and 2, respectively. The dyadic Green's function, \overline{G}_{21} , is defined in Appendix A.

The renormalized scattering source, $\xi(\overline{r})$, is obtained using the strong fluctuation theory [20,21]. It is specified as

$$\xi(\overline{r}) = 3 \frac{\epsilon_g}{\epsilon_0} \left(\frac{\epsilon(\overline{r}) - \epsilon_g}{\epsilon(\overline{r}) + 2\epsilon_g} \right) \quad (3)$$

and ϵ_g is determined by requiring $\langle \xi(\overline{r}) \rangle = 0$ (4)

$$f \left(\frac{\epsilon_s - \epsilon_g}{\epsilon_s + 2\epsilon_g} \right) + (1 - f) \left(\frac{\epsilon_0 - \epsilon_g}{\epsilon_0 + 2\epsilon_g} \right) = 0 \quad (5)$$

where f is the fractional volume of the scatterers and ϵ_s is the permittivity of the scatterers.

In the low frequency limit, the effective permittivity is given by [20-24]

$$\epsilon_{eff} = \epsilon_g + \epsilon_0 \frac{2}{3} k_0^2 \int_0^\infty dr r C_\xi(\overline{r}) + i \frac{2}{3} k_0^2 k_g \epsilon_0 U \quad (6)$$

where

$$U = \int_0^\infty dr r^2 C_\xi(\overline{r}) \quad (7)$$

$$C_\xi(\overline{r}) = \delta e^{-r/l} \quad (8)$$

C_ξ is a spherically symmetric correlation function of $\xi(\overline{r})$, where δ is the variance of $\xi(\overline{r})$ and l is the correlation length of $\xi(\overline{r})$ and roughly approximates the size of the scatterers.

Scalar Green's Function

When all the depolarization effects and boundary effects are neglected, a scalar Green's function is obtained. This Green's function is used in the paraxial approximation, and is also used to calculate the variance of the phase fluctuations with the receiver at arbitrary distances from the random medium. In this paper, the calculations are shown only for the paraxial approximation.

When depolarization and boundary effects are neglected, the dyadic Green's function in (2) is replaced by a scalar Green's function. Therefore, the scattered field for this approximation is written as

$$\overline{E}_{ts}(\overline{r}) \simeq k_0^2 \iiint_{V_1} d^3\overline{r}_1 G(\overline{r}, \overline{r}_1) \xi(\overline{r}_1) \overline{E}_l^{(0)}(\overline{r}_1) \quad (9)$$

where the scalar Green's function is [25]

$$G(\overline{r}) = \frac{i}{(2\pi)^2} \iint_{-\infty}^{+\infty} d^2\overline{k}_\perp \frac{1}{2k_z} e^{i\overline{k}_\perp \cdot \overline{r}_\perp - ik_z z} \quad (10)$$

$$= \frac{e^{ik_z r}}{4\pi R} \quad (11)$$

and $\overline{k}_\perp = k_x \hat{x} + k_y \hat{y}$, $\overline{r}_\perp = x\hat{x} + y\hat{y}$, $k_z = \sqrt{k_{eff}^2 - k_x^2 - k_y^2}$. R is the distance from a scatterer in the random medium to the receiver (see Fig. 1). Note that this formulation assumes that the permittivity of the regions above and below the random medium are the same as the effective permittivity of the random medium.

Paraxial Approximation

When the distance that the receiver is from the random medium, R_r in Fig. 1, is assumed to be much greater than the thickness of the medium and the correlation length of $\xi(\overline{r})$, then the paraxial approximation can be made. The result of this approximation is that the scalar Green's function can be expressed as

$$G(\overline{r}) = \frac{e^{ik_{eff}R}}{4\pi R} \simeq \frac{\exp \left\{ i k_{eff} \left[(z_0 - z_1) + \frac{z_1^2 + y_1^2}{2(z_0 - z_1)} \right] \right\}}{4\pi(z_0 - z_1)} \quad (12)$$

The details of this approximation are discussed in Section 3.

Phase Fluctuations

In calculating the phase fluctuations of the received field, a perturbation series in the phase of the received field is introduced for each polarization. Hence, to find the phase fluctuations for H-Polarization, an incident field polarized in the h -direction is used and the complex phase is calculated for this case. The same is done for an incident field polarized in the v -direction to find the phase fluctuations for V-Polarization.

To find the phase fluctuations for H-Polarization, the total field in Region 2 is written in the Rytov approximation as

$$E_{2h}(\overline{r}) = E_{2h}^{(0)}(\overline{r}) e^{i\Phi_h(\overline{r})} \simeq E_{2h}^{(0)}(\overline{r}) + E_{2sh}(\overline{r}) \quad (13)$$

where $\Phi_h(\overline{r})$ is the complex phase for H-Polarization, and the subscript h denotes horizontally-polarized fields.

Assuming small fluctuations, it is appropriate to approximate the exponential $e^{i\Phi_h(\overline{r})}$ in (13) by the first two terms of its Taylor series expansion. Note that this assumption is valid for the numerical results illustrated in Section 5, whose standard deviation is in general smaller than 20 degrees. The solution for the complex phases is

$$\Phi_h(\overline{r}) \simeq -i \frac{E_{2sh}(\overline{r})}{E_{2h}^{(0)}(\overline{r})}, \quad \Phi_v(\overline{r}) \simeq -i \frac{E_{2sv}(\overline{r})}{E_{2v}^{(0)}(\overline{r})} \quad (14)$$

The complex phase, $\Phi(\overline{r})$, contains both phase and amplitude fluctuation information, and can be written explicitly in terms of its real and imaginary parts as $\Phi(\overline{r}) = \psi(\overline{r}) + i\alpha(\overline{r})$, where $\psi(\overline{r})$ and $\alpha(\overline{r})$ correspond to phase and amplitude fluctuations, respectively. To extract the phase fluctuation information, the quantities $\langle \Phi_h(\overline{r}_a) \Phi_h^*(\overline{r}_a) \rangle$, $\langle \Phi_h(\overline{r}_a) \Phi_h(\overline{r}_a) \rangle$, $\langle \Phi_v(\overline{r}_a) \Phi_v^*(\overline{r}_a) \rangle$, and $\langle \Phi_v(\overline{r}_a) \Phi_v(\overline{r}_a) \rangle$ must be found. The variances are then



$$\sigma_{\psi_h}^2 = \langle \psi_h^2 \rangle = \frac{\langle \Phi_h(\bar{r}_a) \Phi_h^*(\bar{r}_a) \rangle + \text{Re} \langle \Phi_h(\bar{r}_a) \Phi_h(\bar{r}_a) \rangle}{2} \quad (15)$$

$$\sigma_{\psi_v}^2 = \langle \psi_v^2 \rangle = \frac{\langle \Phi_v(\bar{r}_a) \Phi_v^*(\bar{r}_a) \rangle + \text{Re} \langle \Phi_v(\bar{r}_a) \Phi_v(\bar{r}_a) \rangle}{2} \quad (16)$$

For the scalar Green's function and the paraxial approximation, no distinction is made between the polarizations. Therefore,

$$\Phi(\bar{r}) = \Phi_h(\bar{r}) = \Phi_v(\bar{r}) \simeq -i \frac{E_{ts}(\bar{r})}{E_t^{(0)}(\bar{r})} \quad (17)$$

and the variance is calculated as shown above using this value of $\Phi(\bar{r})$.

3. PARAXIAL APPROXIMATION METHOD

The variance of the phase fluctuations for the case of a transmitter and a receiver located far away from the random medium (in the paraxial limit) is calculated in this section. The configuration is shown in Fig. 1. This problem is motivated by the fact that the results are simpler and obtainable in closed form. The closed form results will be used to verify the validity of the numerical results obtained by using the Green's function approach in the following section.

The incident field is assumed to be a plane wave normally incident on the random medium in the z direction (for this formulation the positive z -axis points downward), and is written as

$$\bar{E}_i(\bar{r}) = \hat{x} e^{ik_e l / z} \quad (18)$$

The expression for the complex phase is

$$\Phi(\bar{r}) \simeq -i e^{-ik_e l / z} k_0^2 \iiint_{V_1} d^3 \bar{r}_1 \frac{e^{ik_e l / R_1}}{4\pi R_1} \xi(\bar{r}_1) e^{ik_e l / z_1} \quad (19)$$

Calculation of $\langle \Phi(\bar{r}_a) \Phi^*(\bar{r}_a) \rangle$

The expression for $\langle \Phi(\bar{r}_a) \Phi^*(\bar{r}_a) \rangle$ is obtained from (19) and is

$$\langle \Phi(\bar{r}_a) \Phi^*(\bar{r}_a) \rangle = \frac{k_0^4}{(4\pi)^2} \iiint_{V_1} d^3 \bar{r}_1 \iiint_{V_2} d^3 \bar{r}_2 \frac{\langle \xi(\bar{r}_1) \xi^*(\bar{r}_2) \rangle}{R_1 R_2} \times e^{ik_e l / (z_1 + R_1 - z_0)} e^{-ik_e l / (z_2 + R_2 - z_0)} \quad (20)$$

From Fig. 1, R_1 can be written in cartesian coordinates as

$$R_1 = \sqrt{x_1^2 + y_1^2 + (z_0 - z_1)^2} \quad (21)$$

and R_2 can be written in a similar manner. In the paraxial approximation, the scatterers that will contribute to the received scattered field will be limited to those close to the transmitter-receiver axis (close relative to the scatterer-to-receiver distance). This means that the transverse coordinates of the contributing scatterers, $x_{1,2}$ and $y_{1,2}$, will be small relative to the distances to the receiver,

$(z_0 - z_{1,2})$. The reason that the contributing scatterers are limited to those close to the transmitter-receiver axis is that the farther off-axis the scatterers are, the more rapidly varying their phases become; therefore, contribution can be considered to come from scatterers near the axis because they have stationary phases. Also, the scatterers far off-axis will not contribute as much as those close to the axis because attenuation in the lossy medium will lessen the contribution of those scatterers with the longer path lengths to the receiver. Because the effective values of $x_{1,2}$ and $y_{1,2}$ are small relative to $(z_0 - z_{1,2})$, the following Taylor series expansions of R_1 and R_2 can be taken:

$$R_{1,2} = (z_0 - z_{1,2}) \left(1 + \frac{x_{1,2}^2 + y_{1,2}^2}{2(z_0 - z_{1,2})^2} + \dots \right) \quad (22)$$

The first term and the first two terms of the above expression are used in the magnitudes and phases of (20), respectively.

For the receiver to be in the paraxial limit of the random medium, the distance that the receiver is from the bottom of the medium must be much greater than the thickness of the medium. This means that the thickness becomes a negligible quantity relative to the receiver location. Physically, the receiver is so far away from the medium that the medium appears to be just a "screen" of scatterers. Therefore, the quantities $(z_0 - z_1)$ and $(z_0 - z_2)$ of R_1 and R_2 above are approximated by the receiver to medium distance, R_r .

The $\langle \xi(\bar{r}_1) \xi^*(\bar{r}_2) \rangle$ term corresponds to the correlation function introduced in Section 2. It is written in cartesian coordinates as

$$C(\bar{r}_1 - \bar{r}_2) = \delta e^{-\sqrt{(x_1 - x_2)^2 + (y_1 - y_2)^2 + (z_1 - z_2)^2} / l} \quad (23)$$

where δ is the variance and l is the correlation length of $\xi(\bar{r})$. A spherically symmetric correlation function is used for analytic convenience.

The following change of variables is performed to eliminate the dependence of the correlation function on three of the integrations:

$$x_c = \frac{x_1 + x_2}{2}, \quad y_c = \frac{y_1 + y_2}{2}, \quad z_c = \frac{z_1 + z_2}{2} \quad (24)$$

$$x_d = \frac{x_1 - x_2}{2}, \quad y_d = \frac{y_1 - y_2}{2}, \quad z_d = \frac{z_1 - z_2}{2} \quad (25)$$

The Jacobian for this coordinate change equals eight. After implementing the change of variables and simplifying terms, the resulting expression is

$$\langle \Phi(\bar{r}_a) \Phi^*(\bar{r}_a) \rangle = \frac{\delta k_0^4}{2\pi^2 R_r^2} \iiint_{V_c} d^3 \bar{r}_c \iiint_{V_d} d^3 \bar{r}_d \exp \left\{ -\frac{2}{l} \sqrt{x_d^2 + y_d^2 + z_d^2} \right\} \times \exp \left\{ -\frac{k''_{eff}}{R_r} x_c^2 \right\} \exp \left\{ \frac{k''_{eff}}{R_r} 2x_d x_c \right\} \exp \left\{ -\frac{k''_{eff}}{R_r} y_c^2 \right\} \times \exp \left\{ \frac{k''_{eff}}{R_r} 2y_d y_c \right\} \exp \left\{ -\frac{k''_{eff}}{R_r} (x_d^2 + y_d^2) \right\} \quad (26)$$

where k''_{eff} and k''_{eff} are the real and imaginary parts of k_{eff} , respectively.



After carrying out the integrations over x_c and y_c analytically, the exponentials of order x_d^2 and y_d^2 are neglected. This is valid because in order for the correlation function to be non-zero, x_d and y_d must be smaller than l , which is a small quantity, and it has been assumed that R_r is much greater than l . Assuming that the thickness of the medium, d , is much greater than l and making use of the Laplace method for the integration of z_d , the final expression for $\langle \Phi(\bar{\tau}_a) \Phi^*(\bar{\tau}_a) \rangle$ is

$$\langle \Phi(\bar{\tau}_a) \Phi^*(\bar{\tau}_a) \rangle = \frac{\delta_0 k_0^4 d^3}{2 R_r k_e f f} \quad (27)$$

Calculation of $\langle \Phi(\bar{\tau}_a) \Phi(\bar{\tau}_a) \rangle$

The expression for $\langle \Phi(\bar{\tau}_a) \Phi(\bar{\tau}_a) \rangle$ is obtained from the expression for $\Phi(\bar{\tau})$ in (19), and has the same form as (20). A $\langle \xi(\bar{\tau}_1) \xi(\bar{\tau}_2) \rangle$ term is obtained and is a correlation function similar to the one used in the previous subsection, except the complex variance of $\xi(\bar{\tau})$, δ_0 , is used instead of δ .

The same approximations for $R_1, R_2, z_0 - z_1$, and $z_0 - z_2$ that were made in the previous subsection are made here, and the same change of variables is also made. After these approximations and substitutions are made and the resulting expression simplified, the following is obtained:

$$\langle \Phi(\bar{\tau}_a) \Phi(\bar{\tau}_a) \rangle = -\frac{\delta_0 k_0^4}{2 \pi^2 R_r^2} \iiint_{V_c} d^3 \bar{\tau}_c \iiint_{V_d} d^3 \bar{\tau}_d \exp \left\{ -\frac{2}{l} \sqrt{x_d^2 + y_d^2 + z_d^2} \right\} \times \exp \left\{ i \frac{k_e f f}{R_r} (x_c^2 + x_d^2 + y_c^2 + y_d^2) \right\} \quad (28)$$

The integrations over x_c and y_c are carried out exactly. The exponentials of order x_d^2 and y_d^2 are again neglected. The remaining integrations and the integrand are now the same as in the previous subsection, and are carried out in the same manner. The final result is

$$\langle \Phi(\bar{\tau}_a) \Phi(\bar{\tau}_a) \rangle = -\frac{\delta_0 k_0^4 i d^3}{2 R_r k_e f f} \quad (29)$$

which is similar in form to the result for $\langle \Phi(\bar{\tau}_a) \Phi^*(\bar{\tau}_a) \rangle$.

4. DYADIC GREEN'S FUNCTION METHOD

The variance of the phase fluctuations for the case of a plane wave incident on a random medium at arbitrary angles of incidence and accounting for boundary and depolarization effects is calculated in this section. The two-layer dyadic Green's function is used in these calculations, and is the most general of the formulations used in this study. The configuration for this problem is shown in Fig. 2. This is the configuration for the general two-layer problem, where there are three distinct regions separated by two boundaries. The permittivity of each of the three regions can be specified, but for this study, Region 0 is assumed to be free space.

Calculations for H-Polarization

The incident and mean fields are (for this formulation the positive z -axis points upward)

$$\bar{E}_i(\bar{r}) = \hat{y} e^{i\bar{k}_{m,1} \cdot \bar{r}_\perp} e^{-ik_{0z} z} = \hat{y} e^{ik_{zm} z} e^{-ik_{0z} z} \quad (30)$$

$$\bar{E}_1^{(0)}(\bar{r}) = \hat{y} \left[B_1^{\text{TE}} e^{-ik_{1zm} z} + A_1^{\text{TE}} e^{ik_{1zm} z} \right] e^{ik_{zm} z} \quad (31)$$

$$\bar{E}_2^{(0)}(\bar{r}) = \hat{y} T_m^{\text{TE}} e^{-ik_{2zm} z} e^{ik_{zm} z} \quad (32)$$

where the z -directed wavenumbers in the expressions above are the mean wavenumbers in each of the regions and it has been assumed that the incident field is polarized in the y -direction and propagating in the x - and z -directions. The up-going and down-going waves in each of the regions consist of an infinite series of waves, the sums of which are denoted by the coefficients shown above. For TE polarization, the coefficients are determined to be [1]

$$R_m^{\text{TE}} = \frac{R_{01}^{\text{TE}} + R_{12}^{\text{TE}} e^{i2k_{1zm} d}}{1 + R_{01}^{\text{TE}} R_{12}^{\text{TE}} e^{i2k_{1zm} d}} \quad (33)$$

$$T_m^{\text{TE}} = \frac{4 e^{i(k_{1zm} - k_{2zm})d}}{(1 + P_{01}^{\text{TE}})(1 + P_{12}^{\text{TE}})(1 + R_{01}^{\text{TE}} R_{12}^{\text{TE}} e^{i2k_{1zm} d})} \quad (34)$$

$$A_1^{\text{TE}} = \frac{R_m^{\text{TE}} + 1}{2} + \frac{k_{0zm}}{2k_{1zm}} (R_m^{\text{TE}} - 1) \quad (35)$$

$$B_1^{\text{TE}} = \frac{R_m^{\text{TE}} + 1}{2} - \frac{k_{0zm}}{2k_{1zm}} (R_m^{\text{TE}} - 1) \quad (36)$$

where the reflection coefficients, $R_{ij}^{\text{TE,TM}}$, are defined in (84)–(85).

Note that scalar electric fields are used in the expressions for the complex phases in (14). To obtain the scalar fields, the vector fields are dot-multiplied with the appropriate unit vector. For H-Polarization, the scalar scattered field is obtained by dot-multiplying the vector scattered field with $\hat{h}(k_{2zm})$, the unit vector in the region of the receiver. Thus, the scalar scattered field in the region of the receiver is

$$E_{2sh}(\bar{r}) \simeq \hat{h}(k_{2zm}) \cdot k_0^2 \iiint_{V_1} d^3 \bar{\tau}_1 \bar{C}_{21}(\bar{r}, \bar{\tau}_1) \cdot \xi(\bar{\tau}_1) \bar{E}_1^{(0)}(\bar{\tau}_1) \quad (37)$$

In order to simplify the equations below, the dot-products of the unit vectors are written in shorthand as follows:

$$\hat{h}(k_{2zm}) \cdot \hat{h} \left(-k_{2z}^{(l)} \right) = \frac{k_{lz}}{\sqrt{k_{lx}^2 + k_{ly}^2}} \equiv \text{HH}_{22}(k_{l\perp}) \quad (38)$$

$$\hat{h}(k_{2zm}) \cdot \hat{v} \left(-k_{2z}^{(l)} \right) = \frac{k_{2z}^{(l)} k_{ly}}{k_2 \sqrt{k_{lx}^2 + k_{ly}^2}} \equiv \text{HV}_{22}(k_{l\perp}) \quad (39)$$

$$\hat{h} \left(k_{1z}^{(l)} \right) \cdot \hat{h}(k_{1zm}) = \text{HH}_{22}(k_{l\perp}) \quad (40)$$

$$\hat{h} \left(-k_{1z}^{(l)} \right) \cdot \hat{h}(k_{1zm}) = \text{HH}_{22}(k_{l\perp}) \quad (41)$$

$$\hat{v}(k_{1z}^{(1)}) \cdot \hat{h}(k_{1zm}) = \frac{-k_{1z}^{(1)} k_{ly}}{k_{eff} \sqrt{k_{1z}^2 + k_{ly}^2}} \equiv VH_{11}(k_{1L}) \quad (42)$$

$$\hat{v}(-k_{1z}^{(1)}) \cdot \hat{h}(k_{1zm}) = -VH_{11}(k_{1L}) \quad (43)$$

where the mean unit vectors $\hat{h}(k_{0zm})$, $\hat{h}(k_{1zm})$, and $\hat{h}(k_{2zm})$ are equal to \hat{y} and l equals 1 or 2 corresponding to the integration over \bar{k}_{1L} or \bar{k}_{2L} , respectively. The first two quantities above correspond to the dot-products of the unit vector outside the integral in (37) with the outside vectors of \bar{G}_{21} . The last four quantities are the dot-products of the inside vectors of the Green's function with the mean electric field in Region 1.

After making the above definitions, the complex phase is

$$\begin{aligned} \Phi_h(\bar{r}) = & \frac{e^{ik_{2zm}z} k_0^2}{T_m^{\text{TE}} e^{ik_{zm}z} 8\pi^2} \iiint_{V_1} d^3\bar{r}_1 \iint d^2\bar{k}_{1L} \frac{e^{i\bar{k}_{1L} \cdot (\bar{r}_1 - \bar{r}_{1L})} e^{-ik_{2z}(z+d)} e^{ik_{1z}z}}{k_{1z}} \\ & \times \left\{ \frac{T_{12}^{\text{TE}}(k_{1L})}{D_2(k_{1L})} \text{HH}_{22}(k_{1L}) \text{HH}_{22}(k_{1L}) \left[R_{10}^{\text{TE}}(k_{1L}) e^{-ik_{1z}z_1} + e^{ik_{1z}z_1} \right] \right. \\ & + \frac{k_{eff} T_{12}^{\text{TM}}(k_{1L})}{k_2 F_2(k_{1L})} \text{HV}_{22}(k_{1L}) \text{VH}_{11}(k_{1L}) \left[R_{10}^{\text{TM}}(k_{1L}) e^{-ik_{1z}z_1} - e^{ik_{1z}z_1} \right] \left. \right\} \\ & \times \xi(\bar{r}_1) \left[B_1^{\text{TE}} e^{-ik_{1zm}z_1} + A_1^{\text{TE}} e^{ik_{1zm}z_1} \right] e^{ik_{zm}z_1} \quad (44) \end{aligned}$$

With this expression for the complex phase, the quantities $\langle \Phi_h(\bar{r}_a) \Phi_h^*(\bar{r}_a) \rangle$ and $\langle \Phi_h(\bar{r}_a) \Phi_h(\bar{r}_a) \rangle$ can be calculated as shown below. For the remainder of this section, the field point \bar{r}_a will not be explicitly written out.

Calculation of $\langle \Phi_h \Phi_h^* \rangle$

The expression for $\langle \Phi_h \Phi_h^* \rangle$ is obtained from (44) and is

$$\begin{aligned} \langle \Phi_h \Phi_h^* \rangle = & \frac{k_0^4 e^{i(k_{2zm} - k_{2zm})z}}{64\pi^4 T_m^{\text{TE}} T_m^{\text{TE}} T_m^{\text{TE}} e^{i(k_{zm} - k_{zm})z}} \iiint_{V_1} d^3\bar{r}_1 \iiint_{V_2} d^3\bar{r}_2 \iint d^2\bar{k}_{1L} \iint d^2\bar{k}_{2L} \\ & \times e^{i\bar{k}_{1L} \cdot (\bar{r}_1 - \bar{r}_{1L})} e^{-i\bar{k}_{2L} \cdot (\bar{r}_1 - \bar{r}_{2L})} e^{-ik_{2z}^*(z+d)} e^{ik_{2z}^{(2)*}(z+d)} e^{i(k_{1z}^{(1)} - k_{1z}^{(2)*})d} \\ & \times \left[A e^{-ik_{1z}^{(1)}z_1} + B e^{ik_{1z}^{(1)}z_1} + C e^{-ik_{1z}^{(1)}z_1} - D e^{ik_{1z}^{(1)}z_1} \right] \left[B_1 e^{-ik_{1zm}z_1} + A_1 e^{ik_{1zm}z_1} \right] \\ & \times \left[E e^{ik_{1z}^{(2)*}z_2} + F e^{-ik_{1z}^{(2)*}z_2} + G e^{ik_{1z}^{(2)*}z_2} - H e^{-ik_{1z}^{(2)*}z_2} \right] \left[B_1^* e^{ik_{1zm}z_2} + A_1^* e^{-ik_{1zm}z_2} \right] \\ & \times e^{ik_{zm}z_1} e^{-ik_{zm}z_2} \frac{(\xi(\bar{r}_1) \xi^*(\bar{r}_2))}{k_{1z}^{(1)} k_{1z}^{(2)*}} \quad (45) \end{aligned}$$

where the coefficients A through H are defined in Appendix B and the constants A_1 and B_1 are defined in (33)-(36). Also,

$$k_{1z}^{(1)} = \sqrt{k_{eff}^2 - k_{1z}^2 - k_{1y}^2}, \quad k_{1z}^{(2)*} = \sqrt{k_{eff}^2 - k_{2z}^2 - k_{2y}^2} \quad (46)$$

$$k_{2z}^{(1)} = \sqrt{k_{2z}^2 - k_{1z}^2 - k_{1y}^2}, \quad k_{2z}^{(2)} = \sqrt{k_{2z}^2 - k_{2z}^2 - k_{2y}^2} \quad (47)$$

The superscripts of $k_{1z}^{(1)}$ and $k_{2z}^{(1)}$ associate the z -directed wavenumbers with the integration variable \bar{k}_{1L} . Likewise, the superscripts of $k_{1z}^{(2)}$ and $k_{2z}^{(2)}$ associate the z -directed wavenumbers with the integration variable \bar{k}_{2L} . In the above expressions, the mean wavenumber in the x direction, k_{zm} , is real because Region 0 is free-space, and the same in all three regions from phase matching conditions.

The correlation function used is the same spherically symmetric correlation function used in the previous section, but the form which is used is the Fourier transform of the spectral intensity function [1] and is given by

$$C(\bar{r}_1 - \bar{r}_2) = \delta \iiint d^3\bar{\beta} \frac{l^3}{\pi^2(1 + \beta^2 l^2)^2} e^{-i\bar{\beta} \cdot (\bar{r}_{1L} - \bar{r}_{2L}) - i\beta z_1(z_1 - z_2)} \quad (48)$$

where δ is the variance and l is the correlation length of $\zeta(\bar{r})$.

Integrating over the perpendicular spatial components, \bar{r}_{1L} and \bar{r}_{2L} , the limits of which are from $-\infty$ to $+\infty$, yields delta functions. Integrating over \bar{k}_{1L} and \bar{k}_{2L} , which are in the arguments of the delta functions and also with the limits of integration from $-\infty$ to $+\infty$, results in the following requirements:

$$\bar{k}_{1L} = \bar{k}_{2L} = \bar{k}_{mL} - \bar{\beta}_L \quad (49)$$

$$\Rightarrow k_{1z}^{(1)} = \sqrt{k_{eff}^2 - k_{1L}^2} = \sqrt{k_{eff}^2 - k_{2L}^2} = k_{1z}^{(2)} \quad (50)$$

$$\Rightarrow k_{2z}^{(1)} = \sqrt{k_{2z}^2 - k_{1L}^2} = \sqrt{k_{2z}^2 - k_{2L}^2} = k_{2z}^{(2)} \quad (51)$$

From (50) and (51), it is apparent that the superscripts of $k_{1z}^{(1)}$, $k_{1z}^{(2)}$, $k_{2z}^{(1)}$, and $k_{2z}^{(2)}$ no longer need to be used.

The integrations of z_1 and z_2 are performed next, which leaves the final three integrations from negative to positive infinity over the variable $\bar{\beta}$. The β_z integration is performed using contour integration methods.

After carrying out the β_z integration, the integrand depends only on the variable $\bar{\beta}_L$. The last two integrations must be done numerically. To simplify the integral, the integration variables are transformed to cylindrical coordinates so that one of the integrations (the β_ϕ integration) is over finite limits and simpler to perform numerically. The following is the final result for the value of $\langle \Phi_h \Phi_h^* \rangle$, which requires two numerical integrations:

$$\begin{aligned} \langle \Phi_h \Phi_h^* \rangle = & \frac{k_0^4 \delta \epsilon^{i(k_{2zm} - k_{2zm})z}}{2\pi l T_m^{\text{TE}} T_m^{\text{TE}} T_m^{\text{TE}}} \int_0^\infty d\beta_\rho \int_0^{2\pi} d\beta_\phi \frac{\beta_\rho}{k_{1z} k_{1z}^*} e^{id(k_{1z} - k_{1z}^*)} \\ & \times e^{-ik_{2z}(z+d)} e^{ik_{2z}^*(z+d)} \sum_{(\alpha_1, \alpha_2, \beta_1, \beta_2)} \left\{ \square_{(\alpha_1, \alpha_2, \beta_1, \beta_2)} F(\kappa_1, \kappa_2) \right\} \quad (52) \end{aligned}$$

where

$$F(\kappa_1, \kappa_2) = \frac{1 - e^{id(\kappa_1 - \kappa_2)}}{(\gamma - \kappa_2)^2 (-\gamma - \kappa_2)^2 (\kappa_1 - \kappa_2)}$$

$$\begin{aligned}
 & -\frac{1}{(2\gamma)^2(\gamma+\kappa_1)(\gamma+\kappa_2)} \left[\frac{i d e^{i d(\gamma+\kappa_1)}}{1} + \left(1 - e^{i d(\gamma+\kappa_1)} \right) \left(\frac{1}{\gamma+\kappa_1} + \frac{1}{\gamma+\kappa_2} + \frac{1}{\gamma} \right) \right] \\
 & -\frac{1}{(2\gamma)^2(-\gamma+\kappa_1)(-\gamma+\kappa_2)} \left[\frac{i d e^{i d(\gamma-\kappa_2)}}{1} + \left(e^{i d(\gamma-\kappa_2)} - e^{i d(\kappa_1-\kappa_2)} \right) \right] \\
 & \times \left(\frac{1}{-\gamma+\kappa_1} + \frac{1}{-\gamma+\kappa_2} - \frac{1}{\gamma} \right) \tag{53}
 \end{aligned}$$

$$\kappa_1 = \alpha_1 k_{1z} + \alpha_2 k_{1zm}, \quad \alpha_1, \alpha_2 = -1, 1 \tag{54}$$

$$\kappa_2 = \beta_1 k_{1z}^* + \beta_2 k_{1zm}^*, \quad \beta_1, \beta_2 = -1, 1 \tag{55}$$

$$\gamma = i \sqrt{\beta_z^2 + \beta_y^2} + 1/l^2 \tag{56}$$

$$k_{1z} = \sqrt{k_{eff}^2 - (-\beta_x + k_{zm})^2} - (-\beta_y)^2 \tag{57}$$

$$k_{2z} = \sqrt{k_{eff}^2 - (-\beta_x + k_{zm})^2} - (-\beta_y)^2 \tag{58}$$

$$\beta_x = \beta_\rho \cos \beta_\phi \tag{59}$$

$$\beta_y = \beta_\rho \sin \beta_\phi \tag{60}$$

and the \square coefficients are defined in Appendix B. The three main quantities in the function F are the residues of the poles from the integration of β_z .

Calculation of $\langle \Phi_h \Phi_h \rangle$

The calculation of $\langle \Phi_h \Phi_h \rangle$ parallels the calculation of $\langle \Phi_h \Phi_h^* \rangle$ discussed above. First, the expression for $\langle \Phi_h \Phi_h \rangle$ is obtained using (44), and is very similar to (45). The coefficients A through H are defined in Appendix B. The correlation function used is the same as that used in the previous subsection, (48), except the complex variance of $\xi(\bar{r}), \delta_0$, is used instead of δ . Next, the integrations of the perpendicular components, $\bar{r}_{1\perp}, \bar{r}_{2\perp}, \bar{k}_{1\perp}$, and $\bar{k}_{2\perp}$, are performed using the same methods discussed above. The result of these integrations requires that

$$\bar{k}_{1\perp} = \bar{k}_{m\perp} - \bar{\beta}_\perp \quad \text{and} \quad \bar{k}_{2\perp} = \bar{k}_{m\perp} + \bar{\beta}_\perp$$

Note that for this case, $\bar{k}_{1\perp}$ is not equal to $\bar{k}_{2\perp}$ as in the previous subsection. The wavenumbers $k_{1z}^{(1)}, k_{1z}^{(2)}, k_{2z}^{(1)}$, and $k_{2z}^{(2)}$ must still be named differently.

The z_1 and z_2 integrations are performed next, which again leaves the three-fold integration over the variable $\bar{\beta}$. Again, the β_z integration is carried out using contour integration methods similar to those used to calculate $\langle \Phi_h \Phi_h^* \rangle$. There is a difference for this case, however, because for normal incidence $k_{1z}^{(1)}$ will equal $k_{1z}^{(2)}$, and thus it is possible for κ_1 to equal κ_2 , which yields an additional double-order pole. The result is that the value of one of the residues depends on the values of κ_1 and κ_2 , as shown below. The final result requires two numerical

integrations and is

$$\begin{aligned}
 \langle \Phi_h \Phi_h \rangle = & \frac{i k_0^4 \delta_0 e^{i 2 k_{2zm} z}}{2 \pi l T_m^2 T_m^2} \int_0^\infty d\beta_\rho \int_0^{2\pi} d\beta_\phi \frac{\beta_\rho}{k_{1z}^{(1)} k_{1z}^{(2)}} e^{i d(k_{1z}^{(1)} + k_{1z}^{(2)})} \\
 & \times e^{-i k_{2z}^{(1)}(z+d)} e^{-i k_{2z}^{(2)}(z+d)} \sum_{(\alpha_1, \alpha_2, \beta_1, \beta_2)} \left\{ \square_{(\alpha_1, \alpha_2, \beta_1, \beta_2)} G(\kappa_1, \kappa_2) \right\} \tag{62}
 \end{aligned}$$

where

$$G(\kappa_1, \kappa_2) = + \left\{ \frac{1 - e^{i d(\kappa_1 - \kappa_2)}}{(\gamma - \kappa_2)^2 (-\gamma - \kappa_2)^2 (\kappa_1 - \kappa_2)} \right\}$$

$$- \frac{1}{(2\gamma)^2 (\gamma + \kappa_1)(\gamma + \kappa_2)} \left[\frac{i d e^{i d(\gamma + \kappa_1)}}{1} + \left(1 - e^{i d(\gamma + \kappa_1)} \right) \left(\frac{1}{\gamma + \kappa_1} + \frac{1}{\gamma + \kappa_2} + \frac{1}{\gamma} \right) \right]$$

$$- \frac{1}{(2\gamma)^2 (-\gamma + \kappa_1)(-\gamma + \kappa_2)} \left[\frac{i d e^{i d(\gamma - \kappa_2)}}{1} + \left(e^{i d(\gamma - \kappa_2)} - e^{i d(\kappa_1 - \kappa_2)} \right) \right]$$

$$\times \left(\frac{1}{-\gamma + \kappa_1} + \frac{1}{-\gamma + \kappa_2} - \frac{1}{\gamma} \right), \quad \begin{cases} \text{if } \kappa_1 \neq \kappa_2 \\ \text{if } \kappa_1 = \kappa_2 \end{cases} \tag{63}$$

$$\kappa_1 = \alpha_1 k_{1z}^{(1)} + \alpha_2 k_{1zm}, \quad \alpha_1, \alpha_2 = -1, 1 \tag{64}$$

$$\kappa_2 = \beta_1 k_{1z}^{(2)} + \beta_2 k_{1zm}, \quad \beta_1, \beta_2 = -1, 1 \tag{65}$$

$$k_{1z}^{(1)} = \sqrt{k_{eff}^2 - (-\beta_x + k_{zm})^2} - (-\beta_y)^2 \tag{66}$$

$$k_{1z}^{(2)} = \sqrt{k_{eff}^2 - (\beta_x + k_{zm})^2} - (\beta_y)^2 \tag{67}$$

$$k_{2z}^{(1)} = \sqrt{k_2^2 - (-\beta_x + k_{zm})^2} - (-\beta_y)^2 \tag{68}$$

$$k_{2z}^{(2)} = \sqrt{k_2^2 - (\beta_x + k_{zm})^2} - (\beta_y)^2 \tag{69}$$

and γ, β_x , and β_y are defined previously, (56), (59), and (60).

The four main quantities in the function G are the residues of the poles which result when integrating over β_z , where only one of the first two residues is used depending on the values of κ_1 and κ_2 as shown.

Calculations for V-Polarization

The calculation of phase fluctuations for V-Polarization is similar to the derivation for H-Polarization, with most of the differences arising from the definitions of the incident and mean fields and the resulting changes in the dot-products of the unit vectors. To begin with, the incident field is polarized in the \hat{v} -direction, and the mean fields can be found by using duality and are

$$\bar{E}_1^{(0)}(\bar{r}) = -\eta_1 \left[\hat{v}(-k_{1zm}) B_1^{TM} e^{-i k_{1zm} z} + \hat{v}(k_{1zm}) A_1^{TM} e^{i k_{1zm} z} \right] \tag{70}$$

$$\bar{E}_2^{(0)}(\bar{r}) = -\eta_2 \hat{v}(-k_{2zm}) T_m^{\text{TM}} e^{-ik_{2zm}z} e^{ik_{1zm}z} \quad (71)$$

where η_1 and η_2 are the characteristic impedances of Regions 1 and 2, respectively, and are defined as $\eta = (\mu/\epsilon)^{1/2}$. The coefficients for the up-going and down-going fields are

$$R_m^{\text{TM}} = \frac{R_{01}^{\text{TM}} + R_{12}^{\text{TM}} e^{i2k_{1zm}d}}{1 + R_{01}^{\text{TM}} R_{12}^{\text{TM}} e^{i2k_{1zm}d}} \quad (72)$$

$$T_m^{\text{TM}} = \frac{4 e^{i(k_{1zm} - k_{2zm})d}}{(1 + p_{01}^{\text{TM}})(1 + p_{12}^{\text{TM}})(1 + R_{01}^{\text{TM}} R_{12}^{\text{TM}} e^{i2k_{1zm}d})} \quad (73)$$

$$A_1^{\text{TM}} = \frac{R_m^{\text{TM}} + 1}{2} + \frac{k_{0zm}\epsilon_1}{2k_{1zm}\epsilon_0} (R_m^{\text{TM}} - 1) \quad (74)$$

$$B_1^{\text{TM}} = \frac{R_m^{\text{TM}} + 1}{2} - \frac{k_{0zm}\epsilon_1}{2k_{1zm}\epsilon_0} (R_m^{\text{TM}} - 1) \quad (75)$$

where again, the reflection coefficients, $R_{ij}^{\text{TE, TM}}$, are defined in (84)–(85).

To find the complex phase, $\Phi_v(\bar{r})$ in (14), the appropriate scalar fields must be found. For V-Polarization, the scalar scattered field is found by dot-multiplying the vector scattered field by $\hat{v}(-k_{2zm})$, the unit vector in the region of the receiver. Thus, the scalar scattered field in the region of the receiver is

$$E_{2sv}(\bar{r}) \simeq \hat{v}(-k_{2zm}) \cdot k_0^2 \iiint_{V_1} d^3\bar{r}_1 \bar{G}_{21}(\bar{r}, \bar{r}_1) \cdot \xi(\bar{r}_1) \bar{E}_1^{(0)}(\bar{r}_1) \quad (76)$$

To simplify the equations below, the dot-products of two of the unit vectors are written in shorthand as

$$\hat{v}(-k_{2zm}) \cdot \hat{h}(-k_{2z}^{(l)}) = \frac{-k_{2zm} k_{ly}}{k_2 \sqrt{k_{1z}^2 + k_{ly}^2}} \equiv \text{VH}_{22}(k_{1\perp}) \quad (77)$$

$$\hat{v}(-k_{2zm}) \cdot \hat{v}(-k_{2z}^{(l)}) = \frac{k_{2zm} k_{2z}^{(l)} k_{1z}}{k_2^2 \sqrt{k_{1z}^2 + k_{ly}^2}} + \frac{k_{zm} \sqrt{k_{1z}^2 + k_{ly}^2}}{k_2^2} \equiv \text{VV}_{22}(k_{1\perp}) \quad (78)$$

where the mean unit vectors $\hat{h}(k_{0zm})$, $\hat{h}(k_{1zm})$, $\hat{h}(k_{2zm})$ are equal to \hat{y} and l equals 1 or 2 corresponding to the integration over $k_{1\perp}$ or $k_{2\perp}$, respectively. The quantities VH_{22} and VV_{22} correspond to the dot-multiplication of the unit vector outside the integral in (76) with the outer vectors of \bar{G}_{21} .

After making the above definitions, the complex phase is written as

$$\begin{aligned} \Phi_v(\bar{r}) = & \frac{e^{ik_{2zm}z} k_0^2}{\eta_2 T_m^{\text{TM}} e^{ik_{1zm}z} 8\pi^2} \iiint_{V_1} d^3\bar{r}_1 \iint_{V_1} d^2\bar{k}_{1\perp} \frac{1}{k_{1z}} \\ & \times \left\{ \frac{T_{12}^{\text{TE}}(k_{1\perp})}{D_2(k_{1\perp})} \text{VH}_{22}(k_{1\perp}) \left[R_{10}^{\text{TE}}(k_{1\perp}) \hat{h}(k_{1z}) e^{-ik_{1z}z_1} + \hat{h}(-k_{1z}) e^{ik_{1z}z_1} \right] \right. \\ & + \frac{k_e f f T_{12}^{\text{TM}}(k_{1\perp})}{k_2 F_2(k_{1\perp})} \text{VV}_{22}(k_{1\perp}) \left[R_{10}^{\text{TM}}(k_{1\perp}) \hat{v}(k_{1z}) e^{-ik_{1z}z_1} + \hat{v}(-k_{1z}) e^{ik_{1z}z_1} \right] \left. \right\} \\ & \cdot \left[\hat{v}(-k_{1zm}) B_1^{\text{TM}} e^{-ik_{1zm}z_1} + \hat{v}(k_{1zm}) A_1^{\text{TM}} e^{ik_{1zm}z_1} \right] \xi(\bar{r}_1) \eta_1 e^{ik_{1zm}z_1} \quad (79) \end{aligned}$$

Calculation of $\langle \Phi_v \Phi_v^* \rangle$

The expression for $\langle \Phi_v \Phi_v^* \rangle$ is obtained from (79). The same steps used to evaluate $\langle \Phi_h \Phi_h^* \rangle$ are used to evaluate $\langle \Phi_v \Phi_v^* \rangle$. The only major difference is the definition of the \square coefficients, which is shown in Appendix B. The final result is

$$\begin{aligned} \langle \Phi_v \Phi_v^* \rangle = & \frac{k_0^4 \delta_0 i \eta_1 \eta_1^* e^{i(k_{2zm} - k_{2zm}^*)z}}{2\pi l \eta_2 \eta_2^* T_m^{\text{TM}} T_m^{\text{TM}*}} \int_0^\infty d\beta \rho \int_0^\infty d\beta \phi \frac{\beta \rho}{k_{1z} k_{1z}^*} e^{id(k_{1z} - k_{1z}^*)z} \\ & \times e^{-ik_{2z}(z+d)} e^{ik_{2z}^*(z+d)} \sum_{(\alpha_1, \alpha_2, \beta_1, \beta_2)} \left\{ \square_{(\alpha_1, \alpha_2, \beta_1, \beta_2)} F(\kappa_1, \kappa_2) \right\} \quad (80) \end{aligned}$$

where the values of $\kappa_1, \kappa_2, \gamma, k_{1z}, k_{2z}, \beta_x$, and β_y are defined in (54)–(60), and $F(\kappa_1, \kappa_2)$ is defined in (53). This result requires two numerical integrations.

Calculation of $\langle \Phi_v \Phi_v \rangle$

From the expression for Φ_v in (79), the expression for $\langle \Phi_v \Phi_v \rangle$ can be obtained. The same steps used to calculate $\langle \Phi_h \Phi_h \rangle$ are used to calculate $\langle \Phi_v \Phi_v \rangle$, with the appropriate coefficients used, shown in Appendix B. The final result requires two numerical integrations and is

$$\begin{aligned} \langle \Phi_v \Phi_v \rangle = & \frac{k_0^4 \delta_0 i \eta_1 \eta_1 e^{i2k_{2zm}z}}{2\pi l \eta_2 \eta_2 T_m^{\text{TM}} T_m^{\text{TM}}} \int_0^\infty d\beta \rho \int_0^\infty d\beta \phi \frac{\beta \rho}{k_{1z}^2 k_{1z}^2} e^{id(k_{1z} + k_{1z}^{(2)})z} \\ & \times e^{-ik_{2z}^{(1)}(z+d)} e^{-ik_{2z}^{(2)}(z+d)} \sum_{(\alpha_1, \alpha_2, \beta_1, \beta_2)} \left\{ \square_{(\alpha_1, \alpha_2, \beta_1, \beta_2)} G(\kappa_1, \kappa_2) \right\} \quad (81) \end{aligned}$$

where $G(\kappa_1, \kappa_2)$ is defined in (63).

5. RESULTS AND DISCUSSION

In this section, results obtained using the paraxial approximation, the scalar Green's function (introduced in Section 2 and discussed in detail in [26]), and the Dyadic Green's function formulations are compared, showing good agreement between all three methods in the common regions of validity. The dependence of the variance of the phase fluctuations on the medium parameters are next illustrated and discussed.

The first result, shown in Fig. 3, is a plot of the standard deviation of the phase fluctuations as a function of receiver location, R_r , for all three formulations. The plot shows that the results agree well when the receiver is in the paraxial limit. Note that the standard deviation of the phase fluctuations decreases as the receiver distance increases. This is caused by the lossy region between the receiver and the medium; this region has the same permittivity as the effective permittivity of the random medium, which is lossy. Attenuation due to the lossy receiver region causes the effective volume of the contributing scatterers to be less than the free-space case. The relatively fewer number of scatterers which contribute to the received scattered field causes the decrease in the variance of the phase fluctuations. Also note that when the receiver is moved close to the bottom of



the medium (which violates the paraxial limit assumption), the paraxial result (long dashed line) increases without bound, while the Green's function results have finite values.

Also note that the standard deviation of phase fluctuations for the dyadic formulation (solid line) is slightly less than those for the scalar formulation (short dashed line). This effect is caused by the fact that the dyadic formulation accounts for depolarization of the scattered field, while the scalar formulation does not. Depolarization in this sense means that the scattered field from either an H- or V-Polarized incident field will consist of both polarizations, each of which has an amplitude less than the amplitude of the incident field. Because the dyadic case was formulated such that the phase fluctuations are calculated for only like polarizations (i.e., both scattered and mean fields polarized in the same direction), and the scalar case does not make a distinction between the polarizations, the dyadic case should yield smaller phase fluctuation variance than the scalar case, as the results show. The depolarization effect is most prominent when the receiver is close to the random medium, and less prominent when the receiver is moved into the paraxial limit. This can be explained by the fact that when the receiver is far from the random medium in a lossy region, attenuation limits the scatterers that contribute to the received field to those close to the transmitter-receiver axis. The scatterers close to the axis are those above the receiver, and the scattered field from these scatterers will be polarized in the same direction as the incident field. Therefore, in the paraxial limit, there is little depolarization.

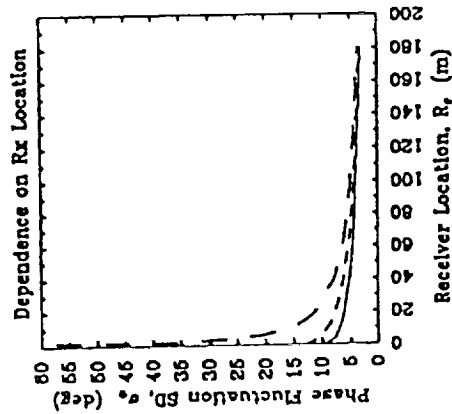


Figure 3. Phase fluctuation standard deviation (SD) dependence on receiver location. Frequency is 1.12 GHz, $\epsilon_s = (39.917 + i16.25678)\epsilon_0$, $l = 5.2$ mm, $f = 1.67\%$, $d = 10.0$ m, and $\epsilon_{eff} = (1.0505 + i0.001794)\epsilon_0$. Solid line: dyadic formulation; short dashed line: scalar formulation; long dashed line: paraxial approximation.

In Fig. 4, the standard deviation of the phase fluctuations is plotted as a function of receiver location when Region 2 is lossy (solid line), and lossless (dashed line). All the other parameters are the same as in Fig. 3. The purpose of this illustration is to verify the explanation of decreasing phase fluctuation standard deviation as a function of receiver location discussed above. As shown in Fig. 4, the standard deviation of the phase fluctuations does *not* decrease when the receiver is moved away from the random medium in a lossless region (dashed line). This is because when the receiver is moved away from the random medium, more scatterers contribute to the received scattered field since the distance that the scatterers can be from the transmitter-receiver axis before their phases vary too rapidly increases. The transverse region of contributing scatterers should increase in proportion to the medium to receiver distance, R_r , which means that the area of scatterers increases in proportion to R_r^2 . However, the power received from each of these scatterers is decreasing by $1/R_r^2$ due to the free-space path loss of the spherical waves from the scatterers. The net result is that when Region 2 is lossless, the received scattered power should change little when R_r is changed. As discussed above, the standard deviation of the phase fluctuations decreases when the receiver is moved away from the random medium in a lossy region because attenuation will decrease the number of scatterers that should contribute to the received scattered field.

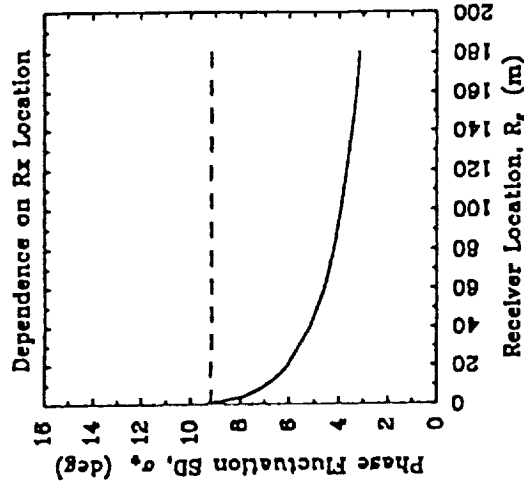


Figure 4. Phase fluctuation standard deviation (SD) for lossy and lossless Region 2. Frequency is 1.12 GHz, $\epsilon_s = (39.917 + i16.25678)\epsilon_0$, $l = 5.2$ mm, $f = 1.67\%$, $d = 10.0$ m, and $\epsilon_{eff} = (1.0505 + i0.001794)\epsilon_0$. Solid line: $\epsilon_2 = (1.0505 + i0.001794)\epsilon_0$; dashed line: $\epsilon_2 = (1.0505 + i0.0)\epsilon_0$.



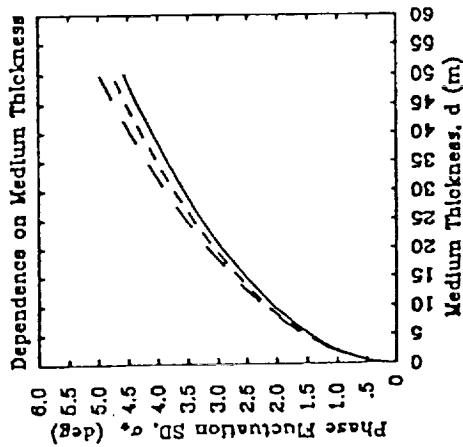


Figure 5. Phase fluctuation standard deviation (SD) dependence on medium thickness. Frequency is 1.12 GHz, $\epsilon_s = (39.917 + i16.25678)\epsilon_0$, $l = 5.2$ mm, $f = 1.67\%$, $R_r = 500.0$ m, and $\epsilon_{eff} = (1.0505 + i0.001794)\epsilon_0$. Solid line: dyadic formulation; short dashed line: scalar formulation; long dashed line: paraxial approximation.

Figure 5 shows the dependence of the phase fluctuation standard deviation on medium thickness, d , for all three formulations. The receiver is located in the paraxial limit and Region 2 has the same permittivity as the effective permittivity of Region 1. The plot shows good agreement between all the results. The behavior of the phase fluctuation standard deviation as a function of medium thickness is governed by two effects. First, increasing the thickness increases the number of scatterers in the medium, which causes an increase in scattering and hence an increase in the phase fluctuation variance. On the other hand, the increased thickness also increases the propagation path of the wave through a lossy medium, thereby reducing the effective number of scatterers which contribute to the received scattered field to those closest to the receiver. As seen in Fig. 5, for small thicknesses, the standard deviation of the phase fluctuations increases relatively rapidly when medium thickness is increased, in accordance with the argument that the increased number of scatterers causes an increase in the phase fluctuation variance. For larger medium thicknesses, the phase fluctuation standard deviation increases relatively slowly as the thickness is increased, and this is in accordance with the argument that the number of effective scatterers is not increasing as rapidly.

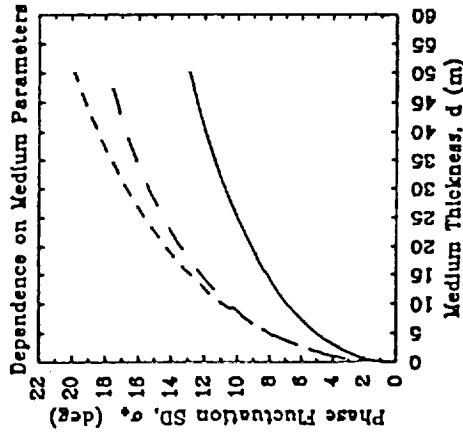
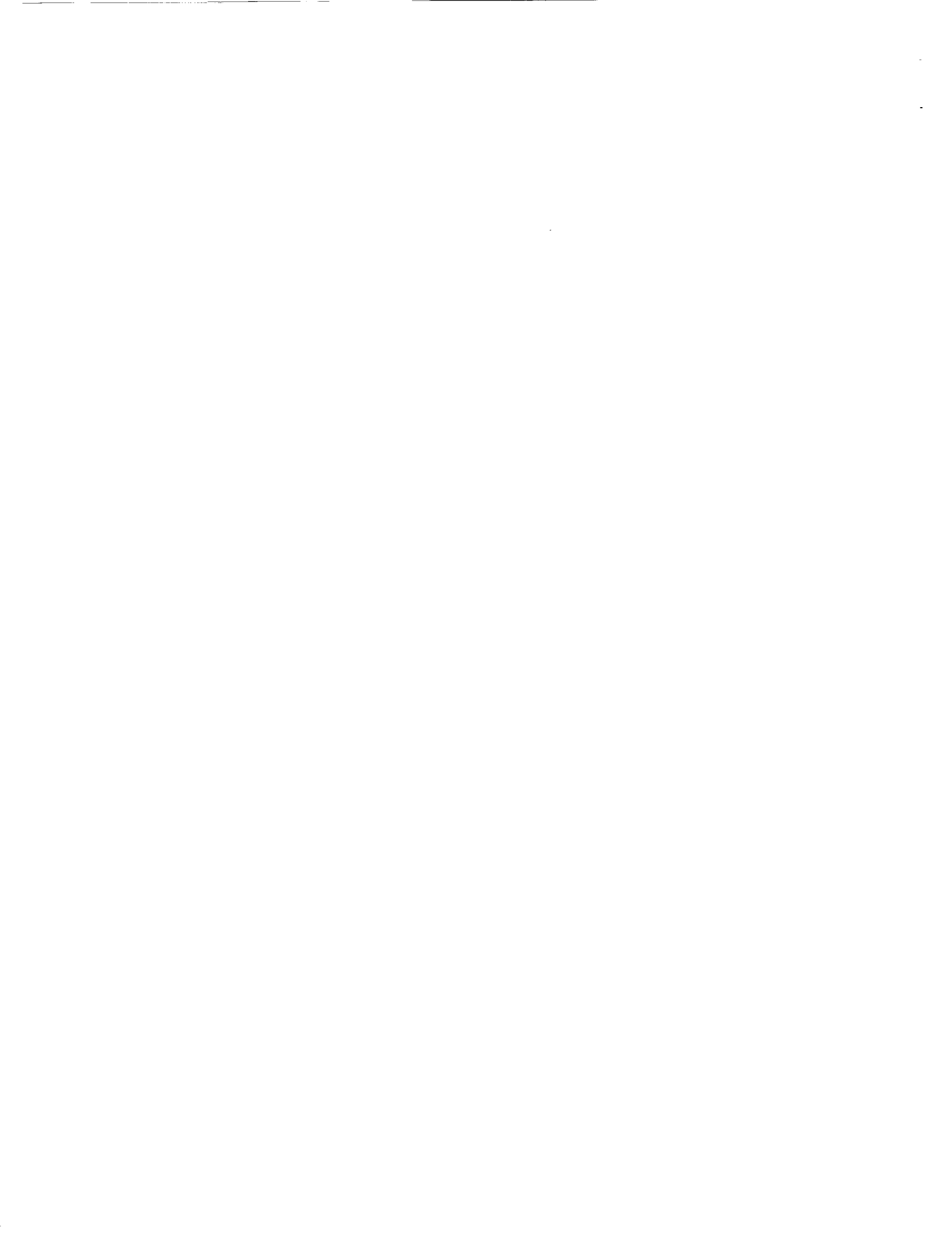


Figure 6. Phase fluctuation standard deviation (SD) dependence on medium parameters. Frequency is 1.12 GHz, $\epsilon_s = (39.917 + i16.25678)\epsilon_0$, $R_r = 0.0$ m, and $\epsilon_2 = (6.0 + i0.6)\epsilon_0$. Solid line: $l = 5.2$ mm, $f = 1.67\%$, $\epsilon_{eff} = (1.0505 + i0.001794)\epsilon_0$; short dashed line: $l = 7.2$ mm, $f = 1.67\%$, $\epsilon_{eff} = (1.0516 + i0.002417)\epsilon_0$; long dashed line: $l = 5.2$ mm, $f = 4.17\%$, $\epsilon_{eff} = (1.1360 + i0.005478)\epsilon_0$.

In Fig. 6, the dependence of the phase fluctuation standard deviation on the medium parameters of correlation length and fractional volume of scatterers is illustrated. For this case, the permittivity of Region 2 is set to approximately that of the earth at 1.12 GHz, $\epsilon_2 = (6.0 + i0.6)\epsilon_0$, and the receiver is directly below the random medium. When the correlation length is increased (solid line versus short dashed line), the phase fluctuation standard deviation also increases, which is due to the fact that the scatterers are larger and thus cause more scattering. When the fractional volume of scatterers is increased (solid line versus long dashed line), the phase fluctuation standard deviation also increases. This is because increasing the fractional volume increases the number of scatterers, and this also causes more scattering to occur.

Figure 7 shows the dependence of the phase fluctuation standard deviation on the permittivity of the ground layer. The results show that for a given medium thickness, the phase fluctuations increase when the ground layer permittivity increases. This is because increasing the ground layer permittivity increases the reflectivity of the lower boundary, which reflects more of the incident energy back into the medium to be scattered. This increased scattering will in turn increase the phase fluctuation of the received field.



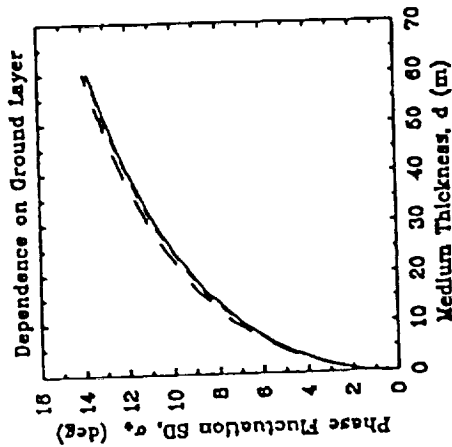


Figure 7. Phase fluctuation standard deviation (SD) dependence on ground layer permittivity. Frequency is 1.12 GHz, $\epsilon_s = (39.917 + i16.25678)\epsilon_0$, $l = 5.2$ mm, $f = 1.67\%$, $R_r = 0.0$ m, and $\epsilon_e/f = (1.0505 + i0.001794)\epsilon_0$. Solid line: $\epsilon_2 = (6.0 + i0.6)\epsilon_0$; short dashed line: $\epsilon_2 = (10.0 + i1.0)\epsilon_0$; long dashed line: $\epsilon_2 = (20.0 + i3.0)\epsilon_0$.

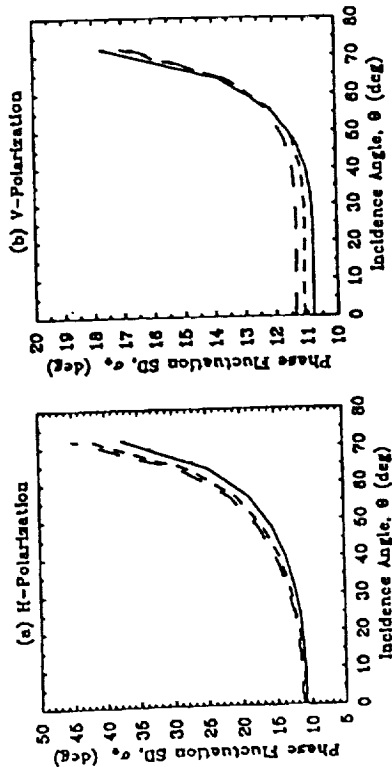


Figure 8. Phase fluctuation standard deviation (SD) dependence on incidence angle. Frequency is 1.12 GHz, $\epsilon_s = (39.917 + i16.25678)\epsilon_0$, $l = 5.2$ mm, $f = 1.67\%$, $R_r = 0.0$ m, $d = 30.0$ m, and $\epsilon_e/f = (1.0505 + i0.001794)\epsilon_0$. Solid line: $\epsilon_2 = (6.0 + i0.6)\epsilon_0$; short dashed line: $\epsilon_2 = (20.0 + i3.0)\epsilon_0$; long dashed line: $\epsilon_2 = (40.0 + i20.0)\epsilon_0$. (a) H-Polarization. (b) V-Polarization.

Figure 8a shows the phase fluctuation standard deviation dependence on incidence angle for H-Polarization. The figure shows the results for three values of ground layer permittivity. As explained above, when the ground layer permittivity increases for a particular incidence angle, the phase fluctuation standard deviation increases. For all three cases, when the incidence angle increases, the phase fluctuation standard deviation increases. This is partly due to the fact that for greater angles of incidence, the waves propagate through more of the random medium, which increases the amount of scattering. For larger angles of incidence, however, the dominant effect is that for H-Polarization, the reflectivity of the lower boundary is increasing monotonically with increasing incidence angle. As explained previously, if the reflectivity of the lower boundary is increased, more of the incident energy will be reflected back into the medium to be scattered, which increases the phase fluctuations of the received field.

Figure 8b shows the phase fluctuation standard deviation dependence on incidence angle for V-Polarization. The medium parameters and receiver location are the same for this case as for the previous case. Again, the same effect of the ground layer on the phase fluctuation standard deviation is demonstrated in this case as in the previous case, for most angles of incidence. When the incidence angle becomes relatively large, however, the curves cross. Another interesting effect is that the phase fluctuation standard deviation decreases slightly when the incidence angle increases from zero to around 45 degrees. These two effects lead to the conclusion that the reflectivity of the lower boundary, which exhibits a Brewster angle effect for V-Polarization, is again affecting the phase fluctuations. For V-Polarization, when the incidence angle increases, the reflectivity of the lower boundary decreases, drops to a minimum, then increases. This will cause the amount of incident energy reflected back into the random medium to first decrease, go to a minimum, then increase as incidence angle is increased. This explains why the phase fluctuation standard deviation decreases slightly, because less energy is reflected back into the random medium to be scattered. The reason the curves cross can be explained by the fact that the Brewster angle increases for increasing ground layer permittivity. Therefore, the ground layer with the smallest permittivity (solid line) has the smallest Brewster angle, so this curve should reach its minimum and begin increasing before the other curves. Conversely, the ground layer with the largest permittivity (long dashed line) has the largest Brewster angle, so it reaches its minimum and begins to increase after the other curves.

VI. SUMMARY

The variance of the phase fluctuations that an electromagnetic wave undergoes as it propagates through a random medium has been calculated and studied in this paper. This is one of the quantities needed to determine the SAR pattern distortion due to foliage. The other quantity needed is the covariance or autocorrelation of the phase fluctuations, which is calculated in another paper [27]. The effects studied here were the dependence of the variance of the phase fluctuations



on receiver location in lossy and lossless regions, medium thickness, correlation length and fractional volume of scatterers, depolarization of the incident wave, ground layer permittivity, and incidence angle for H- and V-Polarization. The results have been verified by comparing theoretical results obtained using different approaches.

APPENDIX A

The two-layer dyadic Green's function is specified as $\overline{\overline{G}}_{21}(\overline{r}, \overline{r}_1)$, where the subscript l denotes the region of the observation point \overline{r} and the subscript j denotes the region of the source point \overline{r}_1 . For this study, the observation region (region where the receiver is located) is Region 2, and the source region (region of the scatterers) is Region 1. Therefore, the appropriate Green's function is $\overline{\overline{G}}_{21}$, and is given by (from [1])

$$\overline{\overline{G}}_{21}(\overline{r}, \overline{r}_1) = \frac{i}{8\pi^2} \iint_{-\infty}^{+\infty} d^2k_{1\perp} \frac{e^{i\mathbf{k}_{1\perp} \cdot (\overline{r}_1 - \overline{r}_{1\perp})} e^{-ik_{2z}(z+d)} e^{ik_{1z}z}}{k_{1z}} \times \left\{ \frac{T_{12}^{\text{TE}}(k_{1\perp})}{D_2(k_{1\perp})} \hat{h}(k_{2z}) \left[R_{10}^{\text{TE}}(k_{1\perp}) \hat{h}(k_{1z}) e^{-ik_{1z}z_1} + \hat{h}(-k_{1z}) e^{ik_{1z}z_1} \right] \right. \\ \left. + \frac{k_{eff} T_{12}^{\text{TM}}(k_{1\perp})}{k_2 F_2(k_{1\perp})} \hat{v}(-k_{2z}) \left[R_{10}^{\text{TM}}(k_{1\perp}) \hat{v}(k_{1z}) e^{-ik_{1z}z_1} + \hat{v}(-k_{1z}) e^{ik_{1z}z_1} \right] \right\} \quad (82)$$

where

$$D_2(k_{1\perp}) = 1 + R_{01}^{\text{TE}} R_{12}^{\text{TE}} e^{i2k_{1z}d}, \quad F_2(k_{1\perp}) = 1 + R_{01}^{\text{TM}} R_{12}^{\text{TM}} e^{i2k_{1z}d} \quad (83)$$

$$R_{l(l+1)}^{\text{TE}} = \frac{1 - p_{l(l+1)}^{\text{TE}}}{1 + p_{l(l+1)}^{\text{TE}}}, \quad R_{l(l+1)}^{\text{TM}} = \frac{1 - p_{l(l+1)}^{\text{TM}}}{1 + p_{l(l+1)}^{\text{TM}}} \quad (84)$$

$$p_{l(l+1)}^{\text{TE}} = \frac{\mu_l k_{l(l+1)z}}{\mu_{(l+1)} k_{lz}}, \quad p_{l(l+1)}^{\text{TM}} = \frac{\epsilon_l k_{l(l+1)z}}{\epsilon_{(l+1)} k_{lz}} \quad (85)$$

$$T_{l(l+1)}^{\text{TE,TM}} = R_{l(l+1)}^{\text{TE,TM}} + 1 \quad (86)$$

$$k_{1z} = \sqrt{\epsilon_{eff}^2 - k_{1z}^2 - k_{1y}^2}, \quad k_{2z} = \sqrt{k_2^2 - k_{1z}^2 - k_{1y}^2} \quad (87)$$

The effective permittivity of the random medium is denoted by k_{eff} . The subscripts of k_{1z} and k_{2z} associate the z -directed wavenumbers with Regions 1 and 2, respectively (see Fig. 2).

The unit vectors \hat{h} and \hat{v} correspond to Transverse Electric polarization (TE, which is horizontal polarization) or Transverse Magnetic polarization (TM, which is vertical polarization), respectively. The unit vector \hat{h} is defined to be

$$\hat{h}(k_{jz}) = \frac{\hat{z} \times \mathbf{k}_j}{|\hat{z} \times \mathbf{k}_j|} = \frac{k_x \hat{y} - k_y \hat{x}}{\sqrt{k_x^2 + k_y^2}} \quad (88)$$

and the unit vector \hat{v} is defined to be

$$\hat{v}(k_{jz}) = \frac{\overline{\mathbf{k}}_j \times \hat{h}(k_{jz})}{k_j} = \frac{-k_{jz}(\hat{x}k_x + \hat{y}k_y)}{k_j \sqrt{k_x^2 + k_y^2}} + \hat{z} \frac{\sqrt{k_x^2 + k_y^2}}{k_j} \quad (89)$$

where k_{jz} corresponds to the z -directed wavenumber in Region j . Note that $(\hat{h}, \hat{v}, \hat{z})$ forms a right-handed coordinate system.

APPENDIX B

$\langle \Phi_h(\overline{r}_a) \Phi_h^*(\overline{r}_a) \rangle$

The coefficients A through H for $\langle \Phi_h(\overline{r}_a) \Phi_h^*(\overline{r}_a) \rangle$ are

$$A = \frac{T_{12}^{\text{TE}}(k_{1\perp})}{D_2(k_{1\perp})} \text{HH}_{22}^2(k_{1\perp}) R_{10}^{\text{TE}}(k_{1\perp}) \quad (90)$$

$$B = \frac{T_{12}^{\text{TE}}(k_{1\perp})}{D_2(k_{1\perp})} \text{HH}_{22}^2(k_{1\perp}) \quad (91)$$

$$C = \frac{k_{eff} T_{12}^{\text{TM}}(k_{1\perp})}{k_2 F_2(k_{1\perp})} \text{HV}_{22}(k_{1\perp}) \text{VH}_{11}(k_{1\perp}) R_{10}^{\text{TM}}(k_{1\perp}) \quad (92)$$

$$D = \frac{k_{eff} T_{12}^{\text{TM}}(k_{1\perp})}{k_2 F_2(k_{1\perp})} \text{HV}_{22}(k_{1\perp}) \text{VH}_{11}(k_{1\perp}) \quad (93)$$

$$E = \frac{T_{12}^{\text{TE}}(k_{2\perp})}{D_2^*(k_{2\perp})} (\text{HH}_{22}^*(k_{2\perp}))^2 R_{10}^{\text{TE}*}(k_{2\perp}) \quad (94)$$

$$F = \frac{T_{12}^{\text{TE}}(k_{2\perp})}{D_2^*(k_{2\perp})} (\text{HH}_{22}^*(k_{2\perp}))^2 \quad (95)$$

$$G = \frac{k_{eff}^* T_{12}^{\text{TM}*}(k_{2\perp})}{k_2^* F_2^*(k_{2\perp})} \text{HV}_{22}^*(k_{2\perp}) \text{VH}_{11}^*(k_{2\perp}) R_{10}^{\text{TM}*}(k_{2\perp}) \quad (96)$$

$$H = \frac{k_{eff}^* T_{12}^{\text{TM}*}(k_{2\perp})}{k_2^* F_2^*(k_{2\perp})} \text{HV}_{22}^*(k_{2\perp}) \text{VH}_{11}^*(k_{2\perp}) \quad (97)$$

The \square coefficients for $\langle \Phi_h(\overline{r}_a) \Phi_h^*(\overline{r}_a) \rangle$ are

$$\square_{(-1,-1,-1,-1)} = (BF - BH - DF + DH) A_1 A_1^* \quad (98)$$

$$\square_{(-1,-1,-1,+1)} = (BF - BH - DF + DH) A_1 B_1^* \quad (99)$$

$$\square_{(-1,-1,+1,-1)} = (BE + BG - DE - DG) A_1 A_1^* \quad (100)$$

$$\square_{(-1,-1,+1,+1)} = (BE + BG - DE - DG) A_1 B_1^* \quad (101)$$

$$\square_{(-1,+1,-1,-1)} = (BF - BH - DF + DH) B_1 A_1^* \quad (102)$$

$$\square_{(-1,+1,-1,+1)} = (BF - BH - DF + DH) B_1 B_1^* \quad (103)$$

$$\square_{(-1,+1,+1,-1)} = (BE + BG - DE - DG) B_1 A_1^* \quad (104)$$

$$\square_{(-1,+1,+1,+1)} = (BE + BG - DE - DG) B_1 B_1^* \quad (105)$$



$$\begin{aligned}
 \square_{(+1,-1,-1,-1)} &= (AF - AH + CF - CH) A_1 A_1^* & (106) \\
 \square_{(+1,-1,-1,+1)} &= (AF - AH + CF - CH) A_1 B_1^* & (107) \\
 \square_{(+1,-1,+1,-1)} &= (AE + AG + CE + CG) A_1 A_1^* & (108) \\
 \square_{(+1,-1,+1,+1)} &= (AE + AG + CE + CG) A_1 B_1^* & (109) \\
 \square_{(+1,+1,-1,-1)} &= (AF - AH + CF - CH) B_1 A_1^* & (110) \\
 \square_{(+1,+1,-1,+1)} &= (AF - AH + CF - CH) B_1 B_1^* & (111) \\
 \square_{(+1,+1,+1,-1)} &= (AE + AG + CE + CG) B_1 A_1^* & (112) \\
 \square_{(+1,+1,+1,+1)} &= (AE + AG + CE + CG) B_1 B_1^* & (113)
 \end{aligned}$$

$(\Phi_h(\bar{\tau}_a) \Phi_h(\bar{\tau}_a))$

For $(\Phi_h(\bar{\tau}_a) \Phi_h(\bar{\tau}_a))$, the coefficients A through D are the same as those for $(\Phi_h(\bar{\tau}_a) \Phi_h^*(\bar{\tau}_a))$ (90)-(93), and the coefficients E through H are the complex conjugates of those in (94)-(97).

The \square coefficients for $(\Phi_h(\bar{\tau}_a) \Phi_h(\bar{\tau}_a))$ are

$$\begin{aligned}
 \square_{(-1,-1,-1,-1)} &= (BE + BG - DE - DG) A_1 B_1 & (114) \\
 \square_{(-1,-1,-1,+1)} &= (BE + BG - DE - DG) A_1 A_1 & (115) \\
 \square_{(-1,-1,+1,-1)} &= (BF - BH - DF + DH) A_1 B_1 & (116) \\
 \square_{(-1,-1,+1,+1)} &= (BF - BH - DF + DH) A_1 A_1 & (117) \\
 \square_{(-1,+1,-1,-1)} &= (BE + BG - DE - DG) B_1 B_1 & (118) \\
 \square_{(-1,+1,-1,+1)} &= (BE + BG - DE - DG) B_1 A_1 & (119) \\
 \square_{(-1,+1,+1,-1)} &= (BF - BH - DF + DH) B_1 B_1 & (120) \\
 \square_{(-1,+1,+1,+1)} &= (BF - BH - DF + DH) B_1 A_1 & (121) \\
 \square_{(+1,-1,-1,-1)} &= (AE + AG + CE + CG) A_1 B_1 & (122) \\
 \square_{(+1,-1,-1,+1)} &= (AE + AG + CE + CG) A_1 A_1 & (123) \\
 \square_{(+1,-1,+1,-1)} &= (AF - AH + CF - CH) A_1 B_1 & (124) \\
 \square_{(+1,-1,+1,+1)} &= (AF - AH + CF - CH) A_1 A_1 & (125) \\
 \square_{(+1,+1,-1,-1)} &= (AE + AG + CE + CG) B_1 B_1 & (126) \\
 \square_{(+1,+1,-1,+1)} &= (AE + AG + CE + CG) B_1 A_1 & (127) \\
 \square_{(+1,+1,+1,-1)} &= (AF - AH + CF - CH) B_1 B_1 & (128) \\
 \square_{(+1,+1,+1,+1)} &= (AF - AH + CF - CH) B_1 A_1 & (129)
 \end{aligned}$$

$(\Phi_v(\bar{\tau}_a) \Phi_v^*(\bar{\tau}_a))$

The \square coefficients for $(\Phi_v(\bar{\tau}_a) \Phi_v^*(\bar{\tau}_a))$ are

$$\square_{(-1,-1,-1,-1)} = (\bar{B} \cdot \bar{A}_1 + \bar{D} \cdot \bar{A}_1) (\bar{F} \cdot \bar{A}_1 + \bar{H} \cdot \bar{A}_1) \quad (130)$$

$$\begin{aligned}
 \square_{(-1,-1,-1,+1)} &= (\bar{B} \cdot \bar{A}_1 + \bar{D} \cdot \bar{A}_1) (\bar{F} \cdot \bar{B}_1 + \bar{H} \cdot \bar{B}_1) & (131) \\
 \square_{(-1,-1,+1,-1)} &= (\bar{B} \cdot \bar{A}_1 + \bar{D} \cdot \bar{A}_1) (\bar{E} \cdot \bar{A}_1 + \bar{G} \cdot \bar{A}_1) & (132) \\
 \square_{(-1,-1,+1,+1)} &= (\bar{B} \cdot \bar{A}_1 + \bar{D} \cdot \bar{A}_1) (\bar{E} \cdot \bar{B}_1 + \bar{G} \cdot \bar{B}_1) & (133) \\
 \square_{(-1,+1,-1,-1)} &= (\bar{B} \cdot \bar{B}_1 + \bar{D} \cdot \bar{B}_1) (\bar{F} \cdot \bar{A}_1 + \bar{H} \cdot \bar{A}_1) & (134) \\
 \square_{(-1,+1,-1,+1)} &= (\bar{B} \cdot \bar{B}_1 + \bar{D} \cdot \bar{B}_1) (\bar{F} \cdot \bar{B}_1 + \bar{H} \cdot \bar{B}_1) & (135) \\
 \square_{(-1,+1,+1,-1)} &= (\bar{B} \cdot \bar{B}_1 + \bar{D} \cdot \bar{B}_1) (\bar{E} \cdot \bar{A}_1 + \bar{G} \cdot \bar{A}_1) & (136) \\
 \square_{(-1,+1,+1,+1)} &= (\bar{B} \cdot \bar{B}_1 + \bar{D} \cdot \bar{B}_1) (\bar{E} \cdot \bar{B}_1 + \bar{G} \cdot \bar{B}_1) & (137) \\
 \square_{(+1,-1,-1,-1)} &= (\bar{A} \cdot \bar{A}_1 + \bar{C} \cdot \bar{A}_1) (\bar{F} \cdot \bar{A}_1 + \bar{H} \cdot \bar{A}_1) & (138) \\
 \square_{(+1,-1,-1,+1)} &= (\bar{A} \cdot \bar{A}_1 + \bar{C} \cdot \bar{A}_1) (\bar{F} \cdot \bar{B}_1 + \bar{H} \cdot \bar{B}_1) & (139) \\
 \square_{(+1,-1,+1,-1)} &= (\bar{A} \cdot \bar{A}_1 + \bar{C} \cdot \bar{A}_1) (\bar{E} \cdot \bar{A}_1 + \bar{G} \cdot \bar{A}_1) & (140) \\
 \square_{(+1,-1,+1,+1)} &= (\bar{A} \cdot \bar{A}_1 + \bar{C} \cdot \bar{A}_1) (\bar{E} \cdot \bar{B}_1 + \bar{G} \cdot \bar{B}_1) & (141) \\
 \square_{(+1,+1,-1,-1)} &= (\bar{A} \cdot \bar{B}_1 + \bar{C} \cdot \bar{B}_1) (\bar{F} \cdot \bar{A}_1 + \bar{H} \cdot \bar{A}_1) & (142) \\
 \square_{(+1,+1,-1,+1)} &= (\bar{A} \cdot \bar{B}_1 + \bar{C} \cdot \bar{B}_1) (\bar{F} \cdot \bar{B}_1 + \bar{H} \cdot \bar{B}_1) & (143) \\
 \square_{(+1,+1,+1,-1)} &= (\bar{A} \cdot \bar{B}_1 + \bar{C} \cdot \bar{B}_1) (\bar{E} \cdot \bar{A}_1 + \bar{G} \cdot \bar{A}_1) & (144) \\
 \square_{(+1,+1,+1,+1)} &= (\bar{A} \cdot \bar{B}_1 + \bar{C} \cdot \bar{B}_1) (\bar{E} \cdot \bar{B}_1 + \bar{G} \cdot \bar{B}_1) & (145)
 \end{aligned}$$

where

$$\begin{aligned}
 \bar{A} &= \frac{T_{12}^{TE}(k_{1\perp})}{D_2(k_{1\perp})} V_{H22}(k_{1\perp}) R_{10}^{TE}(k_{1\perp}) \hat{h}(k_{1z}^{(1)}) & (146) \\
 \bar{B} &= \frac{T_{12}^{TE}(k_{1\perp})}{D_2(k_{1\perp})} V_{H22}(k_{1\perp}) \hat{h}(-k_{1z}^{(1)}) & (147) \\
 \bar{C} &= \frac{k_{eff} T_{12}^{TM}(k_{1\perp})}{k_2 F_2(k_{1\perp})} VV_{22}(k_{1\perp}) R_{10}^{TM}(k_{1\perp}) \hat{v}(k_{1z}^{(1)}) & (148) \\
 \bar{D} &= \frac{k_{eff} T_{12}^{TM}(k_{1\perp})}{k_2 F_2(k_{1\perp})} VV_{22}(k_{1\perp}) \hat{v}(-k_{1z}^{(1)}) & (149) \\
 \bar{E} &= \frac{T_{12}^{TE^*}(k_{2\perp})}{D_2^*(k_{2\perp})} V_{H22}(k_{2\perp}) R_{10}^{TE^*}(k_{2\perp}) \hat{h}^*(k_{1z}^{(2)}) & (150) \\
 \bar{F} &= \frac{T_{12}^{TE^*}(k_{2\perp})}{D_2^*(k_{2\perp})} V_{H22}(k_{2\perp}) \hat{h}^*(-k_{1z}^{(2)}) & (151) \\
 \bar{G} &= \frac{k_{eff}^* T_{12}^{TM^*}(k_{2\perp})}{k_2^* F_2^*(k_{2\perp})} VV_{22}^*(k_{2\perp}) R_{10}^{TM^*}(k_{2\perp}) \hat{v}^*(k_{1z}^{(2)}) & (152)
 \end{aligned}$$



$$\bar{H} = \frac{k_e^* f f_{12}^{TM^*}(k_{2L})}{k_2^* F_2^*(k_{2L})} VV_{22}^*(k_{2L}) \hat{v}^*(-k_{1z}^{(2)}) \quad (153)$$

$$\bar{B}_1 = B_1^M \hat{v}(-k_{1z;m}) \quad (154)$$

$$\bar{A}_1 = A_1^M \hat{v}(k_{1z;m}) \quad (155)$$

$(\Phi_v(\bar{r}_a) \Phi_v(\bar{r}_a))$

The \square coefficients for $(\Phi_v(\bar{r}_a) \Phi_v(\bar{r}_a))$ are

- $\square_{(-1,-1,-1,-1)} = (\bar{B} \cdot \bar{A}_1 + \bar{D} \cdot \bar{A}_1) (\bar{E} \cdot \bar{B}_1 + \bar{G} \cdot \bar{B}_1) \quad (156)$
- $\square_{(-1,-1,-1,+1)} = (\bar{B} \cdot \bar{A}_1 + \bar{D} \cdot \bar{A}_1) (\bar{E} \cdot \bar{A}_1 + \bar{G} \cdot \bar{A}_1) \quad (157)$
- $\square_{(-1,-1,+1,-1)} = (\bar{B} \cdot \bar{A}_1 + \bar{D} \cdot \bar{A}_1) (\bar{F} \cdot \bar{B}_1 + \bar{H} \cdot \bar{B}_1) \quad (158)$
- $\square_{(-1,-1,+1,+1)} = (\bar{B} \cdot \bar{A}_1 + \bar{D} \cdot \bar{A}_1) (\bar{F} \cdot \bar{A}_1 + \bar{H} \cdot \bar{A}_1) \quad (159)$
- $\square_{(-1,+1,-1,-1)} = (\bar{B} \cdot \bar{B}_1 + \bar{D} \cdot \bar{B}_1) (\bar{E} \cdot \bar{B}_1 + \bar{G} \cdot \bar{B}_1) \quad (160)$
- $\square_{(-1,+1,-1,+1)} = (\bar{B} \cdot \bar{B}_1 + \bar{D} \cdot \bar{B}_1) (\bar{E} \cdot \bar{A}_1 + \bar{G} \cdot \bar{A}_1) \quad (161)$
- $\square_{(-1,+1,+1,-1)} = (\bar{B} \cdot \bar{B}_1 + \bar{D} \cdot \bar{B}_1) (\bar{F} \cdot \bar{B}_1 + \bar{H} \cdot \bar{B}_1) \quad (162)$
- $\square_{(-1,+1,+1,+1)} = (\bar{B} \cdot \bar{B}_1 + \bar{D} \cdot \bar{B}_1) (\bar{F} \cdot \bar{A}_1 + \bar{H} \cdot \bar{A}_1) \quad (163)$
- $\square_{(+1,-1,-1,-1)} = (\bar{A} \cdot \bar{A}_1 + \bar{C} \cdot \bar{A}_1) (\bar{E} \cdot \bar{B}_1 + \bar{G} \cdot \bar{B}_1) \quad (164)$
- $\square_{(+1,-1,-1,+1)} = (\bar{A} \cdot \bar{A}_1 + \bar{C} \cdot \bar{A}_1) (\bar{E} \cdot \bar{A}_1 + \bar{G} \cdot \bar{A}_1) \quad (165)$
- $\square_{(+1,-1,+1,-1)} = (\bar{A} \cdot \bar{A}_1 + \bar{C} \cdot \bar{A}_1) (\bar{F} \cdot \bar{B}_1 + \bar{H} \cdot \bar{B}_1) \quad (166)$
- $\square_{(+1,-1,+1,+1)} = (\bar{A} \cdot \bar{A}_1 + \bar{C} \cdot \bar{A}_1) (\bar{F} \cdot \bar{A}_1 + \bar{H} \cdot \bar{A}_1) \quad (167)$
- $\square_{(+1,+1,-1,-1)} = (\bar{A} \cdot \bar{B}_1 + \bar{C} \cdot \bar{B}_1) (\bar{E} \cdot \bar{B}_1 + \bar{G} \cdot \bar{B}_1) \quad (168)$
- $\square_{(+1,+1,-1,+1)} = (\bar{A} \cdot \bar{B}_1 + \bar{C} \cdot \bar{B}_1) (\bar{E} \cdot \bar{A}_1 + \bar{G} \cdot \bar{A}_1) \quad (169)$
- $\square_{(+1,+1,+1,-1)} = (\bar{A} \cdot \bar{B}_1 + \bar{C} \cdot \bar{B}_1) (\bar{F} \cdot \bar{B}_1 + \bar{H} \cdot \bar{B}_1) \quad (170)$
- $\square_{(+1,+1,+1,+1)} = (\bar{A} \cdot \bar{B}_1 + \bar{C} \cdot \bar{B}_1) (\bar{F} \cdot \bar{A}_1 + \bar{H} \cdot \bar{A}_1) \quad (171)$

The coefficients A through D used above are defined in (146)-(149), and the coefficients E through H used above are the complex conjugates of those in (150)-(153).

ACKNOWLEDGEMENTS

This work was supported by the DARPA Contract MDA972-90-C-0021, the ARO Contract DAAL03-88-J-0057, the NASA Contract 958461, the NASA Contract NAGW-1617, and the ONR Contract N00014-89-J-1107.

This work was also sponsored by the Defense Advanced Research Projects Agency. The views expressed are those of the authors and do not reflect the official policy or position of the U. S. Government.

ACKNOWLEDGMENTS

The Editor thanks A. K. Fung and three anonymous Reviewers for reviewing the paper.

REFERENCES

1. Tsang, L., J. A. Kong, and R. T. Shin, *Theory of Microwave Remote Sensing*, Wiley-Interscience, New York, 1985.
2. Tatarski, V. I., and M. E. Gertsenshtein, "Propagation of waves in a medium with strong fluctuation of the refractive index," *Soviet Physics JETP*, Vol. 17, 458-463, 1963.
3. Lee, J., and J. A. Kong, "Electromagnetic wave scattering in a two-layer anisotropic random medium," *J. Opt. Soc. Am. A*, Vol. 2, 2171-2186, 1985.
4. Tsang, L., and J. A. Kong, "Emissivity of half-space random media," *Radio Science*, Vol. 11, 593-598, 1976.
5. Zuniga, M., T. Habashy, and J. A. Kong, "Active remote sensing of layered random media," *IEEE Transactions on Geoscience Electronics*, Vol. 17, 296-302, 1979.
6. Zuniga, M. A., J. A. Kong, and L. Tsang, "Depolarization effects in the active remote sensing of random media," *J. Appl. Phys.*, Vol. 51, No. 5, 2315-2325, May 1980.
7. Zuniga, M., and J. A. Kong, "Active remote sensing of random media," *J. Appl. Phys.*, Vol. 51, 74-79, 1980.
8. Lin, F. C., J. A. Kong, and R. T. Shin, "Theoretical models for active and passive microwave remote sensing of snow-covered sea ice," *IGARSS'87*, University of Michigan, Ann Arbor, Michigan, 18-21 May 1987.
9. Borgeaud, M., J. A. Kong, and F. C. Lin, "Microwave remote sensing of snow-covered sea ice," *Proceeding of the IGARSS'86 Symposium*, 133-138, Zürich, 8-11 Sept. 1986.
10. Borgeaud, M., R. T. Shin, and J. A. Kong, "Theoretical models for polarimetric radar clutter," *J. Electro. Waves Applic.*, Vol. 1, No. 1, 73-89, 1987.
11. Borgeaud, M., S. V. Nghiem, R. T. Shin, and J. A. Kong, "Theoretical models for polarimetric microwave remote sensing of earth terrain," *J. Electro. Waves Applic.*, Vol. 3, No. 1, 61-81, 1989.
12. Stogryn, A., "Electromagnetic scattering by random dielectric constant fluctuations in a bounded medium," *Radio Science*, Vol. 9, 509-518, 1974.
13. Fung, A., and H. Fung, "Application of first-order renormalization method to scattering from a vegetated-like half space," *IEEE Transactions on Geoscience Electronics*, Vol. 15, 189-195, 1977.
14. de Wolf, D. A., "Electromagnetic reflection from an extended turbulent medium: cumulative forward-scatter single backscatter approximation," *IEEE Trans. Antennas Propagat.*, Vol. AP-19, No. 2, 254-262, Mar. 1971.
15. Rosenbaum, S., and L. W. Bowles, "Clutter return from vegetated areas," *IEEE Trans. Antennas Propagat.*, Vol. AP-22, No. 2, 227-236, Mar. 1974.
16. Tan, H. S., A. K. Fung, and H. Eom, "A second-order renormalization theory for cross-polarized backscatter from a half space random medium," *Radio Science*, Vol. 15, No. 6, 1059-1065, Nov.-Dec. 1980.
17. Chuah, H. T., and H. S. Tan, "A high order renormalization method for radar backscatter from a random medium," *IEEE Trans. Geosci. Remote Sensing*, Vol. 27, No. 1, 79-85, Jan. 1989.
18. Tsang, L., and J. A. Kong, "Application of strong fluctuation random medium theory to scattering from vegetation-like half space," *IEEE Trans. Geosci. Remote Sensing*, Vol. GE-19, No. 1, 62-69, Jan. 1981.

19. Nghiem, S. V., F. C. Lin, J. A. Kong, R. T. Shin, and H. A. Yueh, "Three-layer random medium model for fully polarimetric remote sensing of geophysical media," *Digest of the Progress in Electromagnetics Research Symposium*, 267, Boston, Massachusetts, July 1989.
 20. Tsang, L., J. A. Kong, R. W. Newton, "Application of strong fluctuation random medium theory to scattering of electromagnetic waves from a half-space of dielectric mixture," *IEEE Trans. Antennas Propagat.*, Vol. AP-30, No. 2, Mar. 1982.
 21. Tsang, L., and J. A. Kong, "Scattering of electromagnetic waves from random media with strong permittivity fluctuations," *Radio Science*, Vol. 16, No. 3, 303-320, May-June 1981.
 22. Ryzhov, Y. A., V. V. Tamoikin, and V. I. Tatarskii, "Spatial dispersion of inhomogeneous media," *Soviet Physics JETP*, Vol. 21, 433-438, 1965.
 23. Ryzhov, Y. A., and V. V. Tamoikin, "Radiation and propagation of electromagnetic waves in randomly inhomogeneous media," *Radiophys. Quantum Electron.*, Vol. 13 (trans. from Russian), 273-300, 1970.
 24. Tamoikin, V. V., "The average field in a medium having strong anisotropic inhomogeneities," *Radiophys. Quantum Electron.*, Vol. 14 (trans. from Russian), 228-233, 1971.
 25. Kong, J. A., *Electromagnetic Wave Theory*. New York: Wiley-Interscience, 1986.
 26. Chu, N. C., "Phase Fluctuations of Waves Propagating Through a Random Medium," S.M. Thesis, Massachusetts Institute of Technology, June 1990.
 27. Chu, N. C., J. A. Kong, H. A. Yueh, S. V. Nghiem, J. G. Fleischman, S. Ayasli, and R. T. Shin, "Covariance of phase fluctuations of waves propagating through a random medium," submitted for publication, 1990.
- Nelson C. Chu received the B.S. degree in electrical engineering from the Virginia Polytechnic Institute and State University in 1988. Since 1988 he has been with the Department of Electrical Engineering at the Massachusetts Institute of Technology as a graduate student, and a Research Assistant at the MIT Lincoln Laboratory. He received his S.M. degree from MIT in 1990.
- Jin A. Kong is Professor of Electrical Engineering and Chairman of Area IV on Energy and Electromagnetic Systems in the Department of Electrical Engineering and Computer Science at the Massachusetts Institute of Technology in Cambridge, Massachusetts. His research interest is in the field of electromagnetic wave theory and applications. He has published seven books and over 300 refereed journal and conference papers, and is the Editor of the Wiley Series in Remote Sensing, and Chief Editor of the Elsevier book series of Progress In Electromagnetics Research (PIER).
- Simon H. Yueh received the SB (1982) and SM (1984) from the Electrical Engineering Department of National Taiwan University, Taiwan, and is currently working on the Ph.D. degree in Electrical Engineering at Massachusetts Institute of Technology, Cambridge. His fields of interest are electromagnetic field theory and remote sensing.
- Son V. Nghiem received his B.S. degree (1985) in electrical engineering with Summa Cum Laude Honor from Texas A & M University and his M.S. degree (1988) in electrical engineering and computer science from the Massachusetts Institute of Technology. He is currently working toward his Ph.D. degree and his research interest encompasses electromagnetic wave theory, polarimetric remote sensing, and atmospheric and ionospheric effects on wave propagation. Mr. Nghiem is a member of the IEEE and the Honor Society of Phi Kappa Phi.
- Jack G. Fleischman received the Ph.D. degree in physics from the University of Pennsylvania in 1987. His dissertation was in the field of elementary particle physics. Since 1988 he has been a member of the Research Staff in the Systems and Analysis Group at the MIT Lincoln Laboratory. His research activities include polarimetric remote sensing, electromagnetic propagation and systems analysis. Dr. Fleischman is a member of the American Physical Society, Sigma Pi Sigma and the New York Academy of Sciences.
- Serpil Ayasli received the B.S. degree in electrical engineering, and the M.S. and Ph.D. degrees in physics, all from the Middle East Technical University, Ankara, Turkey, in 1973, 1975, and 1978, respectively. From 1975 to 1979 she was a member of the teaching staff at the Department of Physics, Middle East Technical University. In 1979 she started working as a Postdoctoral Fellow at the Center for Theoretical Physics and the Center for Space Research, Massachusetts Institute of Technology, where she pursued research on theoretical modeling of astronomical X-ray burst sources until 1982. Since 1982 she has been with the MIT Lincoln Laboratory. Her current research activities include terrain-specific radar propagation and clutter modeling, radar cross-section evaluation, and ground-based radar performance predictions.
- Robert T. Shin received his SB (1977), SM (1980), and Ph.D. (1984) in Electrical Engineering from the Massachusetts Institute of Technology. Since 1984 he has been on the Research Staff in the Air Defense Techniques Group at the MIT Lincoln Laboratory. His research interest is in the areas of electromagnetic wave scattering and propagation and theoretical model development and data interpretation for microwave remote sensing. He is the coauthor of *Theory of Microwave Remote Sensing* (Wiley, 1985). Dr. Shin is a member of the IEEE, American Geophysical Union, Tau Beta Pi, Eta Kappa Nu, and commission F of the International Union of Radio Science.

THEORETICAL MODELING FOR PASSIVE MICROWAVE REMOTE SENSING OF EARTH TERRAIN

by

J. A. Kong

Center for Electromagnetic Theory and Applications
Research Laboratory of Electronics and
Department of Electrical Engineering and Computer Science
Massachusetts Institute of Technology
Cambridge, Massachusetts 02139, USA

TEL: 617-253-5625

FAX: 617-253-0987

Abstract

In this paper we address the issue of theoretical modeling for passive microwave remote sensing of terrain media such as snow, ice, vegetation, and periodic surfaces. Historically, the volume scattering effects stimulated the development of the continuous random medium model and the random discrete scattering model for the description of the media. Theoretical treatments were developed along two different paths. Invoking the principle of reciprocity, the wave theory based on Maxwell's equations has been used to calculate the emissivity. The other approach was to start with the radiative transfer equations and solved for the brightness temperatures directly. Attempts have been made to derive the radiative transfer theory from the wave theory. At the same time, both theoretical approaches have been used to calculate the radiometric emissions and to interpret experimentally measured data.

The successful interpretation of the Cosmos 243 data was perhaps the first most important step towards a serious development of the continuous random medium model to account for the volume scattering effects of snow ice fields. Subsequent interpretation of measurement results from snow field with both passive radiometers and active radar systems established a unique position for its description of earth terrain media. Recent efforts in classifying sea ice with correlation function characterization are demonstration of acceptance of this model. Future inverse scattering developments will perhaps rely heavily on this model.

In this paper, we shall illustrate the development of the theoretical models and present data matching results with measurements made in snow ice fields and vegetation canopies. The emissivity calculations for periodical rough surfaces will also be presented and compared to measured data.

Recent development in polarimetric active remote sensing with synthetic aperture radar has created significant theoretical results and practical applications. In passive remote sensing, the third and the fourth Stokes parameters for earth remote sensing have not received much attention in the past partly due to the expected small values any measurement can yield. We have made initial calculations and experimental measurements to show that at least the third Stokes parameter can give appreciable number in both theoretical prediction and actual experimentation in a plowed field. Such results may have practical implications in measuring wind directions in ocean waves, for instance. We believe polarimetric passive remote sensing is a viable field which should be explored in light of its potential applications that may derived from the full Stokes vector instead of its first two parameters, i.e., the horizontally and vertically polarized brightness temperature components.

Acknowledgement: The work presented in this paper contains contributions from L. Tsang, R. Shin, S. Nghiem, H. Yueh, J. Lee, M. Borgeaud, K. O'Neill, M. Veysoglu, H. Han, C. Hsu, and others.

Polarimetric Signatures of a Canopy of Dielectric Cylinders
Based on First and Second Order Vector Radiative
Transfer Theory

L. Tsang and C. H. Chan

Electromagnetics and Remote Sensing Laboratory
Department of Electrical Engineering
University of Washington
Seattle, WA 98195, USA

J. A. Kong

Department of Electrical Engineering and Computer Science
Massachusetts Institute of Technology
Cambridge, MA 02139, USA

J. Joseph

General Electric Corporate Research and Development
Schenectady, NY 12301, USA

Abstract—Complete polarimetric signatures of a canopy of dielectric cylinders overlying a homogeneous half space are studied with the first and second order solutions of the vector radiative transfer theory. The vector radiative transfer equations contain a general nondiagonal extinction matrix and a phase matrix. The energy conservation issue is addressed by calculating the elements of the extinction matrix and the elements of the phase matrix in a manner that is consistent with energy conservation. Two methods are used. In the first method, the surface fields and the internal fields of the dielectric cylinder are calculated by using the fields of an infinite cylinder. The phase matrix is calculated and the extinction matrix is calculated by summing the absorption and scattering to ensure energy conservation. In the second method, the method of moments is used to calculate the elements of the extinction and phase matrices. The Mueller matrix based on the first order and second order multiple scattering solutions of the vector radiative transfer equation are calculated. Results from the two methods are compared. The vector radiative transfer equations, combined with the solution based on method of moments, obey both energy conservation and reciprocity. The polarimetric signatures, copolarized and depolarized return, degree of polarization, and phase differences are studied as a function of the orientation, sizes, and dielectric properties of the cylinders. It is shown that second order scattering is generally important for vegetation canopy at C band and can be important at L band for some cases.

I. INTRODUCTION

Recently, there has been growing interest in polarimetric microwave remote sensing of geophysical terrain [1-5]. Some of the prominent features in terrain signatures [6-8] are a pedestal in copolarized return and in depolarized return, a

N93 - 13088

88001-66A



hibition of partial polarization with a degree of polarization less than unity on averaging the return signals, and a polarization phase difference between uv and vh waves. The theoretical models of volume scattering that have been studied include the random medium model [9], Rayleigh spherical scatterers [10], simple scattering models [6], small spheroidal scatterers [11], dense medium model [11,12], finite cylinder and discs scattering models [13], and multiple scattering solution [11,14].

Theoretically, the polarimetric signatures of geophysical terrain can be represented by the Mueller matrix. A very common method of calculating the Mueller matrix is through the vector radiative transfer equation [2] governing the propagation and scattering of the four Stokes parameters in a medium containing a random distribution of scatterers. Solutions of the vector radiative transfer theory include the first order solution, the second order solution [11,15], and the full multiple scattering solution for small spherical and non-spherical scatterers [11,14]. It has been shown that the vector radiative transfer equation obeys energy conservation if the scattering amplitude functions used are that of the exact solution of Maxwell's equations for that particular type of scatterers (e.g. Mic scattering by spheres) [2,11]. For the case when approximate expressions are used for the scattering amplitudes, it has been pointed out that care must be exercised in calculating the elements of the extinction matrix and the elements of the phase matrix in a manner that is consistent with energy conservation [11]. The problem of energy conservation is particularly important for multiple scattering problems when violation of energy conservation can lead to nonphysical results. (Note: imagine what will happen if albedo is larger than unity). For the case of scattering by finite cylinders, a common model of approximation was based on the surface field or the internal field of an infinite cylinder to calculate the extinction matrix and the phase matrix. In those cases, however the issue of energy conservation for scattering by a cylinder of finite length has not been addressed [13,16-18]. Conservation of energy in scattering by a single particle is the classical subject of the forward scattering theorem [19,20]. In a medium consisting of a random distribution of many particles with a certain orientation distribution, the situation is different as characteristic waves exist with characteristic polarizations as dictated by Foldy's approximation and the extinction matrix of transfer theory [2,11]. Extinction is described by extinction rates of these characteristic waves. The energy conservation of the extinction matrix, emission vector, and phase matrix of the vector radiative transfer theory is shown to be obeyed if exact scattering amplitudes of the particle is used [2,11]. Reciprocity is also obeyed in vector radiative transfer theory if the exact scattering amplitudes are used [2,11]. On the other hand, the use of the infinite cylinder approximation [16-18] does not give reciprocal bistatic scattering amplitudes. Single scattering by a forest canopy overlying the ground makes use of bistatic scattering amplitudes of the particle in addition to monostatic scattering amplitudes as the wave can be scattered by the particle and then reflected by the ground before reaching the receiver. Thus using the infinite cylinder approximation in scattering by a vegetation canopy overlying the ground can give different results for HV and VH return.

In this paper, we study the complete polarimetric signatures of a canopy of dielectric cylinders overlying a homogeneous half space with the first and second order solutions of the vector radiative transfer theory. The energy conservation issue is addressed by calculating the elements of the extinction matrix and the elements of the phase matrix in a manner that is consistent with energy conservation. Two methods are used. In the first method, the surface fields and the internal fields of the dielectric cylinder are calculated by using the fields of an infinite cylinder [4]. We calculate the extinction matrix, however, by summing the absorption and scattering to ensure energy conservation. In the second method, the method of moments [21-22], which is a numerical solution of Maxwell's equations, is used to calculate the elements of the extinction and phase matrices. Results of the computed Mueller matrices from the two methods are tabulated and compared. The CPU for the two methods and for first and second order solutions of the transfer theory are compared and discussed. The computation based on method of moments is not formidable compared with the infinite cylinder approach because much of the CPU in transfer theory is consumed on averaging over orientations and integration over directions in second order theory. The polarimetric signatures, copolarized and depolarized return, degree of polarization, and phase differences are studied as a function of the orientation, sizes, and dielectric properties of the cylinders using parameters of vegetation canopy overlying the ground [23-25]. Salient features of the numerical results are as follows. (1) The infinite cylinder approximation gives reasonable approximations for cylinders of small radius and deviate from MOM for larger radius. (2) The infinite cylinder approximation also violates reciprocity and can give significantly different results for HV and VH returns, particularly for problems of larger radius. (3) In scattering by vegetation canopy, second order scattering effects can become important for frequencies around C -band and higher. For some medium parameters, second order scattering can also be important at L -band.

The numerical computation in this paper is intensive. However, it can be used to provide training data for neural network which can be used for speedy inversion of parameters from remote sensing data [26]. Polarimetric sensing utilizing complete Mueller matrix is an important remote sensing tool. Recently, it has also been shown that the third and fourth Stokes parameters can be nonzero in passive remote sensing so that complete polarimetric passive remote sensing is also possible [27].

II. FIRST AND SECOND ORDER SOLUTIONS OF THE VECTOR RADIATIVE TRANSFER EQUATION FOR A LAYER OF SPARSELY DISTRIBUTED NONSPHERICAL PARTICLES

Consider a collection of sparsely distributed nonspherical particles with permittivity ϵ_s , embedded in a background medium with permittivity ϵ (region 1) overlying a homogeneous half space of dielectric of permittivity ϵ_2 (region 2). An incident wave is launched from region 0 in direction $(\pi - \theta_0, \phi_0)$. The permittivity of region 0 is the same as that of the background medium of region 1. The vector radiative



transfer equation in region 1 is of the following form, with $0 \leq \theta \leq \pi, 0 \leq \phi \leq 2\pi$.

$$\cos \theta \frac{d}{dz} \bar{I}(\theta, \phi, z) = -\bar{\kappa}_c(\theta, \phi) \cdot \bar{I}(\theta, \phi, z) + \int_0^{2\pi} d\phi' \int_0^\pi d\theta' \sin \theta' \bar{P}(\theta, \phi, \theta', \phi') \cdot \bar{I}(\theta', \phi', z) \quad (1)$$

where $\bar{I}(\theta, \phi, z)$ is a 4×1 column vector denoting the modified Stokes parameters in direction (θ, ϕ)

$$\bar{I}(\theta, \phi, z) = \begin{bmatrix} I_v \\ I_h \\ U \\ V \end{bmatrix} \quad (2)$$

$\bar{\kappa}_c(\theta, \phi)$ is a 4×4 extinction matrix given by

$$\bar{\kappa}_c(\theta, \phi) = \frac{2\pi n_0}{k} \begin{bmatrix} 2\text{Im} \langle f_{vv} \rangle & 0 & \text{Im} \langle f_{vh} \rangle & -\text{Re} \langle f_{vh} \rangle \\ 0 & 2\text{Im} \langle f_{hh} \rangle & \text{Im} \langle f_{hv} \rangle & \text{Re} \langle f_{hv} \rangle \\ 2\text{Im} \langle f_{hv} \rangle & 2\text{Im} \langle f_{vh} \rangle & \text{Im} \langle f_{vv} + f_{hh} \rangle & \text{Re} \langle f_{vv} - f_{hh} \rangle \\ 2\text{Re} \langle f_{hv} \rangle & -2\text{Re} \langle f_{vh} \rangle & \text{Re} \langle f_{hh} - f_{vv} \rangle & \text{Im} \langle f_{vv} + f_{hh} \rangle \end{bmatrix} \quad (3)$$

where n_0 is the number of particles per unit volume. In (3), all the f_{jm} , $j, m = v, h$ are forward scattering amplitudes from (θ, ϕ) of polarization m into the same direction (θ, ϕ) of polarization j . The phase matrix $\bar{P}(\theta, \phi; \theta', \phi')$ is a 4×4 matrix and is given by

$$\bar{P}(\theta, \phi; \theta', \phi') = n_0 \begin{bmatrix} \langle |f_{vv}|^2 \rangle & \langle |f_{vh}|^2 \rangle \\ \langle |f_{hv}|^2 \rangle & \langle |f_{hh}|^2 \rangle \\ 2\text{Re} \langle f_{vv} f_{hv}^* \rangle & 2\text{Re} \langle f_{vh} f_{hh}^* \rangle \\ 2\text{Im} \langle f_{vv} f_{hv}^* \rangle & 2\text{Im} \langle f_{vh} f_{hh}^* \rangle \\ \text{Re} \langle f_{vv} f_{vh}^* \rangle & -\text{Im} \langle f_{vv} f_{vh}^* \rangle \\ \text{Re} \langle f_{hv} f_{hh}^* \rangle & -\text{Im} \langle f_{hv} f_{hh}^* \rangle \\ \text{Re} \langle f_{vv} f_{hh}^* + f_{vh} f_{hv}^* \rangle & -\text{Im} \langle f_{vv} f_{hh}^* - f_{vh} f_{hv}^* \rangle \\ \text{Im} \langle f_{vv} f_{hh}^* + f_{vh} f_{hv}^* \rangle & \text{Re} \langle f_{vv} f_{hh}^* - f_{vh} f_{hv}^* \rangle \end{bmatrix} \quad (4)$$

In (4), all the f_{jm} , $j, m = v, h$ are bistatic scattering amplitudes denoting scattering from a general direction (θ', ϕ') of polarization m into direction (θ, ϕ) of

polarization j . In (1), we can distinguish between the upward going Stokes vector in direction (θ, ϕ) and the downward going Stokes vector in direction $(\pi - \theta, \phi)$ by considering the range $0 \leq \theta \leq \pi/2$ and $0 \leq \phi \leq 2\pi$. The boundary conditions for the vector radiative transfer equation assuming a smooth boundary at $z = -d$ are as follows. At $z = 0$, and at $z = d$, the boundary conditions are respectively

$$\bar{I}(\pi - \theta, \phi, z = 0) = \bar{I}_0 \delta(\cos \theta - \cos \theta_0) \delta(\phi - \phi_0) \quad (5)$$

$$\bar{I}(\theta, \phi, z = -d) = \bar{R}(\theta) \cdot \bar{I}(\pi - \theta, \phi, z = -d) \quad (6)$$

for $0 \leq \theta \leq \pi/2$. In (5) and (6), \bar{I}_0 is the incident Stokes vector, $\bar{R}(\theta)$ is the 4×4 reflectivity matrix for the interface separating regions 1 and 2 and is given by

$$\bar{R}(\theta) = \begin{bmatrix} |R_v(\theta)|^2 & 0 & 0 & 0 \\ 0 & |R_h(\theta)|^2 & 0 & 0 \\ 0 & 0 & \text{Re}(R_v(\theta)R_h(\theta)^*) & -\text{Im}(R_v(\theta)R_h(\theta)^*) \\ 0 & 0 & \text{Im}(R_v(\theta)R_h(\theta)^*) & \text{Re}(R_v(\theta)R_h(\theta)^*) \end{bmatrix} \quad (7)$$

where $R_v(\theta)$ and $R_h(\theta)$ are respectively the Fresnel reflection coefficients for vertically and horizontally polarized waves. Given the vector radiative transfer equation (1) and the boundary conditions in (5) and (6), the Stokes vector can be calculated either numerically or iteratively. Once that is solved, the overall scattered Stokes vector in direction (θ_s, ϕ_s) that is observed by the receiver is $I_s(\theta_s, \phi_s) = I(\theta_s, \phi_s, z = 0) = [I_{vs}, I_{hs}, U_s, V_s]$ and can be calculated. It is proportional to \bar{I}_0 with the proportionality represented by the 4×4 averaged Mueller matrix $\bar{M}(\theta_s, \phi_s; \pi - \theta_0, \phi_0)$ as follows

$$\bar{I}_s(\theta_s, \phi_s) = \bar{M}(\theta_s, \phi_s; \pi - \theta_0, \phi_0) \cdot \bar{I}_0 \quad (8)$$

The Mueller matrix represents the overall polarimetric characteristics of the layer of random discrete scatterers including all multiple scattering effects and boundary reflections that are included in the vector radiative transfer theory. In this paper, the results based on the Mueller matrix will be illustrated for the backscattering direction with $\theta_s = \theta_0$ and $\phi_s = \pi + \phi_0$. Based on the Mueller matrix, we shall illustrate four polarimetric signatures: the phase difference, the copolarized return, the depolarized return, and the degree of polarization. The phase difference between vv and hh waves, ϕ_{vh} , (actually the phase at which the probability density function of phase difference is maximum [28]) is

$$\phi_{vh} = \tan^{-1} \left(\frac{M_{43} - M_{34}}{M_{33} + M_{44}} \right) \quad (9)$$

where M_{ij} is the ij element of the Mueller matrix. For a completely polarized incident wave, with ellipticity angle χ , $-45^\circ \leq \chi \leq 45^\circ$ and orientation angle ψ , $0^\circ \leq \psi \leq 180^\circ$, the incident Stokes vector with unit total intensity is defined



$$M_{mj}(\theta, \phi; \pi - \theta_0, \phi_0) = \sec \theta \sum_{k,i} \bar{E}_{mk}(\theta, \phi) \left\{ \bar{E}(\theta, \phi)^{-1} \bar{P}(\theta, \phi; \pi - \theta_0, \phi_0) \bar{E}(\pi - \theta_0, \phi_0) \right\}_{ki}$$

$$\times \frac{1 - e^{-\beta_k(\theta, \phi) d \sec \theta - \beta_i(\pi - \theta_0, \phi_0) d \sec \theta_0}}{\beta_k(\theta, \phi) \sec \theta + \beta_i(\pi - \theta_0, \phi_0) \sec \theta_0} \left\{ \bar{E}(\pi - \theta_0, \phi_0)^{-1} \right\}_{ij}$$

$$+ \sum_{k,i} \sec \theta \left\{ \bar{E}(\theta, \phi) \bar{D}(-\beta(\theta, \phi) d \sec \theta) \bar{E}(\theta, \phi)^{-1} \bar{R}(\theta) \bar{E}(\pi - \theta, \phi) \right\}_{mk}$$

$$\times \left\{ \bar{E}(\pi - \theta, \phi)^{-1} \bar{P}(\pi - \theta, \phi; \pi - \theta_0, \phi_0) \bar{E}(\pi - \theta_0, \phi_0) \right\}_{ki}$$

$$\times \frac{e^{-\beta_k(\pi - \theta, \phi) d \sec \theta} - e^{-\beta_i(\pi - \theta_0, \phi_0) d \sec \theta_0}}{\beta_i(\pi - \theta_0, \phi_0) \sec \theta_0 - \beta_k(\pi - \theta, \phi) \sec \theta} \left\{ \bar{E}(\pi - \theta_0, \phi_0)^{-1} \right\}_{ij}$$

$$+ \sec \theta \sum_{k,i} \bar{E}_{mk}(\theta, \phi) \left\{ \bar{E}(\theta, \phi)^{-1} \bar{P}(\theta, \phi; \theta_0, \phi_0) \bar{E}(\theta_0, \phi_0) \right\}_{ki}$$

$$\times \frac{e^{-\beta_k(\theta, \phi) d \sec \theta} - e^{-\beta_i(\theta_0, \phi_0) d \sec \theta_0}}{\beta_i(\theta_0, \phi_0) \sec \theta_0 - \beta_k(\theta, \phi) \sec \theta} \left\{ \bar{E}(\theta_0, \phi_0)^{-1} \bar{R}(\theta_0) \bar{E}(\pi - \theta_0, \phi_0) \right\}_{ij}$$

$$\cdot \bar{D}(-\beta(\pi - \theta_0, \phi_0) d \sec \theta_0) \bar{E}(\pi - \theta_0, \phi_0)^{-1} \left\{ \right\}_{ij}$$

$$+ \sum_{k,i} \sec \theta \left\{ \bar{E}(\theta, \phi) \bar{D}(-\beta(\theta, \phi) d \sec \theta) \bar{E}(\theta, \phi)^{-1} \bar{R}(\theta) \bar{E}(\pi - \theta, \phi) \right\}_{mk}$$

$$\times \left\{ \bar{E}(\pi - \theta, \phi)^{-1} \bar{P}(\pi - \theta, \phi; \theta_0, \phi_0) \bar{E}(\theta_0, \phi_0) \right\}_{ki}$$

$$\times \frac{1 - e^{-\beta_k(\pi - \theta, \phi) d \sec \theta - \beta_i(\theta_0, \phi_0) d \sec \theta_0}}{\beta_k(\pi - \theta, \phi) \sec \theta + \beta_i(\theta_0, \phi_0) \sec \theta_0} \left\{ \bar{E}(\theta_0, \phi_0)^{-1} \bar{R}(\theta_0) \bar{E}(\pi - \theta_0, \phi_0) \right\}_{ij}$$

$$\cdot \bar{D}(-\beta(\pi - \theta_0, \phi_0) d \sec \theta_0) \bar{E}(\pi - \theta_0, \phi_0)^{-1} \left\{ \right\}_{ij}$$

$$+ \int_0^{2\pi} d\phi' \int_0^{\pi/2} d\theta' \sin \theta' \sum_{n,k,i} \bar{E}_{mn}(\theta, \phi) \left(\bar{E}(\pi - \theta_0, \phi_0)^{-1} \right)_{ij}$$

$$\times \left\{ \cos \theta_0 \frac{1 - e^{-\beta_n(\theta, \phi) d \sec \theta - \beta_i(\pi - \theta_0, \phi_0) d \sec \theta_0}}{\beta_n(\theta, \phi) \cos \theta_0 + \beta_i(\pi - \theta_0, \phi_0) \cos \theta} \right\}$$

$$\bar{I}_0 = \begin{bmatrix} \frac{1 - \cos 2\chi \cos 2\Psi}{2} \\ \frac{1 + \cos 2\chi \cos 2\Psi}{2} \\ -\cos 2\chi \sin 2\Psi \\ \sin 2\chi \end{bmatrix} \quad (10)$$

where the orientation angle Ψ is defined as the angle between the major axis of the ellipse and the direction of horizontal polarization. The normalized copolarized received power P_n in the backscattering direction corresponds to the case when the receiving antenna measures the same polarization as that of the transmitting antenna. The copolarized power P_n and the backscattering co-polarized coefficient σ are, respectively,

$$P_n = \frac{I_{vs}}{2} (1 - \cos 2\chi \cos 2\Psi) + \frac{I_{hs}}{2} (1 + \cos 2\chi \cos 2\Psi) \quad (11)$$

$$+ \frac{U_s}{2} \cos 2\chi \sin 2\Psi + \frac{V_s}{2} \sin 2\chi \quad (12)$$

$$\sigma = 4\pi \cos \theta_0 P_n$$

The depolarized power P_d and the depolarized coefficient σ_d are respectively

$$P_d = I_{vs} + I_{hs} - P_n \quad (13)$$

$$\sigma_d = 4\pi \cos \theta_0 P_d \quad (14)$$

The degree of polarization for the scattered Stokes vector is

$$m_s = \frac{\sqrt{Q_s^2 + U_s^2 + V_s^2}}{I_s} \quad (15)$$

where $Q_s = I_{vs} - I_{hs}$ and $I_s = I_{vs} + I_{hs}$.

In the following we list the second order theory of the vector radiative transfer equation. To reduce the complexity, we adopt the viewpoint by regarding a volume scattering as an order of scattering and a boundary reflection as half an order of scattering [15]. In this manner, the second order theory will include only five terms: (a) a single upward scattering by the particles, (b) a downward single scattering by the particles that is followed by a reflection off the boundary at $z = -d$, (c) a reflection by the boundary that is followed by a single upward scattering by the particles, (d) a reflection by the boundary at $z = -d$, followed by a single downward scattering by the particles and further followed by a reflection off the boundary at $z = -d$, which then proceeds upward to the receiver, and (e) double volume scattering [12]. The sum of (a), (b), (c), and (d) shall be labelled as first order theory and the sum of all five terms shall be labelled as second order theory.



$$\begin{aligned}
& - \cos \theta' \frac{\left(e^{-\beta_k(\theta', \phi') d \sec \theta'} - e^{-\beta_n(\theta, \phi) d \sec \theta} \right) e^{-\beta_i(\pi - \theta_0, \phi_0) d \sec \theta_0}}{\beta_n(\theta, \phi) \cos \theta' - \beta_k(\theta', \phi') \cos \theta} \\
& \times \frac{\cos \theta_0}{\beta_k(\theta, \phi') \cos \theta_0 + \beta_i(\pi - \theta_0, \phi_0) \cos \theta'} \\
& \times \left[\overline{E}(\theta, \phi)^{-1} \overline{P}(\theta, \phi; \theta', \phi') \overline{E}(\theta', \phi') \right]_{nk} \\
& \times \left[\overline{E}(\theta', \phi')^{-1} \overline{P}(\theta', \phi'; \pi - \theta_0, \phi_0) \overline{E}(\pi - \theta_0, \phi_0) \right]_{ki} \\
& + \frac{\cos \theta_0}{\left[\beta_n(\theta, \phi) \cos \theta' + \beta_k(\pi - \theta', \phi') \cos \theta \right] \left[\beta_n(\theta, \phi) \cos \theta_0 + \beta_i(\pi - \theta_0, \phi_0) \cos \theta \right]} \\
& \times \left[\cos \theta + \frac{e^{-\beta_n(\theta, \phi) d \sec \theta}}{\beta_i(\pi - \theta_0, \phi_0) \cos \theta' - \beta_k(\pi - \theta', \phi') \cos \theta_0} \right] \\
& \times \left\{ \beta_n(\theta, \phi) \cos \theta_0 \cos \theta' \left(e^{-\beta_i(\pi - \theta_0, \phi_0) d \sec \theta_0} - e^{-\beta_k(\pi - \theta', \phi') d \sec \theta'} \right) \right. \\
& + \cos \theta \left[\cos \theta_0 \beta_k(\pi - \theta', \phi') e^{-\beta_i(\pi - \theta_0, \phi_0) d \sec \theta_0} \right. \\
& \left. \left. - \cos \theta' \beta_i(\pi - \theta_0, \phi_0) e^{-\beta_k(\pi - \theta', \phi') d \sec \theta'} \right] \right\} \\
& \times \left[\overline{E}(\theta, \phi)^{-1} \overline{P}(\theta, \phi; \pi - \theta', \phi') \overline{E}(\pi - \theta', \phi') \right]_{nk} \\
& \times \left\{ \overline{E}(\pi - \theta', \phi')^{-1} \overline{P}(\pi - \theta', \phi'; \pi - \theta_0, \phi_0) \overline{E}(\pi - \theta_0, \phi_0) \right\}_{ki} \quad (16)
\end{aligned}$$

where $D(\beta(\theta, \phi)_z \sec \theta)$ is a 4×4 diagonal matrix with the i th element equal to $\exp(\beta_i(\theta, \phi)_z \sec \theta)$.

In (16), $\overline{E}(\theta, \phi)$ is the eigenmatrix for coherent propagation and $\beta_i, i = 1, 2, 3, 4$, are the eigenvalues of coherent wave propagation [2,11,15]. In the numerical examples of this paper, we shall only consider the statistical azimuthal symmetric case when the vertical polarized waves and the horizontal polarized waves are the characteristic polarizations of the medium. In this case, we have [2,11,15],

$$\overline{E}(\theta, \phi) = \begin{bmatrix} 1 & 0 & 0 & 0 \\ 0 & 1 & 0 & 0 \\ 0 & 0 & 1 & 1 \\ 0 & 0 & 0 & -i \end{bmatrix} \quad (17)$$

$$\overline{\beta}(\theta, \phi) = \frac{2\pi n_0}{k} \begin{bmatrix} \beta_1(\theta, \phi) & & & \\ \beta_2(\theta, \phi) & & & \\ \beta_3(\theta, \phi) & & & \\ \beta_4(\theta, \phi) & & & \end{bmatrix} = \frac{2\pi n_0}{k} \begin{bmatrix} 2 < \text{Im} f_{vv}(\theta, \phi; \theta, \phi) > & & & \\ 2 < \text{Im} f_{hh}(\theta, \phi; \theta, \phi) > & & & \\ i(< f_{vv}^*(\theta, \phi; \theta, \phi) - f_{hh}(\theta, \phi; \theta, \phi) >) & & & \\ i(< f_{hh}^*(\theta, \phi; \theta, \phi) - f_{vv}(\theta, \phi; \theta, \phi) >) & & & \end{bmatrix} \quad (18)$$

III. CALCULATION OF EXTINCTION MATRIX ELEMENTS TO ENSURE ENERGY CONSERVATION

The vector radiative transfer equations as given in equations (1), (3)-(4) obey energy conservation if exact numerical calculations are made in calculating the scattering amplitudes to be used in the extinction matrix and phase matrix. If approximate solutions are used to calculate the scattering amplitudes, e.g. Rayleigh scattering approximation and infinite cylinder approximation, steps need to be taken to ensure that the extinction matrix elements and the phase matrix elements are consistent with energy conservation. In this case, we calculate the real part of the forward scattering amplitudes by using the approximate expressions of the forward scattering amplitudes. However, the imaginary parts of the forward scattering amplitudes are calculated as follows. Consider a plane wave with angular frequency ω incident in the direction \hat{s} onto the particle. The particle has permittivity ϵ_p and is occupying volume V_p . The incident field has the electric vector given by $\hat{v}_i E_v + \hat{h}_i E_h$. Then, following a procedure similar to the derivation of the optical theorem except using a linear combination of the two polarizations [2], we get

$$\begin{aligned}
& \frac{4\pi}{k} \left\{ \text{Im} (f_{vv}(\hat{s}, \hat{s}) |E_v|^2 + \text{Im} (f_{hh}(\hat{s}, \hat{s}) |E_h|^2) \right. \\
& \quad \left. - \text{Im} [(f_{vh}^*(\hat{s}, \hat{s}) - f_{hv}(\hat{s}, \hat{s})) E_v E_h^*] \right\} \\
& = \eta \int_{V_p} d\vec{r}' \omega \epsilon_p'' |\overline{E}_p(\vec{r}')|^2 + \int_{4\pi} d\hat{s}' [|f_{vv}(\hat{s}', \hat{s}) E_v + f_{vh}(\hat{s}', \hat{s}) E_h|^2 \\
& \quad + |f_{hv}(\hat{s}', \hat{s}) E_v + f_{hh}(\hat{s}', \hat{s}) E_h|^2] \quad (19)
\end{aligned}$$

where η is the wave impedance of the background medium, ϵ_p'' is the imaginary part of the permittivity of the particle, and $\overline{E}_p(\vec{r}')$ is the field inside the particle.

Next, consider the incident wave to be of unit amplitude in the vertical polarization, i.e., $E_v = 1$ and $E_h = 0$. We then calculate the interior field of the particle $\overline{E}_p^v(\vec{r}')$ and then the imaginary part of the forward scattering amplitude $\text{Im} f_{vv}$ is given by (20) below. In the second case, consider the incident wave to be of unit amplitude in the horizontal polarization, i.e., $E_v = 0$ and $E_h = 1$. We then calculate the interior field of the particle $\overline{E}_p^h(\vec{r}')$ and then the imaginary

part of the forward scattering amplitude $\text{Im} f_{hh}$ is given by (21) below

$$\frac{4\pi}{k} \text{Im} f_{vv}(\hat{s}, \hat{s}) = \eta \int_{V_p} d\vec{r} \omega \epsilon_p'' |E_p^V(\vec{r})|^2 + \int_{4\pi} d\hat{s}' [|f_{vv}(\hat{s}', \hat{s})|^2 + |f_{hv}(\hat{s}', \hat{s})|^2] \quad (20)$$

$$\frac{4\pi}{k} \text{Im} f_{hh}(\hat{s}, \hat{s}) = \eta \int_{V_p} d\vec{r} \omega \epsilon_p'' |E_p^H(\vec{r})|^2 + \int_{4\pi} d\hat{s}' [|f_{vh}(\hat{s}', \hat{s})|^2 + |f_{hh}(\hat{s}', \hat{s})|^2] \quad (21)$$

Thus, to use (20) and (21) to calculate the imaginary part of the forward scattering amplitudes, we have to first obtain the internal fields and then integrate over the volume of the particle. To calculate $\text{Im} f_{vh}$ and $\text{Im} f_{hv}$, we consider an incident linear polarization L with

$$E_v = E_h = \frac{1}{\sqrt{2}} \quad (22)$$

and the internal field represented by $\vec{E}_p^L(\vec{r}')$ in this case. Then

$$\begin{aligned} & \frac{2\pi}{k} \text{Im} \{ (f_{vv}(\hat{s}, \hat{s})) + \text{Im} (f_{hh}(\hat{s}, \hat{s})) - \text{Im} [(f_{vh}^*(\hat{s}, \hat{s}) - f_{hv}(\hat{s}, \hat{s}))] \} \\ &= \eta \int_{V_p} d\vec{r}' \omega \epsilon_p'' |\vec{E}_p^L(\vec{r}')|^2 + \frac{1}{2} \int_{4\pi} d\hat{s}' [|f_{vv}(\hat{s}', \hat{s}) + f_{vh}(\hat{s}', \hat{s})|^2] \\ &+ |f_{hv}(\hat{s}', \hat{s}) + f_{hh}(\hat{s}', \hat{s})|^2 \end{aligned} \quad (23)$$

In general, we cannot separate $\text{Im} f_{vh}$ and $\text{Im} f_{hv}$ in (23). We can, however, separate them by assuming inversion symmetry of the particle. If the particle obeys inversion symmetry, we have a relation between f_{vh} and f_{hv} . Furthermore, we have a reciprocal relation between f_{vh} and f_{hv} [2,27]. The reciprocal relations and the inversion symmetry relations are given respectively in (24) and (25).

$$f_{vh}(\hat{s}', \hat{s}) = -f_{hv}(-\hat{s}, -\hat{s}') \quad (24)$$

$$f_{hv}(\hat{s}', \hat{s}) = -f_{hv}(-\hat{s}', -\hat{s}) \quad (25)$$

Combining (23), (24), and (25) gives

$$f_{vh}(\hat{s}, \hat{s}) = f_{hv}(\hat{s}, \hat{s}) \quad (26)$$

$$\begin{aligned} \frac{4\pi}{k} \text{Im} (f_{hv}(\hat{s}, \hat{s})) &= \frac{4\pi}{k} \text{Im} (f_{vh}(\hat{s}, \hat{s})) \\ &= \eta \int_{V_p} d\vec{r}' \omega \epsilon_p'' |\vec{E}_p^L(\vec{r}')|^2 + \frac{1}{2} \int_{4\pi} d\hat{s}' [|f_{vv}(\hat{s}', \hat{s}) + f_{vh}(\hat{s}', \hat{s})|^2] \\ &+ |f_{hv}(\hat{s}', \hat{s}) + f_{hh}(\hat{s}', \hat{s})|^2] \\ &- \frac{2\pi}{k} \{ \text{Im} (f_{vv}(\hat{s}, \hat{s})) + \text{Im} (f_{hh}(\hat{s}, \hat{s})) \} \end{aligned} \quad (27)$$

Thus the imaginary parts of the forward scattering amplitudes can be calculated by using (20), (21), and (27). Equation (27), however, only applies if the particle has inversion symmetry.

IV. SCATTERING AMPLITUDES AND EXTINCTION MATRIX ELEMENTS OF A FINITE DIELECTRIC CYLINDER BASED ON INFINITE CYLINDER APPROXIMATION

In this section, we derive expressions for the scattering amplitudes for a finite cylinder of length L , radius a , permittivity ϵ_p , and wavenumber k_p . The surface field on the surface of the finite length cylinder is assumed to be the same as that of an infinite cylinder. Huygen's principle is then used to calculate the scattering amplitude functions. The radiation from the two end faces of the cylinder are ignored. There are two choices of the surface fields in applying Huygen's principle. One choice is to use the total surface field which is the sum of the incident field and the scattered field [4,13]. The second choice is to use only the scattered field for the surface field. The second choice has the advantage that the scattered field from the finite cylinder will vanish in the event that the permittivity ϵ_p approaches the value of the background permittivity ϵ . In this section, we also derive expressions for the absorption of the cylinder to calculate the imaginary parts of the forward scattering amplitudes in a manner consistent with energy conservation. In the derivation of the absorption, we also assume that the interior field of the finite cylinder is the same as that of an infinite cylinder and integration is performed over the volume of the finite cylinder.

Consider an incident plane wave in the direction \hat{s}_i ; impinging on the cylinder with axis \hat{z}_b (Fig. 2). The subscript b denotes body frame with \hat{x}_b , \hat{y}_b , and \hat{z}_b as axes. The axis of symmetry \hat{z}_b is at an angle with respect to the principal frame of Fig. 1.

$$\hat{z}_b = \sin \beta \cos \alpha \hat{x} + \sin \beta \sin \alpha \hat{y} + \cos \beta \hat{z} \quad (28)$$

Note that the results in this section are calculated for one cylinder with fixed orientation as represented by α and β . The results will be averaged over the orientation in Section VI. Let the incident electric field be given by

$$\vec{E}^i = (E_{vb_i} \hat{v}_{b_i} + E_{hb_i} \hat{h}_{b_i}) \quad (29)$$

$$\hat{s}_i = \sin \theta_{b_i} \hat{x}_b + \cos \theta_{b_i} \hat{z}_b \quad (30)$$

$$\hat{v}_{b_i} = \cos \theta_{b_i} \hat{x}_b - \sin \theta_{b_i} \hat{z}_b \quad (31)$$

$$\hat{h}_{b_i} = \hat{y}_b \quad (32)$$

Since the cylinder is rotationally symmetric, we have chosen \hat{y}_b to coincide with \hat{h}_{b_i} ; without loss of generality. In (29), without loss of generality, we have let the incident direction to be in the $\hat{z}_b \hat{x}_b$ plane. We assume the surface fields of the finite cylinder to be the same as that of an infinite cylinder and the surface fields can be expressed as follows

$$\begin{bmatrix} E_{\phi b} \\ E_{z b} \\ \eta H_{\phi b} \\ \eta H_{z b} \end{bmatrix} = \sum_{m=-\infty}^{\infty} e^{im\phi_b + ik_z b} \begin{bmatrix} E_{\phi m} \\ E_{z m} \\ \eta H_{\phi m} \\ \eta H_{z m} \end{bmatrix} \quad (33)$$

where

$$k_{z b_i} = k \cos \theta_{b_i} \quad (34)$$

The surface fields based on the total field approach and the scattered field can be expressed in terms of the coefficients C_m and ηD_m which are governed by the following equations.

$$C_m J_m(w_p) \left(k_p^2 a^2 - k^2 a^2 \right) \frac{m k_{zbi} a}{w_p^2} + \eta D_m i k a \left[-\frac{w^2 J'_m(w_p)}{w_p} + \frac{J_m(w_p) w H'_m(w)}{H_m(w)} \right] = -\frac{2 E_{hbi} w}{\pi H_m(w)} \quad (35)$$

$$C_m i k a \left[\frac{\epsilon_p w^2 J'_m(w_p)}{\epsilon} - \frac{J_m(w_p) w H'_m(w)}{H_m(w)} \right] + \eta D_m J_m(w_p) \left(k_p^2 a^2 - k^2 a^2 \right) \frac{m k_{zbi} a}{w_p^2} = -\frac{2 E_{vbi} w}{\pi H_m(w)} \quad (36)$$

where

$$w = k a \sin \theta_{bi} \quad (37)$$

$$w_p = \sqrt{k_p^2 - k^2} \cos^2 \theta_{bi} a \quad (38)$$

k_p is the wavenumber of the particle, J_m and H_m are, respectively, the Bessel function and Hankel function of the first kind. In the following we list the two approximations.

(1) The scattered field approximation. The surface tangential fields are replaced by that of the scattered field. Thus we use the following substitution for (33)

$$\begin{bmatrix} E_{\phi m} \\ E_{z m} \\ \eta H_{\phi m} \\ \eta H_{z m} \end{bmatrix} = \begin{bmatrix} E_{\phi m}^s \\ E_{z m}^s \\ \eta H_{\phi m}^s \\ \eta H_{z m}^s \end{bmatrix} \quad (39)$$

where

$$E_{\phi m}^s = i^m \left(-\frac{m k_{zbi} a}{w^2} A_m H_m(w) - \frac{i k a}{w} \eta B_m H'_m(w) \right) \quad (40)$$

$$E_{z m}^s = i^m A_m H_m(w) \quad (41)$$

$$\eta H_{\phi m}^s = i^m \left(-\frac{m k_{zbi} a}{w^2} \eta B_m H_m(w) + \frac{i k a}{w} A_m H'_m(w) \right) \quad (42)$$

$$\eta H_{z m}^s = i^m \eta B_m H_m(w) \quad (43)$$

$$A_m = \frac{C_m J_m(w_p)}{H_m(w)} + E_{vbi} \sin \theta_{bi} \frac{J_m(w)}{H_m(w)} \quad (44)$$

$$\eta B_m = \eta D_m \frac{J_m(w_p)}{H_m(w)} - E_{hbi} \sin \theta_{bi} \frac{J_m(w)}{H_m(w)} \quad (45)$$

(2) The total field approximation. In this case the surface field harmonics are approximated by the total field on the surface of the infinite cylinder. The total field

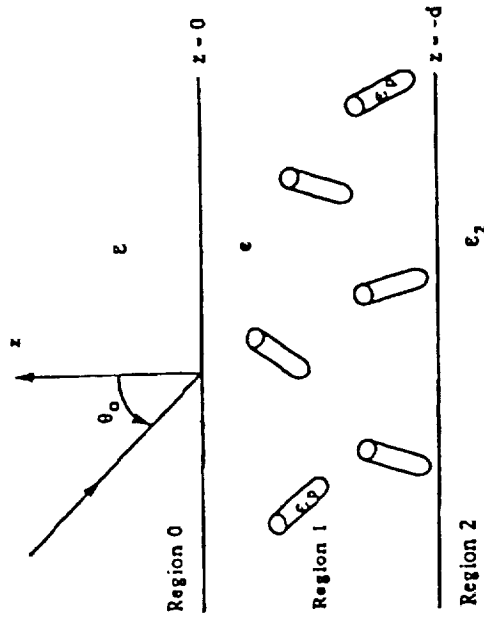


Figure 1. An incident plane wave impinging upon a layer of sparsely distributed dielectric cylinders of finite length and permittivity ϵ_p . The background permittivity of the layer is ϵ and is the same as region 0. The layer is overlying a homogeneous half space with permittivity ϵ_2 .

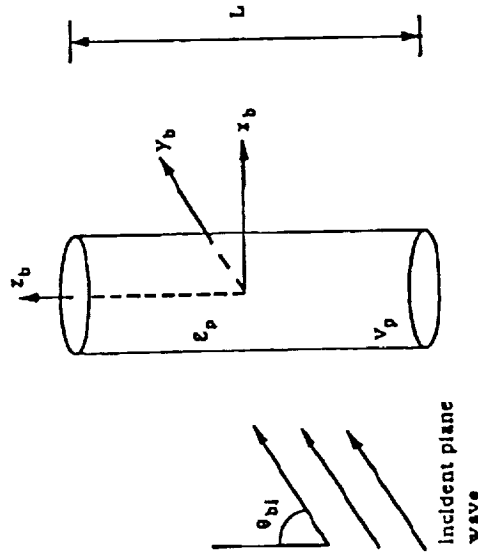


Figure 2. The dielectric cylinder with permittivity ϵ_p in its body frame with axes x_b , y_b , and symmetry axis z_b . The length is L and the radius is a . The incident plane wave is launched in the direction $(\theta_{bi}, \phi_{bi} = 0)$.

is the sum of the scattered field and incident field. Thus, in this approximation, we use the following substitution for (33)

$$E_{\phi m} = E_{\phi m}^s + i^m \left(E_{vbi} \cos \theta_{bi} \frac{m J_m(w)}{w} - i E_{hbi} J_m'(w) \right) \quad (46)$$

$$E_{z m} = E_{z m}^s - i^m E_{vbi} \sin \theta_{bi} J_m(w) \quad (47)$$

$$\eta H_{\phi m} = \eta H_{\phi m}^s + i^m \left(-E_{hbi} \cos \theta_{bi} \frac{m J_m(w)}{w} - i E_{vbi} J_m'(w) \right) \quad (48)$$

$$\eta H_{z m} = \eta H_{z m}^s + i^m E_{hbi} \sin \theta_{bi} J_m(w) \quad (49)$$

Given the surface fields of either (1) scattered fields or (2) total fields, the scattering amplitudes in the body frame are

$$f_{v,\alpha}(\theta_{bs}, \phi_{bs}; \theta_{bi}, \phi_{bi} = 0) = a \frac{\sin \left(k \frac{1}{2} (\cos \theta_{bs} - \cos \theta_{bi}) \right)}{k (\cos \theta_{bs} - \cos \theta_{bi})} \sum_{m=-\infty}^{\infty} (-i)^m e^{im\phi_{bs}} F_{v,\alpha m} \quad (50a)$$

$$f_{h,\alpha}(\theta_{bs}, \phi_{bs}; \theta_{bi}, \phi_{bi} = 0) = a \frac{\sin \left(k \frac{1}{2} (\cos \theta_{bs} - \cos \theta_{bi}) \right)}{k (\cos \theta_{bs} - \cos \theta_{bi})} \sum_{m=-\infty}^{\infty} (-i)^m e^{im\phi_{bs}} F_{h,\alpha m} \quad (50b)$$

where

$$F_{v,\alpha m} = -ik \sin \theta_{bs} \eta H_{\phi m} J_m(w_s) - \frac{m}{w_s} \cos \theta_{bs} \eta H_{z m} J_m(w_s) - k E_{z m} J_m'(w_s) \quad (51a)$$

$$F_{h,\alpha m} = -ik \sin \theta_{bs} E_{\phi m} J_m(w_s) - \frac{m}{w_s} \cos \theta_{bs} E_{z m} J_m(w_s) + k \eta H_{z m} J_m'(w_s) \quad (51b)$$

and $\alpha = v, h$. In (50)-(51), when we set $\alpha = v$, we let $(E_{vbi} = 1, E_{hbi} = 0)$ in (35)-(36) and (47)-(49) so that the incident wave is vertically polarized in the body frame. When we set $\alpha = h$ in (50)-(51), we let $(E_{vbi} = 0, E_{hbi} = 1)$ in (35)-(36) and (47)-(49) so that the incident wave is horizontally polarized in the body frame. To transform between the body frame to the principal frame, we use the following 2×2 matrix multiplication

$$\begin{bmatrix} f_{vv}(\theta_s, \phi_s; \theta_i, \phi_i) & f_{vh}(\theta_s, \phi_s; \theta_i, \phi_i) \\ f_{hv}(\theta_s, \phi_s; \theta_i, \phi_i) & f_{hh}(\theta_s, \phi_s; \theta_i, \phi_i) \end{bmatrix} = \begin{bmatrix} \hat{v}_s \cdot \hat{v}_{bs} & \hat{v}_s \cdot \hat{h}_{bs} \\ \hat{h}_s \cdot \hat{v}_{bs} & \hat{h}_s \cdot \hat{h}_{bs} \end{bmatrix} \begin{bmatrix} f_{v_b}(\theta_{bs}, \phi_{bs}; \theta_{bi}, \phi_{bi} = 0) & f_{v_b} \cdot \hat{h}_i \\ f_{h_b}(\theta_{bs}, \phi_{bs}; \theta_{bi}, \phi_{bi} = 0) & f_{h_b} \cdot \hat{h}_i \end{bmatrix} \quad (53)$$

where

$$\hat{z}_i = \sin \theta_i \cos \phi_i \hat{x} + \sin \theta_i \sin \phi_i \hat{y} + \cos \theta_i \hat{z} \quad (54)$$

$$\hat{v}_i = \cos \theta_i \cos \phi_i \hat{x} + \cos \theta_i \sin \phi_i \hat{y} - \sin \theta_i \hat{z} \quad (55)$$

$$\hat{h}_i = -\sin \phi_i \hat{x} + \cos \phi_i \hat{y} \quad (56)$$

$$\hat{z}_s = \sin \theta_s \cos \phi_s \hat{x} + \sin \theta_s \sin \phi_s \hat{y} + \cos \theta_s \hat{z}$$

$$= \sin \theta_{bs} \cos \phi_{bs} \hat{x}_b + \sin \theta_{bs} \sin \phi_{bs} \hat{y}_b + \cos \theta_{bs} \hat{z}_b \quad (57)$$

$$\hat{v}_s = \cos \theta_s \cos \phi_s \hat{x} + \cos \theta_s \sin \phi_s \hat{y} - \sin \theta_s \hat{z} \quad (58)$$

$$\hat{h}_s = -\sin \phi_s \hat{x} + \cos \phi_s \hat{y} \quad (59)$$

$$\hat{v}_{bs} = \cos \theta_{bs} \cos \phi_{bs} \hat{x}_b + \cos \theta_{bs} \sin \phi_{bs} \hat{y}_b - \sin \theta_{bs} \hat{z}_b \quad (60)$$

$$\hat{h}_{bs} = -\sin \phi_{bs} \hat{x}_b + \cos \phi_{bs} \hat{y}_b \quad (61)$$

$$\hat{y}_b = \frac{\hat{z}_b \times \hat{z}_i}{\sin \theta_{bi}} \quad (62)$$

Note that the angle θ_{bi} can be related to θ_i and ϕ_i by using (28), (30), (32), (54), and (62). It depends on the orientation of the body axis \hat{z}_b as represented by the orientation angles α and β of (28). Similarly, θ_{bs} and ϕ_{bs} can be related to θ_s and ϕ_s by using (28), (57), and (62).

To find the absorption cross section so as to apply (20), (21), and (27) to find the imaginary parts of the forward scattering amplitudes, we first calculate the imaginary parts of the forward scattering amplitudes and the absorption cross sections in the body frame. The absorption cross sections are calculated by assuming that the internal fields of the cylinder are the same as that of the infinite cylinder.

$$\begin{aligned} & \eta \int_{V_b} d\vec{r}' \omega \epsilon_p'' \left| \vec{E}_p^{\text{in}}(\vec{r}') \right|^2 \\ &= 2\pi k L \alpha^4 \frac{\epsilon_p''}{\epsilon} \left\{ \left[\frac{|C_m|^2 k^2 + |\eta D_m|^2 k^2}{|w_p|^2 (w_p^2 - w_p^{*2})} \left[w_p J_m(w_p) J_m'(w_p) - w_p^* J_m(w_p^*) J_m'(w_p^*) \right] \right] \right. \\ & \quad \left. - 2\text{Re} \left[\frac{ik_{zbi} C_m \eta D_m^* k m J_m(w_p) J_m(w_p^*)}{|w_p|^4} \right] \right\} \\ & \quad + \frac{|C_m|^2 \left[w_p^* J_m(w_p) J_m'(w_p^*) - w_p J_m(w_p) J_m'(w_p) \right]}{(w_p^2 - w_p^{*2}) \alpha^2} \quad (63) \end{aligned}$$

$$\frac{4\pi}{k} \text{Im} f_{v_b \gamma_b}(\theta_{bi}, \phi_{bi} = 0; \theta_{bi}, \phi_{bi} = 0)$$

$$= \eta \int_{V_p} d\vec{r}' \omega \epsilon_p'' \left| \vec{E}_p^{\text{in}}(\vec{r}') \right|^2$$

$$+ 2\pi \int_0^\pi d\theta_{bs} \sin \theta_{bs} \alpha^2 \frac{\sin^2 \left(k \frac{1}{2} (\cos \theta_{bs} - \cos \theta_{bi}) \right)}{k (\cos \theta_{bs} - \cos \theta_{bi})} \sum_{m=-\infty}^{\infty} \left[|F_{v_b m}|^2 + |F_{h_b m}|^2 \right] \quad (64)$$

with $\gamma_b = v, h$. For $\gamma_b = v$, we set $(E_{vbi} = 1, E_{hbi} = 0)$ to calculate the C_m and ηD_m in (35) and (36). For $\gamma_b = h$, we set $(E_{vbi} = 0, E_{hbi} = 1)$ to calculate the C_m and ηD_m in (35) and (36). In the body frame,

$$\text{Im} f_{v_b h_b}(\theta_{bi}, \phi_{bi} = 0; \theta_{bi}, \phi_{bi} = 0) = \text{Im} f_{h_b v_b}(\theta_{bi}, \phi_{bi} = 0; \theta_{bi}, \phi_{bi} = 0) = 0 \quad (65)$$

To find the forward scattering amplitudes in the principal frame, we use (53) and



Step 1: Calculation of Impedance Matrix and Admittance Matrix

Given the length, radius, and complex permittivity of the cylinder, the impedance matrix and the admittance matrix of the cylinder are calculated by solving the surface integral equations only one time using the Method of Moment Body of Revolution Code [21,22]. The admittance matrix is then stored.

Step 2: Calculation of Bistatic Scattering Amplitudes for Each Harmonic in the Body Frame

Consider an incident field given in the body frame by

$$\vec{E}^i = (E_{\nu\theta_i} \hat{\nu}_{\theta_i} + E_{h\theta_i} \hat{h}_{\theta_i}) \quad (70)$$

$$\hat{s}_i = \sin \theta_{bi} \hat{x}_b + \cos \theta_{bi} \hat{z}_b \quad (71)$$

$$\hat{\nu}_{\nu i} = \cos \theta_{bi} \hat{x}_b - \sin \theta_{bi} \hat{z}_b \quad (72)$$

$$\hat{h}_{\theta_i} = \hat{y}_b \quad (73)$$

Because of rotational symmetry, we have taken $\phi_{bi} = 0$ without loss of generality. Given the admittance matrix stored in step 1, a product can be taken between the admittance matrix and the incident field to give the surface fields at each discretized point on the surface for each harmonic. These include $E_{\phi m}^C(z_b)$, $H_{\phi m}^C(z_b)$, $E_{z m}^C(z_b)$, and $H_{z m}^C(z_b)$ on the curved side, $E_{\rho m}^U(\rho_b)$, $H_{\rho m}^U(\rho_b)$, $E_{\phi m}^L(\rho_b)$, and $H_{\phi m}^L(\rho_b)$ on the upper side, and $E_{\rho m}^L(\rho_b)$, $H_{\rho m}^L(\rho_b)$, $E_{\phi m}^U(\rho_b)$, and $H_{\phi m}^U(\rho_b)$ on the lower side, where z_b denotes the coordinate on the curved side and ρ_b denotes the cylindrical radial coordinate on the upper side and the lower side. The bistatic scattering amplitudes in the body frame are

$$f_{\nu_b \nu_b}(\theta_{bs}, \phi_{bs}; \theta_{bi}, \phi_{bi} = 0) = \sum_{m=-\infty}^{\infty} e^{im\phi_{bs}} f_{\nu_b \nu_b m}(\theta_{bs}, \theta_{bi}) \quad (74)$$

$$f_{\nu_b h_b}(\theta_{bs}, \phi_{bs}; \theta_{bi}, \phi_{bi} = 0) = \sum_{m=-\infty}^{\infty} e^{im\phi_{bs}} f_{\nu_b h_b m}(\theta_{bs}, \theta_{bi}) \quad (75)$$

$$f_{h_b \nu_b}(\theta_{bs}, \phi_{bs}; \theta_{bi}, \phi_{bi} = 0) = \sum_{m=-\infty}^{\infty} e^{im\phi_{bs}} f_{h_b \nu_b m}(\theta_{bs}, \theta_{bi}) \quad (76)$$

$$f_{h_b h_b}(\theta_{bs}, \phi_{bs}; \theta_{bi}, \phi_{bi} = 0) = \sum_{m=-\infty}^{\infty} e^{im\phi_{bs}} f_{h_b h_b m}(\theta_{bs}, \theta_{bi}) \quad (77)$$

The bistatic scattering amplitudes for each harmonic, $f_{\nu_b \nu_b m}(\theta_{bs}, \theta_{bi})$, $f_{\nu_b h_b m}(\theta_{bs}, \theta_{bi})$, $f_{h_b \nu_b m}(\theta_{bs}, \theta_{bi})$, and $f_{h_b h_b m}(\theta_{bs}, \theta_{bi})$ can be expressed in terms of the surface fields as follows

$$f_{\nu_b \nu_b m}(\theta_{bs}, \theta_{bi}) = (-i)^m \frac{a}{2} \left[-ik \left\{ \sin \theta_{bs} \eta H_{\phi m} J_m(w_s) \right. \right. \\ \left. \left. + \frac{m}{w_s} \cos \theta_{bs} \eta H_{z m} J_m(w_s) \right\} - k E_{z m} J_m'(w_s) \right]$$

65) to obtain

$$\text{Im } f_{\nu\nu}(\theta_i, \phi_i; \theta_i, \phi_i) = (\text{Im } f_{\nu_b \nu_b}(\theta_{bi}, \phi_{bi} = 0; \theta_{bi}, \phi_{bi} = 0)) (\hat{\nu}_i \cdot \hat{\nu}_{bi})^2 \\ + (\text{Im } f_{h_b h_b}(\theta_{bi}, \phi_{bi} = 0; \theta_{bi}, \phi_{bi} = 0)) (\hat{\nu}_i \cdot \hat{h}_{bi})^2 \quad (66)$$

$$\text{Im } f_{hh}(\theta_i, \phi_i; \theta_i, \phi_i) = (\text{Im } f_{\nu_b \nu_b}(\theta_{bi}, \phi_{bi} = 0; \theta_{bi}, \phi_{bi} = 0)) (\hat{h}_i \cdot \hat{\nu}_{bi})^2 \\ + (\text{Im } f_{h_b h_b}(\theta_{bi}, \phi_{bi} = 0; \theta_{bi}, \phi_{bi} = 0)) (\hat{h}_i \cdot \hat{h}_{bi})^2 \quad (67)$$

$$\text{Im } f_{\nu h}(\theta_i, \phi_i; \theta_i, \phi_i) = (\text{Im } f_{\nu_b \nu_b}(\theta_{bi}, \phi_{bi} = 0; \theta_{bi}, \phi_{bi} = 0)) (\hat{\nu}_i \cdot \hat{\nu}_{bi}) (\hat{h}_i \cdot \hat{\nu}_{bi}) \\ + (\text{Im } f_{h_b h_b}(\theta_{bi}, \phi_{bi} = 0; \theta_{bi}, \phi_{bi} = 0)) (\hat{h}_i \cdot \hat{h}_{bi}) (\hat{\nu}_i \cdot \hat{\nu}_{bi}) \quad (68)$$

$$\text{Im } f_{h\nu}(\theta_i, \phi_i; \theta_i, \phi_i) = (\text{Im } f_{\nu_b \nu_b}(\theta_{bi}, \phi_{bi} = 0; \theta_{bi}, \phi_{bi} = 0)) (\hat{h}_i \cdot \hat{\nu}_{bi}) (\hat{\nu}_i \cdot \hat{\nu}_{bi}) \\ + (\text{Im } f_{h_b h_b}(\theta_{bi}, \phi_{bi} = 0; \theta_{bi}, \phi_{bi} = 0)) (\hat{h}_i \cdot \hat{h}_{bi}) (\hat{\nu}_i \cdot \hat{\nu}_{bi}) \quad (69)$$

Note that the results in this section are calculated for one finite cylinder with orientation in terms of α and β as given by (28). In Section VI, these will be averaged over orientations.

V. METHOD OF MOMENTS AND ENERGY CONSERVATION

We also use a method of moment (MOM) body of revolution code [21,22] to calculate scattering from a finite cylinder. In this code, surface integral equations are solved by using the method of moments. The variations of the unknown electric and magnetic surface fields are approximated by staggered pulse functions in the t -direction and are expanded in Fourier series in the ϕ -direction. The detailed discretization procedure can be found in [21] and [22]. For computational efficiency, it is important to note that it is required to calculate the inverse of the impedance matrix or admittance matrix only once for a cylinder of fixed length, radius, and permittivity. The admittance matrix of the cylinder is then stored. Given incident fields of arbitrary polarization, incident angle, and orientation of the cylinder, the surface fields induced on the surface of the cylinder are calculated by multiplying the admittance matrix with the incident field. In this case, the total surface fields on the curved sides as well as on the two ends of the cylinder are calculated. The bistatic scattering amplitudes can then be calculated. In our implementation, we further store the bistatic scattering amplitudes in the body frame for each harmonic. For an arbitrary incident field and with arbitrary orientation, the bistatic scattering amplitudes in the principal frame can be calculated from that of the stored scattering amplitudes by rotation of coordinates and by interpolation. We also carry out the energy conservation test for the code. The code not only satisfies energy conservation but also reciprocity.

$$\begin{aligned}
& + \frac{(-i)^m}{2} e^{ik(\cos\theta_{bi}-\cos\theta_{bs})\frac{L}{2}} \int_0^a d\rho_b \rho_b \left[\frac{imk}{k \sin\theta_{bs}\rho_b} J_m(k \sin\theta_{bs}\rho_b) \right. \\
& \times \left. \left\{ -E_{\phi m}^U(\rho_b) + \eta H_{\rho m}^U(\rho_b) \cos\theta_{bs} \right\} \right. \\
& + k J_m'(k \sin\theta_{bs}\rho_b) \left\{ E_{\rho m}^U(\rho_b) + \eta H_{\phi m}^U(\rho_b) \cos\theta_{bs} \right\} \left. \right] \\
& + \frac{(-i)^m}{2} e^{-ik(\cos\theta_{bi}-\cos\theta_{bs})\frac{L}{2}} \int_0^a d\rho_b \rho_b \left[-\frac{imk}{k \sin\theta_{bs}\rho_b} J_m(k \sin\theta_{bs}\rho_b) \right. \\
& \times \left. \left\{ -E_{\phi m}^L(\rho_b) + \eta H_{\rho m}^L(\rho_b) \cos\theta_{bs} \right\} \right. \\
& - k J_m'(k \sin\theta_{bs}\rho_b) \left\{ E_{\rho m}^L(\rho_b) + \eta H_{\phi m}^L(\rho_b) \cos\theta_{bs} \right\} \left. \right] \\
& f_{h_b\delta_b m}(\theta_{bs}, \theta_{bi}) = (-i)^m \frac{\alpha}{2} \left[-ik \{ \sin\theta_{bs} E_{\phi m}^U J_m(w_s) \right. \\
& + \frac{m}{w_s} \cos\theta_{bs} E_{zm} J_m(w_s) \left. \right] + k \eta H_{zm} J_m'(w_s) \\
& + \frac{(-i)^m}{2} e^{ik(\cos\theta_{bi}-\cos\theta_{bs})\frac{L}{2}} \int_0^a d\rho_b \rho_b \left[\frac{imk}{k \sin\theta_{bs}\rho_b} J_m(k \sin\theta_{bs}\rho_b) \right. \\
& \times \left. \left\{ \eta H_{\phi m}^U(\rho_b) + E_{\rho m}^U(\rho_b) \cos\theta_{bs} \right\} \right. \\
& + k J_m'(k \sin\theta_{bs}\rho_b) \left\{ -\eta H_{\rho m}^U(\rho_b) + E_{\phi m}^U(\rho_b) \cos\theta_{bs} \right\} \left. \right] \\
& + \frac{(-i)^m}{2} e^{-ik(\cos\theta_{bi}-\cos\theta_{bs})\frac{L}{2}} \int_0^a d\rho_b \rho_b \left[-\frac{imk}{k \sin\theta_{bs}\rho_b} J_m(k \sin\theta_{bs}\rho_b) \right. \\
& \times \left. \left\{ E_{\rho m}^L(\rho_b) \cos\theta_{bs} + \eta H_{\phi m}^L(\rho_b) \right\} \right. \\
& - k J_m'(k \sin\theta_{bs}\rho_b) \left\{ E_{\phi m}^L(\rho_b) \cos\theta_{bs} - \eta H_{\rho m}^L(\rho_b) \right\} \left. \right] \\
& \text{where } \delta = v, h \\
& w_s = k \sin\theta_{bs} \\
& H_{\phi m} = \int_{-\frac{L}{4}}^{\frac{L}{4}} dz_b e^{ik(\cos\theta_{bi}-\cos\theta_{bs})z_b} H_{\phi m}^C(z_b) \\
& H_{zm} = \int_{-\frac{L}{4}}^{\frac{L}{4}} dz_b e^{ik(\cos\theta_{bi}-\cos\theta_{bs})z_b} H_{zm}^C(z_b) \\
& E_{\phi m} = \int_{-\frac{L}{4}}^{\frac{L}{4}} dz_b e^{ik(\cos\theta_{bi}-\cos\theta_{bs})z_b} E_{\phi m}^C(z_b) \\
& E_{zm} = \int_{-\frac{L}{4}}^{\frac{L}{4}} dz_b e^{ik(\cos\theta_{bi}-\cos\theta_{bs})z_b} E_{zm}^C(z_b)
\end{aligned} \tag{78}$$

For $\delta_b = v_b$, we set $(E_{vbi} = 1, E_{hbi} = 0)$ to calculate the surface fields from the admittance matrix. For $\delta_b = h_b$, we set $(E_{vbi} = 0, E_{hbi} = 1)$ to calculate

the surface fields from the admittance matrix. The bistatic scattering amplitudes for each harmonic $f_{v_b h_b m}(\theta_{bs}, \theta_{bi})$, $f_{v_b h_b m}(\theta_{bs}, \theta_{bi})$, $f_{h_b v_b m}(\theta_{bs}, \theta_{bi})$, and $f_{h_b h_b m}(\theta_{bs}, \theta_{bi})$ can be stored for a two dimensional array of values of θ_{bs} and θ_{bi} . The bistatic scattering amplitudes for each harmonic at arbitrary values of θ_{bs} and θ_{bi} can then be calculated by interpolation.

Step 3: Calculation of Bistatic Scattering Amplitude in the Principal Frame
For an incident plane wave in the direction \hat{s}_i as given by (54) impinging upon the cylinder with body axis

$$\hat{z}_b = \sin\beta \cos\alpha \hat{x} + \sin\beta \sin\alpha \hat{y} + \cos\beta \hat{z} \tag{28}$$

the transformation of bistatic scattering amplitudes between the principal frame and the body frame follows that of (53)-(62). Calculation of body frame scattering amplitudes are done by using (74)-(77) and interpolation.

We also carry out energy conservation tests. For the case of real permittivity ϵ_r without absorption loss, the optical theorem can be verified by checking the equality of extinction and scattering cross sections. Thus for the case of real ϵ_r , the following relations from (20) to (21) have to be obeyed to satisfy energy conservation.

$$\begin{aligned}
& \frac{4\pi}{k} \text{Im} f_{\delta_b \delta_b}(\theta_{bi}, \phi_{bi} = 0; \theta_{bi}, \phi_{bi} = 0) \\
& = 2\pi \int_0^\pi d\theta_{bs} \sin\theta_{bs} \sum_{m=-\infty}^{\infty} \left[|f_{v_b \delta_b m}(\theta_{bs}, \theta_{bi})|^2 + |f_{h_b \delta_b m}(\theta_{bs}, \theta_{bi})|^2 \right] \tag{85}
\end{aligned}$$

for $\delta_b = v_b, h_b$. In our calculations, we have checked energy conservation for the method of moment code by using (85).

VI. NUMERICAL RESULTS AND DISCUSSIONS

In this section, we illustrate the numerical results of radar polarimetry of a layer of dielectric cylinders overlying a homogeneous half space using parameters of vegetation and soil [23-25]. The special case of statistical azimuthal symmetry will be examined. Thus for a function that depends on the orientation angles α and β , the averaging of the function $g(\alpha, \beta)$ is taken as follows

$$\langle g(\alpha, \beta) \rangle = \frac{1}{\cos\beta_1 - \cos\beta_2} \int_{\beta_1}^{\beta_2} d\beta \sin\beta \int_0^{2\pi} d\alpha g(\alpha, \beta) \tag{86}$$

The probability density function is uniform for solid angles with α between 0 and 2π , and β between β_1 and β_2 . The $\sin\beta$ factor in (86) accounts for the differential solid angle. The results of copolarized return, depolarized return, degree of polarization, and the phase differences [28] are illustrated for first order and second order solution. The first order solution consists of the sum of the first four terms in (16) (i.e., a, b, c, and d). The second order solution refers to the sum of all five terms in (16) (a, b, c, d, e). In all the figures we only show the results of MOM combined with the vector radiative transfer theory. The corresponding Mueller matrices are tabulated. Some of the Mueller matrices based on the infinite



cylinder approximation are also listed in the tables for comparison.

In Fig. 3, we plot the copolarized return, depolarized return, and degree of polarization for a medium of cylinders of length 15 cm and radius 2.5 cm at L band based on first order theory and MOM. The Mueller matrices of MOM, the infinite cylinder approach with scattered field and that with total field, are all listed in Table I for comparison. The absorption coefficients, scattering coefficients, and extinction coefficients for V and H polarizations are all listed so that the optical thicknesses can be calculated readily to see whether higher order scattering effects are important. We note from the tabulated Mueller matrices that there is some difference between the scattered field approximation and the total field approximation. However, there are large differences with the MOM results. This is because for this case, the radius of the cylinder is not small and significant errors are in the infinite cylinder approximation because the scattering-induced radiation from the ends of the cylinders are neglected. Also results based on the infinite cylinder approach do not obey reciprocity. That is, VH is not equal to HV . Some of the terms in the first order solution include scattering by the cylinder as well as reflection by the boundary. For example, the term that corresponds to first scattering by the cylinder and then reflection by the boundary makes use of the bistatic scattering amplitude of the cylinder which is not reciprocal in the infinite cylinder approximation. On the other hand, the MOM solution is reciprocal. The cylinders are uniformly oriented for β between 0° and 45° . As indicated in Fig. 3a, the HH return is larger than the VV return because of the randomness of orientation and the large radius of the cylinder. The results in Fig. 3 also indicate large variation of scattering with polarization.

(1) Infinite cylinder scattered field approximation

0.549E-02	0.188E-02	0.000	0.000
0.167E-02	0.593E-02	0.000	0.000
0.000	0.000	-0.481E-03	0.798E-03
0.000	0.000	-0.829E-03	0.354E-03

(2) Infinite Cylinder total field approximation

(The computed values of absorption and scattering rates based on infinite cylinder scattered field approximations are $\kappa_{av} = 0.138 \text{ m}^{-1}$, $\kappa_{ev} = 0.201 \text{ m}^{-1}$, $\kappa_{ah} = 0.0872 \text{ m}^{-1}$, $\kappa_{ah} = 0.0926 \text{ m}^{-1}$).

0.552E-02	0.189E-02	0.000	0.000
0.169E-02	0.604E-02	0.000	0.000
0.000	0.000	-0.575E-03	0.998E-03
0.000	0.000	-0.961E-03	0.227E-03

(3) Method of Moment solution

(The computed values of extinction rates are $\kappa_{ev} = 0.4037 \text{ m}^{-1}$, $\kappa_{eh} = 0.2324 \text{ m}^{-1}$).

0.882E-02	0.168E-02	0.000	0.000
0.168E-02	0.101E-01	0.000	0.000
0.000	0.000	-.277E-02	0.184E-02
0.000	0.000	-.184E-02	-.939E-03

(3) Method of Moment solution

(The computed values of extinction rates are $\kappa_{ev} = 0.4037 \text{ m}^{-1}$, $\kappa_{eh} = 0.2324 \text{ m}^{-1}$).

Table I. Mueller matrices of Fig. 3.

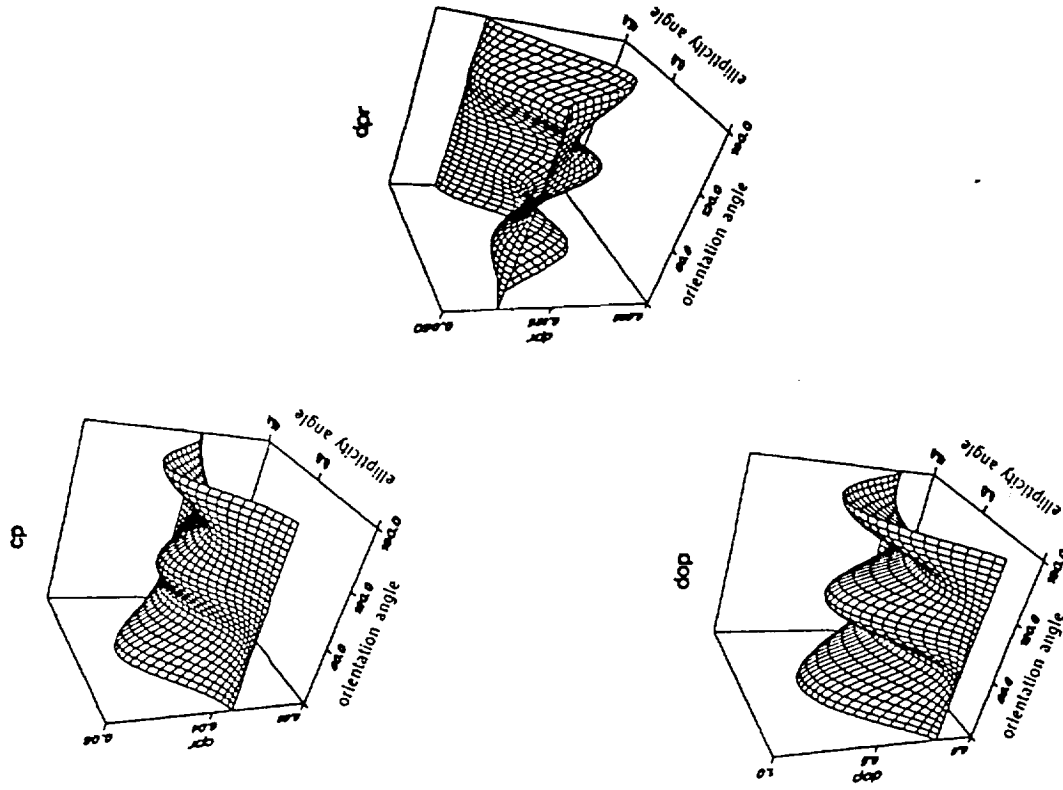


Figure 3. Polarimetric signatures based on first order theory and MOM code as a function of ellipticity angle ψ and orientation angle θ of a layer of dielectric cylinders with prescribed orientation distribution (a) copolarized return, (b) depolarized return, and (c) degree of polarization. The parameters are: frequency = 1.225 GHz, $\epsilon_s = (6.5 + i2)\epsilon_0$, $a = 2.5 \text{ cm}$, $L = 15 \text{ cm}$, fractional volume = 0.006, $d = 0.5 \text{ meters}$, $\epsilon_2 = (1.5 + i2)\epsilon_0$, and $\theta_0 = \theta_s = 60^\circ$. Orientation distribution is governed by $\beta_1 = 0^\circ$ and $\beta_2 = 45^\circ$. The values of the Mueller matrices based on MOM and infinite cylinder approximations are listed in Table I.

In Fig. 4, we show the case for cylinders with a smaller radius of $a = 1$ cm. The corresponding Mueller matrices for the three approaches are shown in Table II. Because of the smaller radius compared with wavelength, the results of the infinite cylinder approximation are in good agreement with MOM. The copolarized return indicate that VV is larger than HH for this case of slender cylinders. The copolarized return and the depolarized return also show that the variations of scattering with polarization are less rapid than that of Fig. 3.

In Figs. 5 and 6, we show respectively the results of first order theory and second order theory using the same parameters of Fig. 3 but with a larger layer thickness of $d = 2.5$ meters. The Mueller matrices are listed in Table III. The optical thicknesses are 1.01 and 0.58 respectively for vertical and horizontal polarizations. There is a significant amount of multiple scattering in this case as seen by the differences in results between the two figures. The Mueller matrices are listed in Table III. Inclusion of second order scattering significantly increases the contrast between the VV and HH return. It also significantly increases the depolarized return. The results also indicate that multiple scattering can be important at L band for some cases of medium parameters.

0.740E-02	0.126E-02	0.000	0.000
0.128E-02	0.411E-02	0.000	0.000
0.000	0.000	-0.181E-02	0.589E-03
0.000	0.000	-0.591E-03	-0.104E-02

(1) Infinite cylinder scattered field approximation

(The computed values of absorption and scattering rates based on infinite cylinder scattered field approximations are $\kappa_{av} = 0.245 \text{ m}^{-1}$, $\kappa_{sv} = 0.118 \text{ m}^{-1}$, $\kappa_{ah} = 0.0764 \text{ m}^{-1}$, $\kappa_{sh} = 0.0318 \text{ m}^{-1}$).

0.741E-02	0.128E-02	0.000	0.000
0.127E-02	0.411E-02	0.000	0.000
0.000	0.000	-0.183E-02	0.586E-03
0.000	0.000	-0.572E-03	-0.107E-02

(2) Infinite Cylinder total field approximation

0.703E-02	0.987E-03	0.000	0.000
0.987E-03	0.446E-02	0.000	0.000
0.000	0.000	-.204E-02	0.485E-03
0.000	0.000	-.485E-03	-.134E-02

(3) Method of Moments solution

(The computed values of extinction rates are $\kappa_{ev} = 0.2955 \text{ m}^{-1}$, $\kappa_{eh} = 0.0953 \text{ m}^{-1}$).

Table II. Mueller matrices of Fig. 4

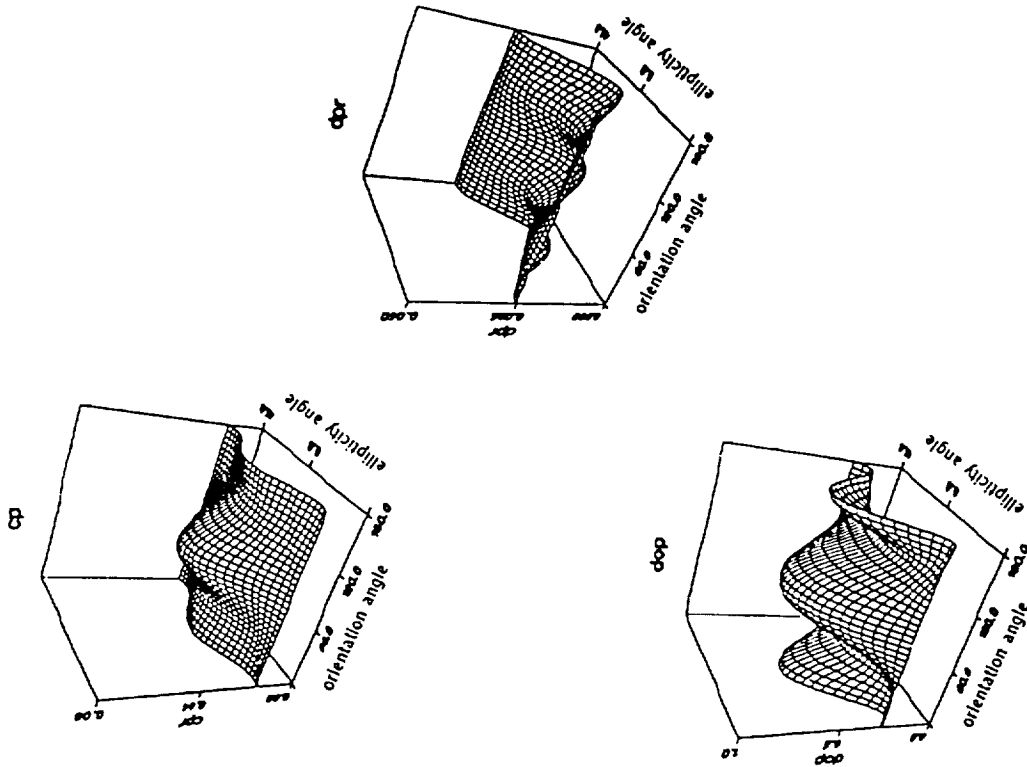


Figure 4. Polarimetric signatures based on first order theory and MOM code as a function of ellipticity angle χ and orientation angle ψ of a layer of dielectric cylinders with prescribed orientation distribution (a) copolarized return, (b) depolarized return, and (c) degree of polarization. The parameters are: frequency = 1.225 GHz, $\epsilon_s = (6.5 + i2)\epsilon_0$, $a = 1$ cm, $L = 15$ cm., fractional volume = 0.006, $d = 0.5$ meters, $\epsilon_2 = (15 + i2)\epsilon_0$, and $\theta_0 = \theta_s = 60^\circ$. Orientation distribution is governed by $\beta_1 = 0^\circ$ and $\beta_2 = 45^\circ$. The values of the Mueller matrices based on MOM and infinite cylinder approximations are listed in Table II.

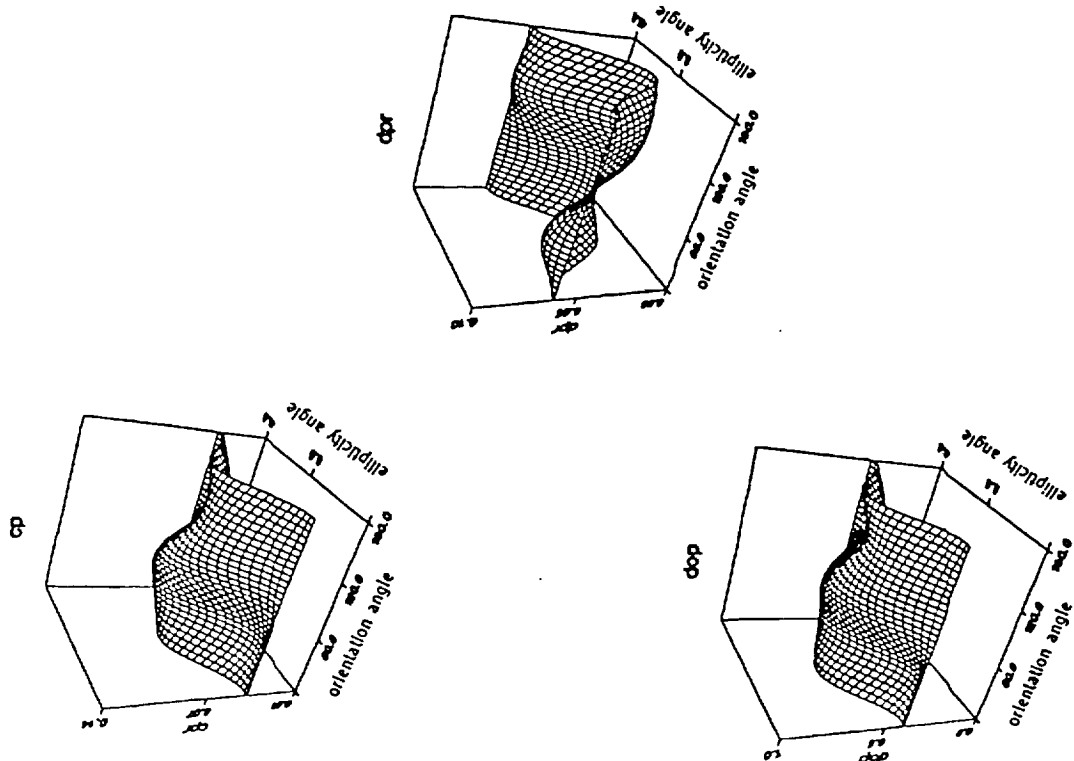


Figure 5. Polarimetric signatures based on first order theory and MOM code as a function of ellipticity angle χ and orientation angle ψ of a layer of dielectric cylinders with prescribed orientation distribution (a) copolarized return, (b) depolarized return, and (c) degree of polarization. The parameters are: frequency = 1.225 GHz, $\epsilon_g = (6.5 + i2)\epsilon_0$, $a = 2.5$ cm, $L = 15$ cm, fractional volume = 0.006, $d = 2.5$ meters, $\epsilon_2 = (15 + i2)\epsilon_0$, and $\theta_0 = \theta_g = 60^\circ$. Orientation distribution is governed by $\beta_1 = 0^\circ$ and $\beta_2 = 45^\circ$. The values of the Mueller matrices based on MOM are listed in Table III.

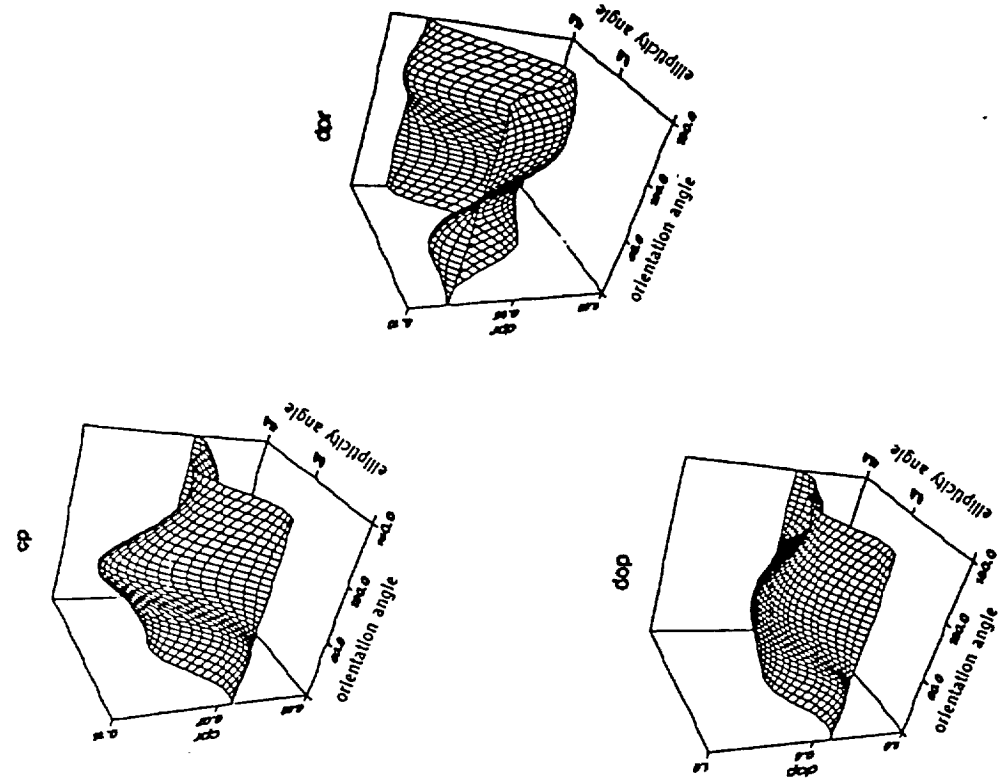


Figure 6. Polarimetric signatures based on second order theory and MOM code as a function of ellipticity angle χ and orientation angle ψ of a layer of dielectric cylinders with prescribed orientation distribution (a) copolarized return, (b) depolarized return, and (c) degree of polarization. The parameters are: frequency = 1.225 GHz, $\epsilon_g = (6.5 + i2)\epsilon_0$, $a = 2.5$ cm, $L = 15$ cm, fractional volume = 0.006, $d = 2.5$ meters, $\epsilon_2 = (15 + i2)\epsilon_0$, and $\theta_0 = \theta_g = 60^\circ$. Orientation distribution is governed by $\beta_1 = 0^\circ$ and $\beta_2 = 45^\circ$. The values of the Mueller matrices based on MOM are listed in Table III.

0.149E-01	0.263E-02	0.000	0.000
0.263E-02	0.122E-01	0.000	0.000
0.000	0.000	-.788E-02	0.537E-02
0.000	0.000	-.537E-02	-.335E-02
Mueller matrices of Fig. 5 (first order solution)			
0.219E-01	0.421E-02	0.000	0.000
0.422E-02	0.143E-01	0.000	0.000
0.000	0.000	-.101E-01	0.735E-02
0.000	0.000	-.737E-02	-.367E-02

Mueller matrix of Fig. 6 (second order solution)

Table III. (The computed values of extinction rates are $\kappa_{ev} = 0.4037 \text{ m}^{-1}$
 $\kappa_{eh} = 0.2324 \text{ m}^{-1}$).

In Figs. 7 and 8, the results at C band for the first order solution and second order solution are shown respectively. The Mueller matrices are listed in Table IV. The second order solution show a stronger contrast between VV and HH returns. It also shows larger depolarization return than the first order solution. There is strong depolarization even for linearly polarized waves. The results indicate that multiple scattering effects are generally important at C band.

0.296E-01	0.156E-02	0.000	0.000
0.156E-02	0.288E-01	0.000	0.000
0.000	0.000	-.166E-01	0.122E-01
0.000	0.000	-.122E-01	-.141E-01
Mueller matrices of Fig. 7 (first order solution)			
0.436E-01	0.316E-02	0.000	0.000
0.316E-02	0.327E-01	0.000	0.000
0.000	0.000	-.193E-01	0.164E-01
0.000	0.000	-.164E-01	-.146E-01

Mueller matrix of Fig. 8 (Second order solution)

Table IV. (The computed values of extinction rates are $\kappa_{ev} = 0.2353 \text{ m}^{-1}$
 $\kappa_{eh} = 0.1068 \text{ m}^{-1}$).

In Fig. 9, we plot the phase difference (i.e., phase at which the probability density function is maximum [28]) as a function of orientation with $\beta_1 = 0$ and β_2 varying between 0 degrees and 90 degrees using the parameters of C band of Figs. 7 and 8. The case of β_2 equal to zero corresponds to vertically aligned cylinders while β_2 equal to 90 degrees corresponds to completely random orientations. As can be seen from the figure, the case of a completely random orientation gives zero phase difference. We also note that the first order theory underestimates the phase difference. The phase difference is positive for cylinders while previous results indicate the phase difference is negative for oblate spheroids [11].

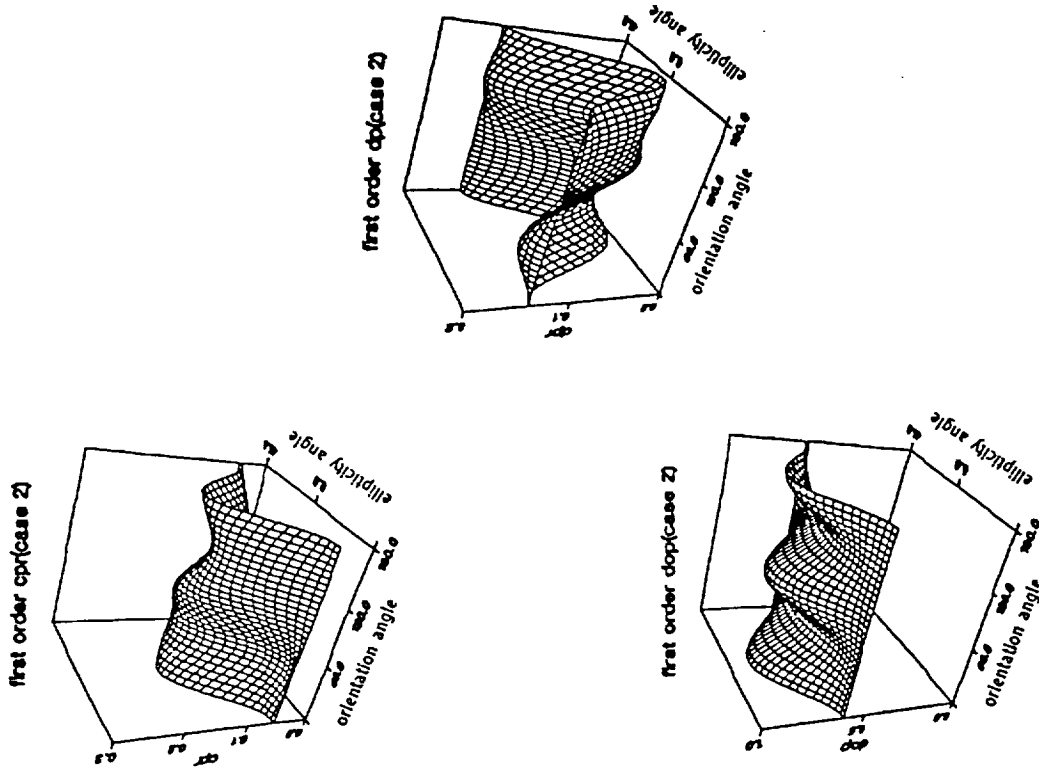


Figure 7. Polarimetric signatures based on first order theory and MOM code as a function of ellipticity angle χ and orientation angle ψ of a layer of dielectric cylinders with prescribed orientation distribution (a) copolarized return, (b) depolarized return, and (c) degree of polarization. The parameters are: frequency = 5.64 GHz, $\epsilon_s = (3 + i0.06)\epsilon_0$, $a = 0.35 \text{ cm}$, $L = 5 \text{ cm}$, fractional volume = 0.006, $d = 2.5 \text{ meters}$, $\epsilon_2 = (4 + i)\epsilon_0$, and $\theta_0 = \theta_s = 60^\circ$. Orientation distribution is governed by $\beta_1 = 0^\circ$ and $\beta_2 = 45^\circ$. The values of the Mueller matrices based on MOM are listed in Table IV.



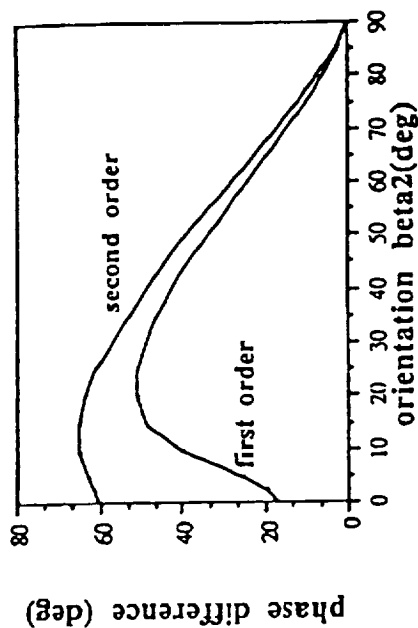


Figure 9. Phase differences (9) based on first order theory and second order theory are compared as a function of orientation distribution. Orientation distribution is governed by $\beta_1 = 0^\circ$ and β_2 varying between 0 degrees and 90 degrees. Phase matrices and extinction matrices are based on MOM code. The parameters are: frequency = 5.64 GHz, $\epsilon_s = (3 + i0.06)\epsilon_0$, $a = 0.35$ cm, $L = 5$ cm, fractional volume=0.006, $d = 2.5$ meters, $\epsilon_2 = (4 + i)\epsilon_0$, $\theta_0 = \theta_s = 60^\circ$.

In Fig. 10 we make a comparison of total surface fields for $m = 0$ harmonic, computed based on infinite cylinder approximation (IC) and MOM solution using the parameters of the dielectric cylinder of Fig. 3. The incident wave is of unit amplitude in a direction perpendicular to the axis of the cylinder with polarization parallel to the axis of the cylinder. Equivalent electric surface currents ηJ_t and equivalent magnetic surface current M_ϕ are shown. The t coordinate and the t direction is as indicated in the figure. As shown in Fig. 10, the infinite cylinder approximation has a magnitude of equivalent surface currents uniform along the length of the cylinder while the MOM solution has currents tapering off towards the two endfaces.

In Table V, we compare the CPU time of the various methods that are used in computing the results of Fig. 3. We note that the CPU required for MOM for one cylinder far exceeds that of infinite cylinder approximation. In vector radiative transfer first and second order solutions, however, most of the CPU goes to the computation of averaging over orientations and summing over scattered directions from one cylinder to another. Thus the CPU of MOM becomes a small fraction of the total CPU. As indicated in the table, the total required CPU for the first order solution differs only by a factor of 4 between that of MOM and infinite cylinder approximation.

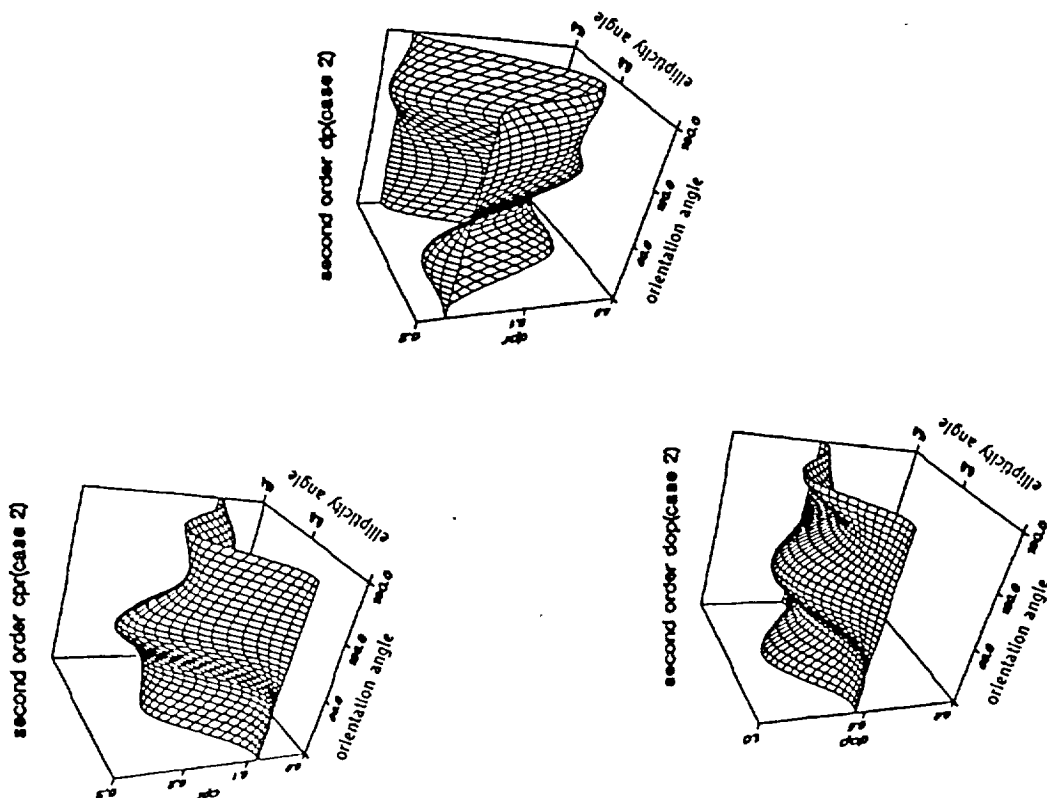


Figure 8. Polarimetric signatures based on second order theory and MOM code as a function of ellipticity angle χ and orientation angle ψ of a layer of dielectric cylinders with prescribed orientation distribution (a) copolarized return, (b) depolarized return, and (c) degree of polarization. The parameters are: frequency = 5.64 GHz, $\epsilon_s = (3 + i0.06)\epsilon_0$, $a = 0.35$ cm, $L = 5$ cm, fractional volume=0.006, $d = 2.5$ meters, $\epsilon_2 = (4 + i)\epsilon_0$, $\theta_0 = \theta_s = 60^\circ$. Orientation distribution is governed by $\beta_1 = 0^\circ$ and $\beta_2 = 45^\circ$. The values of the Mueller matrices based on MOM are listed in Table IV.

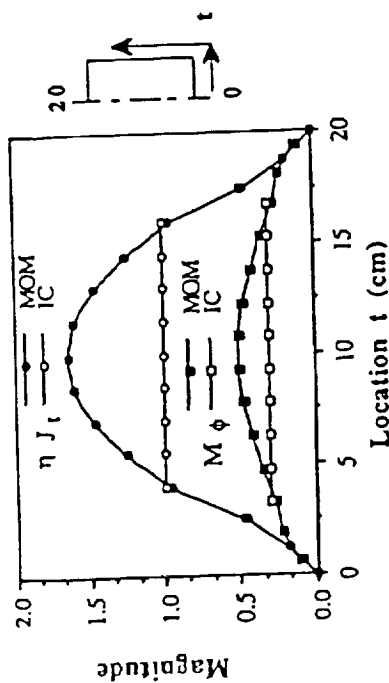


Figure 10. Comparison of total surface fields for $m = 0$ harmonic computed based on infinite cylinder approximation (IC) and MOM solution using parameters of dielectric cylinder of Fig. 3 with frequency = 1.225 GHz, $\epsilon_s = (6.5 + i2)\epsilon_0$, $a = 2.5$ cm, $L = 15$ cm. The incident wave is of unit amplitude in a direction perpendicular to the axis of the cylinder with polarization parallel to the axis of the cylinder. Equivalent electric surface currents ηJ_t and equivalent magnetic surface current M_ϕ are shown. The t coordinate and the ϕ direction is as indicated in the figure. The t coordinate starts from center of bottom face, radially outward to the edge, along the curved side and then ends at the center of the top face with range 2.5 cm + 15 cm + 2.5 cm = 20 cm.

Method	Single Particle Scattering	Vector Radiative Transfer Solution	Total CPU Required
first order vector radiative transfer and MOM	89 sec	391 sec	480 sec
second order vector radiative transfer and MOM	89 sec	5932 sec	6021 sec
first order vector radiative transfer and infinite cylinder approximation			122 sec

Table V. Comparison of CPU of various methods on DEC Station 3100 for computer results of Fig. 3.

ACKNOWLEDGMENTS

The research in this paper was supported by the Army Research Office, NASA, and the National Science Foundation.

The Editor thanks S. S. Seker and two anonymous Reviewers for reviewing the paper.

REFERENCES

- Huynen, J. R., "Phenomenological theory of radar targets" *Electromagnetic Scattering*, ed. by P. L. E. Ustenghi, 653-712, Academic Press, New York, 1978.
- Tsang, L., J. A. Kong, and R. T. Shin, *Theory of Microwave Remote Sensing*, Wiley Interscience, New York, 1985.
- Giuli, D., "Polarization diversity in radars." *Proc. IEEE*, Vol. 74, 245-269, 1986.
- Ulaby, F. T., and C. Elachi (eds.), *Radar Polarimetry for Geoscience Applications*, Artech House, Norwood, MA, 1990.
- Kong, J. A., (ed.), "Polarimetric remote sensing," *Progress in Electromagnetic Research*, Vol. 3, Elsevier, New York, 1990.
- van Zyl, J. J., H. A. Zebker, and C. Elachi, "Imaging radar polarization signatures: theory and observation," *Radio Science*, Vol. 22, 529-543, 1987.
- Ulaby, F. T., D. N. Held, M. C. Dobson, K. C. McDonald, and T. B. A. Senior, "Relating polarization difference of SAR signals to scene properties," *IEEE Trans. Geoscience and Remote Sensing*, GE-25, 83-92, 1987.
- Evans, D. L., T. G. Farr, J. J. van Zyl, and H. A. Zebker, "Radar polarimetry: analysis tools and applications," *IEEE Trans. Geoscience and Remote Sensing*, GE-26, 774-789, 1988.
- Borgeaud, M., R. T. Shin, and J. A. Kong, "Theoretical models for polarimetric radar clutter," *J. Electromagnetic Waves and Applications*, Vol. 1, 73-89, 1987.
- Boerner, W. M., B. Y. Foo, and H. J. Eom, "Interpretation of polarimetric copolarization phase term in radar images obtained with the JPL airborne L-band SAR system," *IEEE Trans. Geoscience and Remote Sensing*, GE-25, 77-82, 1987.
- Tsang, L., K. H. Ding, and B. Wen, "Polarimetric signatures of random discrete scatterers based on vector radiative transfer theory, Part I: Nonspherical particles, and Part II: Dense Media," Chapter 2 of *Polarimetric Remote Sensing*, 75-142, Vol. 3 of *Progress in Electromagnetic Research*, ed. by J. Kong, Elsevier, New York, 1990.
- Wen, B., L. Tsang, D. P. Winebrenner, and A. Ishimaru, "Dense medium radiative transfer theory: comparison with experiment and application to microwave remote sensing and polarimetry," *IEEE Trans. Geosci. Remote Sensing*, GE-28, 46-59, 1990.
- Ulaby, F. T., K. Sarabandi, K. McDonald, M. Whitt, and M. C. Dobson, "Michigan microwave canopy scattering model (MIMICS)," *Radiation Laboratory Report 022486-T-1*, Department of Electrical Engineering and Computer Science, The University of Michigan, Ann Arbor, Michigan, July 1988.
- Chen, Z., M.Sc. Thesis, Department of Electrical Engineering, University of Washington, Seattle, WA 981995, Nov. 1990.
- Tsang, L., and K. H. Ding, "Polarimetric signatures of a layer of random nonspherical discrete scatterers overlying a homogeneous half space based on first and second order vector radiative transfer theory," *IEEE Trans. on Geoscience and Remote Sensing*, Vol. 29, No. 2, 242-252, March 1991.
- Chauhan, N. S., and R. H. Lang, "Microwave modelling of orchard canopy," *Proceedings of IGARSS'88*, 1757, Edinburgh, Scotland, 1988.
- Seker, S. S., and A. Schneider, "Electromagnetic scattering from a dielectric cylinder of finite length," *IEEE Trans. on Antennas and Propagation*, AP-36, 303-307, 1988.
- Karam, M., and A. K. Fung, "Electromagnetic scattering from a layer of finite length, randomly oriented dielectric circular cylinders over a rough interface with application to vegetation," *Int. J. Remote Sensing*, Vol. 9, 1109-1134, 1988.
- Iorn, M., and E. Wolf, *Principles of Optics*, Fifth Edition, Pergamon Press, New York.

20. Karam, M. A., and A. K. Fung, "Vector forward scattering theorem," *Radio Science*, Vol. 17, 752-756, 1982.
21. Glisson, A. W., and D. R. Wilton, "Simple and efficient numerical techniques for treating bodies of revolution," *Technical Report 105*, Engineering Experiment Station, The University of Mississippi, University, Mississippi, March 1979.
22. Joseph, J., "Application of integral equation and finite difference method to electromagnetic scattering by two dimensional and body of revolution geometries," Ph.D. thesis, Department of Electrical and Computer Engineering, University of Illinois at Urbana-Champaign, Urbana, Illinois, May 1990.
23. EL-Rayes, M. A., and F. T. Ulaby, "Microwave dielectric spectrum of vegetation, Part I: Experimental observations," *IEEE Trans. Geoscience and Remote Sensing*, GE-25, 541-549, 1987.
24. Ulaby, F. T., and M. A. EL-Rayes, "Microwave dielectric spectrum of vegetation, Part II: Dual dispersion model," *IEEE Trans. Geoscience and Remote Sensing*, GE-25, 550-57, 1987.
25. Newton, R. W., and J. W. Rouse, Jr., "Microwave radiometer measurements of soil moisture content," *IEEE Trans. Antennas and Propagation*, AP-28, 680-686, 1980.
26. Tsang, L., Z. Chen, S. Oh, R. Marks II, and A. Chang, "Inversion of snow parameters from passive microwave remote sensing measurements by a neural network trained with a multiple scattering model," *Proceedings of IGARSS'91*, 1965-1968, Espoo, Finland, 1991.
27. Tsang, L., "Polarimetric passive remote sensing of rough surfaces and discrete scatterers," *J. of Electromagnetic Waves and Applications*, Vol. 5, No. 1, 41-57, 1991.
28. Sarabandi, K., "Derivation of phase statistics of distributed targets from the averaged Mueller matrix," *Technical Report 026511-I-T*, Radiation Laboratory, Department of Electrical Engineering and Computer Science, University of Michigan, Ann Arbor, April 1991.

Leung Tsang received the SB (1971), SM, EE (1973), and Ph.D. (1976) from the Massachusetts Institute of Technology. He is presently a Professor of Electrical Engineering at the University of Washington. He is co-author of the book *Theory of Microwave Remote Sensing* Wiley-Interscience, 1985). He is on the editorial board of the *Journal of Electromagnetic Waves and Applications* (1987-1990), the *Journal of Waves in Random Media* (1990-present), an Associate Editor of *Radio Science* (1988-present) and an Associate Editor of the *IEEE Trans. on Geoscience and Remote Sensing* (1987-present). He is a Fellow of the IEEE and a member of the Electromagnetics Academy. His current research interests are in microwave remote sensing, waves in random media, and solid state theory of optoelectronics.

Chi Hou Chan attended Hong Kong Polytechnic and the City College of New York. He received the B.S. and M.S. degrees in electrical engineering from Ohio State University, Columbus, in 1981 and 1982, respectively, and the Ph.D. degree in electrical engineering from the University of Illinois at Urbana-Champaign, in 1987. He was a Visiting Assistant Professor associated with the Electromagnetic Communication Laboratory in the Department of Electrical and Computer Engineering at UIUC. Since September 1989, he has been an Assistant Professor of Electrical Engineering at the University of Washington, Seattle. He is a recipient of the Presidential Young Investigator award in 1991.

Jin Au Kong is Professor of Electrical Engineering and Chairman of Area IV on Energy and Electromagnetic Systems in the Department of Electrical Engineering and Computer Science at the Massachusetts Institute of Technology in Cambridge, Massachusetts. His research interest is in the field of electromagnetic wave theory and applications. He has published 7 books and over 300 refereed journal and conference papers, is the Editor of the Wiley Series in Remote Sensing, and is Chief Editor of the Elsevier book series

Progress In Electromagnetics Research (PIER).

James Joseph received his B.S. from the University of Kerala, M.S. from the University of Mississippi, and Ph.D. from the University of Illinois at Urbana-Champaign, all in Electrical Engineering. Since July 1990, he has been with the General Electric Corporate Research and Development Laboratory in Schenectady, New York. His current research interests include non-destructive testing of composite materials, electromagnetic and acoustic-scattering and radiation, and numerical methods.

